NANOTECHNOLOGY APPLICATIONS FOR BIOMASS PRETREATMENT, FUNCTIONAL MATERIAL FABRICATION AND SURFACE MODIFICATION

By

Wei Wang

A DISSERTATION

Submitted to
Michigan State University
in partial fulfillment of the requirements
for the degree of

DOCTOR OF PHILOSOPHY

Chemical Engineering

2012

ABSTRACT

NANOTECHNOLOGY APPLICATIONS FOR BIOMASS PRETREATMENT, FUNCTIONAL MATERIAL FABRICATION AND SURFACE MODIFICATION

By

Wei Wang

Nanotechnology has gained its prosperity in the past two decades because of extensive contributions from interdisciplinary collaboration and a favorable interaction with practical applications. It covers a huge spectrum of applications. The dissertation hereby, in conjunction with the three research projects conducted by the author, will make contributions to nanotechnology applications in the following three topics: biomass pretreatment in biofuel production, functional material fabrication and surface modification.

First, a fast and efficient nano-scale shear hybrid alkaline (NSHA) pretreatment method of lignocellulosic biomass was introduced. In this work, corn stover was pretreated in a modified Taylor-Couette reactor with sodium hydroxide at room temperature, with a two-minute retention time and a 12500 s^{-1} shear rate. Synergistic effects induced by the NSHA pretreatment disrupted the naturally-formed recalcitrance of biomass and generated nano-scale polysaccharide aggregates that are ready to be digested. After the pretreatment, results revealed major removals of hemicellulose and lignin, leaving an up to 82 % of cellulose content in the remaining solid. Compared with untreated corn stover, an approximately 4-fold increase in enzymatic cellulose conversion and a 5-fold increase in hemicellulose conversion were achieved.

Second, a nano-deposition strategy was developed to enhance the energy absorption capacity of aluminum (Al) open-cell foams. The energy absorption capacity of open cell foams can be enhanced by a homogeneous thickening of the foam struts. However, the enhancement is compromised since an increase in the plateau stress without a reduction in densification strain

cannot be achieved. To overcome that problem, a featured non-cyanide nano-crystalline copper electro-deposition system was setup for the coating of open-cell Al foam, and, the energy absorption capacity as a function of foam pore size and Cu coating thickness was investigated. An up to 3-time enhancement was achieved with a 60 μm Cu coating on Al foams with an average strut thickness of 192 μm. The compressive stress-strain response of the composite samples showed no significant reduction of the densification strain compared to the uncoated foams. With the same overall strut thickness, nano-reinforced foams had superior energy absorption capacity over plain foams, with almost a 2-time enhancement.

Finally, a facile "dip & rinse" method for nickel (Ni) electroless deposition on hydrophobic polymer surfaces was developed. The electroless deposition (metallization) usually incorporates a harsh and/or toxic surface conditioning to activate the substrate. To eliminate the need for that step, a facile method of electroless Ni deposition on various hydrophobic polymer substrates was demonstrated, by making use of the hydrophobic interactions between Poly(allylamine hydrochloride) (PAH) and polymer substrates for catalyst adsorption/immobilization. Various hydrophobic polymer surfaces with different geometries and dimensions, including low density polyethylene (LDPE), high density polyethylene (HDPE), polypropylene (PP) and polystyrene (PS) thin sheets, and PE pellets were tested and Ni was successfully deposited onto all these surfaces. A kinetic study on polymer thin sheets examples showed that with 2 hours of deposition, an approximately 2 μm thickness was achieved. A prove-of-concept study showed that Ni coated polymer thin sheets can be further electrodeposited with heterogeneous metal (Cu), hence enabling a faster thickness growth over time.

DEDICATION

This dissertation is dedicated to my family, especially my beloved wife, Kaiyao Ni, my parents, Jianying Jin and Fengqiang Wang, my parents in law, Shaozhen Lu and Zhi'an Ni, and all other members.

ACKNOWLEDGEMENTS

It has been a great privilege to spend several years in the Department of Chemical Engineering and Materials Science at Michigan State University for my PhD study and completion of the dissertation. The Spartan spirit, which I will carry on with wherever I go, has been inspirational to me and made me who I become today.

This dissertation would not have been accomplished without help from many people in many ways. I would like to acknowledge all of them from the bottom of my heart.

First and foremost, with immense gratitude I would like to acknowledge my PhD advisor and mentor, Professor Ilsoon Lee for his continuous guidance and support throughout the production of this research and dissertation. He has been patiently providing unique insights and encouragement for me to proceed through the PhD program. His mentorship in various ways is a precious treasure to me.

I am also grateful to my dissertation committee members, Professor K. Jayaraman, Professor David Hodge and Professor Jung-Wuk Hong for the invaluable discussions and help to my research work. Their lectures on different topics helped me improve my knowledge in the related areas. Also, their constructive suggestions and inputs make this dissertation better.

Special thanks go to Professor Rigoberto Burgueño for his support and all the helpful discussions, comments and contributions to the Chapter 3 in this dissertation.

I am also thankful to Dr. Jue Lu at Metna Corporation. She has been incredibly helpful in providing me with the samples, useful information and feedbacks.

I would like to thank my colleagues and office mates at EB 2522, Shaowen Ji, Ankush Gokhale, Oishi Sanyal, Tongjun Liu, Xianfeng Ma, Rui Lin, Yangmu Liu, Bhushan Awate, Ying

Liu, Lee Alexander, Yi Sun, Jing Yu and Anna Song for their friendship and help all over the years. It is a great pleasure working with these brilliant people. Their company made my time in the lab enjoyable.

I am indebted to my family for their unconditional love and support. Being away from my parents for so many years helped me better realize how important the family means to me. My beloved wife, Kaiyao Ni made me the luckiest man on earth to have her with me for a lifetime. I appreciate the love, care and everything she did for me. My parents, Jianying Jin and Fengqiang Wang have had their love and support for me since the day I was born. Their trust in me and good examples by themselves gave me strength to overcome the challenges and difficulties throughout my PhD program. My parents in law, Shaozhen Lu and Zhi'an Ni, who treat me like their own son, are unconditionally supportive and caring all over the years. I am also thankful to all my other family members for their love and support.

Last but not least, I want to acknowledge the National Science Foundation, Michigan's University Research Corridor and Michigan Initiative for Innovation & Entrepreneurship for the financial support on my research.

TABLE OF CONTENTS

LIST OF TABLES ix

LIST OF FIGURES x

Chapter 1 Introduction 1
- **1.1 Overview of the nanotechnology** 1
- **1.2 Nanotechnology for biofuel production** 5
- **1.3 Nanotechnology for functional material fabrication** 8
- **1.4 Nanotechnology for surface modification** 11
- **1.5 Scope of the dissertation** 14
- **REFERENCES** 19

Chapter 2 Fast and efficient nanoshear hybrid alkaline pretreatment of corn stover for biofuel and materials production 27
- **2.0 Abstract** 27
- **2.1 Introduction** 28
- **2.2 Experimental Sections** 29
  - 2.2.1 Materials 29
  - 2.2.2 Modified Taylor-Couette reactor (nanomixer) 30
  - 2.2.3 Nanoshear hybrid alkaline pretreatment 32
  - 2.2.4 Washing 32
  - 2.2.5 Drying 33
  - 2.2.6 Compositional analysis 33
  - 2.2.7 Enzymatic hydrolysis 33
  - 2.2.8 Scanning electron microscope (SEM) imaging 34
- **2.3 Results and discussions** 34
  - 2.3.1 Compositional analysis 34
  - 2.3.2 Chemical and energy recovery 37
  - 2.3.3 Enzymatic hydrolysis 38
  - 2.3.4 Scanning electron microscope (SEM) imaging 44
- **2.4 Conclusions** 48
- **REFERENCES** 51

Chapter 3 Nano-deposition on 3-D open-cell aluminum foam materials for improved energy absorption capacity 55
- **3.0 Abstract** 55
- **3.1 Introduction** 56
- **3.2 Experimental Methods** 58
  - 3.2.1 Materials and equipment 58
  - 3.2.2 Sample pretreatment 59
  - 3.2.3 Electro-deposition 60
  - 3.2.4 Scanning electron microscope (SEM) imaging 62

3.2.5 Crystallite size determination using X-ray diffraction (XRD) 62
3.2.6 Quasi-static compression test 63
3.3 Results and discussions 63
3.3.1 3-D deposition visualization and uniformity 64
3.3.2 Quasi-static compression test and energy absorption calculation 73
3.3.3 Comparison between coated and uncoated foam samples with same strut thickness 80
3.4 Conclusions 83
REFERENCES 85

Chapter 4 A facile method of nickel electroless deposition on various neutral hydrophobic polymer surfaces 89
4.0 Abstract 89
4.1 Introduction 90
4.2 Experimental sections 92
4.2.1 Materials and equipment 92
4.2.2 Ni electroless deposition 93
4.2.3 Copper (Cu) electro-deposition 94
4.2.4 Scanning electron microscopy (SEM) imaging 95
4.2.5 Kinetic study of Ni deposition on polymers 95
4.2.6 Optical microscopy imaging 96
4.3 Results and discussions 96
4.3.1 Visualization and microscopic analysis of polymer thin sheets 96
4.3.2 Visualization and microscopic analysis of polymer pellets and spheres 107
4.3.2.1 Ni deposition on PE pellets 110
4.3.2.2 Ni deposition on PS microspheres 111
4.3.3 Kinetic study of Ni deposition 114
4.3.3 Cu electro-deposition on Ni coated polymer 116
4.4 Conclusions 119
REFERENCES 122

Chapter 5 Conclusions and future work 127
5.1 Conclusions 127
5.2 Outlook & future work 129

LIST OF TABLES

Table 2.1 Major fractions[a] of the pretreated corn stover after pretreatment methods [8, 39]. 36

Table 3.1 Specimen name designations and coating information..... 72

Table 3.2 Important parameters and calculations for 40 PPI uncoated and copper coated samples 75

Table 3.3 Important parameters and calculations for 20 PPI uncoated and copper coated samples 76

Table 3.4 Important parameters and calculations for 10 PPI uncoated and copper coated samples 77

Table 3.5 Energy absorption calculations and comparison based on Figure 3.15 81

LIST OF FIGURES

Figure 1.1 Diverse applications of nanotechnology. (For interpretation of the references to color in this and all other figures, the reader is referred to the electronic version of this dissertation.) .. 3

Figure 1.2 The Bottom-up (a) and Top-down (b) approaches in nanotechnology application. Reproduced with permission from Ref [17]. 4

Figure 2.1 Schematic illustration of the modified Taylor-Couette reactor (nanomixer). 31

Figure 2.2 Major fractions of the remaining solid of CS before and after pretreatment at different conditions. 35

Figure 2.3 Cellulose and hemicellulose conversion profile of the NSHA pretreated CS with 4 g L^{-1} and 40 g L^{-1} NaOH, with a 5 FPU (g cellulose)$^{-1}$ enzyme loading, and a 50 °C incubation temperature..... 39

Figure 2.4 Cellulose and hemicellulose conversion profile of the NSHA pretreated CS with 4 g L^{-1} and 40 g L^{-1} NaOH, with a 20 FPU (g cellulose)$^{-1}$ enzyme loading, and a 50 °C incubation temperature..... 40

Figure 2.5 Cellulose and hemicellulose conversion profile of the NSHA pretreated CS, with a 60 FPU (g cellulose)$^{-1}$ enzyme loading, and a 50 °C incubation temperature..... 41

Figure 2.6 From crystalline to disrupted structure – before and after pretreatment at different conditions. a) Untreated corn stover, area pointed by the arrow is an intact cell wall; b) nanoshear hybrid water pretreated CS; c) 4 g L^{-1} NaOH NSHA pretreated CS, area pointed by the arrow is a discontinued structure with a reduced fiber length (fibrillation); d) 20 g L^{-1} NaOH NSHA pretreated CS, area indicated by the circle is where cellulose crystalline structure breaks apart (another form of fibrillation); e) 40 g L^{-1} NaOH NSHA pretreated CS, minipores and more disrupted fibers..... 45

Figure 2.7 Fibril aggregates on the surface of the cellulose crystalline structure. a) 40 g L^{-1} NaOH NSHA pretreated CS, nano-fibril aggregates retained on the surface of a single cellulose fiber, diameters are around 300-500 nanometers; b) 40 g L^{-1} NaOH NSHA pretreated CS, more fibril aggregates with thinner diameters..... 47

Figure 3.1 The electro-deposition system applied in this study. A rare metal rectangular bar mesh attached with copper sheets was used as the anode in the system. The aluminum foam was connected to the cathode and centered in the mesh to enable the uniform transfer of electrons and copper cations. 61

Figure 3.2 Electro-deposition kinetic studies on open-cell Al foams. Straight lines are theoretical values based on Faraday's law of electrolysis. Dots in different shapes are experimental data. .. 62

Figure 3.3 SEM (a) and EDX elmental mapping (b) on a Cu coated Al foam. The distribution of each element is: 97.6 wt % (or 91.8 at %) of Cu, 0.4 wt % (or 0.9 at %) of Al and 2.0 wt % (or 7.3 at %) of O. 65

Figure 3.4 Uncoated Al foams (a) and Cu coated Al foams (b). Left: 10 PPI; middle: 20 PPI; right: 40 PPI 66

Figure 3.5 Top view digital image of Cu coated Al foams at cut area 66

Figure 3.6 Middle section of a copper electrodeposited Al foam. a) and b) SEM images of selected areas..... 67

Figure 3.7 SEM (a) and EDX elemental mapping (b) at sample cut area, where Al and Cu can be seen at the same time. The distribution of each element is: 72.0 wt % (or 50.0 at %) of Cu, 24.3 wt % (or 39.7 at %) of Al and 3.7 wt % (or 10.3 at %) of O. 68

Figure 3.8 SEM images of Cu coated Al foams at different scales 69

Figure 3.9 XRD pattern of a Cu coated Al foam. Crystallite size was calculated using the Cu peak at 43.3° in this curve. Using the Scherrer formula the crystalline size of deposited Cu was 38 nm. 71

Figure 3.10 Cu coated Al foams before (a) and after (b) quasi-static compression tests 74

Figure 3.11 Compressive stress-strain response of 10 PPI open-cell Al foams with different relative densities (i.e., different strut thicknesses). 74

Figure 3.12 Compressive stress-strain responses of 40 PPI uncoated and coated foam samples. The samples were compressed at 0.1 in/min, until 80 % strain was achieved. The embedded figure represents the enlarged elastic region. Linear trend lines were used to fit the curve of the elastic region of each sample. 75

Figure 3.13 Compressive stress-strain responses of 20 PPI uncoated and coated foam samples. The embedded figure represents the enlarged elastic region. Linear trend lines were used to fit the curve of the elastic region of each sample. 76

Figure 3.14 Compressive stress-strain responses of 10 PPI uncoated and coated foam samples. The samples were compressed at 0.1 in/min, until 80 % strain was achieved. The embedded figure represents the enlarged elastic region. Linear trend lines were used to fit the curve of the elastic region of each sample. 77

Figure 3.15 Compressive stress-strain responses of 10 PPI samples. "US10-HD" denotes an uncoated 10 PPI sample, with high density (12 (±1) % relative density), and a strut thickness

around 580 μm; “CS10-95” represents a coated 10 PPI sample, starting from a 6 (±1) % relative density, with an approximately 95 μm coating thickness. Al foams with 6 (±1) % relative density were Cu coated until their strut thickness was equivalent to Al foams with 12 (±1) % relative density. All samples were tested under quasi-static compression at 0.1 in/min. The embedded figure represents the enlarged elastic region. Linear trend lines were used to fit the curve of the elastic region of each sample. 81

Figure 4.1 Overall scheme of Ni electroless deposition on a hydrophobic polymer thin sheet.... 97

Figure 4.2 Visualization and comparison of Ni coating on various hydrophobic polymer thin sheets (LDPE, HDPE, PP, PS). Non-PAH modified polymer sheets were not able to form Ni coating. 100

Figure 4.3 Visualization of Ni coating on a PP polymer thin sheet. Upper left is a SEM image at the edge of Ni coating; upper right is the corresponding EDX elemental mapping (60 wt % of C, 11 wt % of Au, 29 wt % of Ni); lower left is a SEM image at the main coating body; lower right is the corresponding EDX elemental mapping (6 wt % of C, 5 wt % of O, 18 wt % of Au, 71 wt % of Ni)..... 101

Figure 4.4 Visualization of Ni coating on a PS polymer thin sheet. Upper left is a SEM image at the edge of Ni coating; upper right is the corresponding EDX elemental mapping (44 wt % of C, 3 wt % of O, 8 wt % of Au, 45 wt % of Ni); lower left is a SEM image at the main coating body; lower right is the corresponding EDX elemental mapping (4 wt % of O, 12 wt % of Au, 84 wt % of Ni). 102

Figure 4.5 Visualization of Ni coating on a HDPE polymer thin sheet. Upper left is a SEM image at the edge of Ni coating; upper right is the corresponding EDX elemental mapping (37 wt % of C, 6 wt % of O, 9 wt % of Au, 48 wt % of Ni); lower left is a SEM image at the main coating body; lower right is the corresponding EDX elemental mapping (3 wt % of C, 4 wt % of O, 9 wt % of Au, 84 wt % of Ni). 103

Figure 4.6 Visualization of Ni coating on a LDPE polymer thin sheet. Upper left is a SEM image at the edge of Ni coating; upper right is the corresponding EDX elemental mapping (51 wt % of C, 7 wt % of Au, 42 wt % of Ni); lower left is a SEM image at the main coating body; lower right is the corresponding EDX elemental mapping (28 wt % of C, 3 wt % of O, 8 wt % of Au, 61 wt % of Ni)..... 104

Figure 4.7 The evolution of Ni coating morphologies on the LDPE surfaces. 105

Figure 4.8 Overall scheme of the Ni electroless deposition on the hydrophobic polymer pellet/sphere. 108

Figure 4.9 Visualization of Ni deposition on PE pellets. Non-PAH modified PE pellets were not able to form Ni coating. 109

Figure 4.10 SEM images of a) uncoated PE pellets; b) a coated PE pellet. The corresponded diagram next to each image shows the element signal of a selected area designated in the SEM image. 110

Figure 4.11 SEM images of a) PS microspheres before coating; b) non-PAH modified PS microspheres after Ni deposition; c) and d) PAH modified PS microspheres after Ni deposition. 112

Figure 4.12 A morphological change of HDPE thin sheet, during Ni electroless deposition. ... 113

Figure 4.13 A morphological change of PS thin sheet, during the Ni electroless deposition. 114

Figure 4.14 Kinetic studies and comparison of Ni electroless deposition on HDPE and PS, respectively. A nominal thickness gain over coating time was plotted. 115

Figure 4.15 Visualization of Cu deposition on Ni coated PS thin sheets, after Cu electro-deposition. Uncoated PS sheets were not able to form Cu coating. 117

Figure 4.16 Visualization of Cu coating on a Ni coated PS thin sheet, after Cu electro-deposition. Upper left is a SEM image at the edge of Cu coating; upper right is the corresponding EDX elemental mapping (36 wt % of C, 3 wt % of O, 21 wt % of Au, 39 wt % of Ni); lower left is a SEM image at the main coating body; lower right is the corresponding EDX elemental mapping (3 wt % of O, 14 wt % of Au, 82 wt % of Ni). 118

Chapter 1 Introduction

1.1 Overview of the nanotechnology

The word "nano" is derived from a Greek word for dwarf. It represents one billionth. "Nanotechnology" represents a characterization, operation or controlling of matters on the nano-scale, for unique or improved properties, products and devices [1]. The concept of nanotechnology originates from a lecture "There is Plenty of Room at the Bottom", given by the Nobel laureate Richard Feynman in 1959 [1, 2]. In his lecture, he was challenging the scientific community, imagining the entire Encyclopedia Britannica to be written on the head of a pin [2].

Since then, without a significant advance in instrumentation, the nanotechnology did not receive broad attention until the early 1980s, when the scanning tunneling microscope (STM) [3, 4] and atomic force microscope (AFM) [5, 6] were introduced. At the time they were invented, the STM had a spatial resolution of 0.1 nanometer (nm), whereas the AFM had a spatial resolution of 0.05 nm. With the development of these techniques and sophisticated instruments, substances were able to be investigated and rudimentarily manipulated at the nano-scale, enabling the realization and implementation of the "nano" concept proposed decades ago.

Another reason why the nanotechnology gained its prosperity in recent decades is its vast interdisciplinary collaboration and a favorable interaction with practical applications. The nanotechnology covers a broad range of disciplines, including primarily chemistry, physics, biology, materials science, electronics, engineering, pharmaceutics, and environmental science. Because of that, the nanotechnology is a versatile approach to address many engineering problems, as illustrated in Figure 1.1. Among all these applications, the variety of the approaches and methodologies in nanotechnology falls into two categories: "bottom-up" and "top-down". As

the name suggests, in the bottom-up approach, substances (atoms, molecules, etc.) are selectively assembled to build up nanostructures [7]. For example, the layer-by-layer self-assembly of polyelectrolytes with various interactions (electrostatic interaction, hydrogen bond, etc.) to form a multilayer system is a typical bottom-up approach [8]. On the other hand, in the top-down approach, materials or patterns start with a larger scale are tailored into nano-scale for desired functionalities and/or properties [7]. For example, the lithography methodology for microchip and electronic device fabrication is a typical top-down approach [9]. Figure 1.2 elucidates the classification of various techniques and applications with the two categories.

With enormous research attention and efforts, up to now, the nanotechnology has covered a large and diverse spectrum of engineering applications, from the fabrication of nano-sized metal catalyst for chemical synthesis [10] to the lithography methodology for electronic devices manufacturing [11], from the molecular level self-assembly for multilayer polymeric composites [8] to the fabrication and integration of nano-scale materials for solar cell and hydrogen storage purposes [12], from the newly discovered carbon-based materials (carbon nanotube, graphene, graphite, etc.) for new devices and composites with enhanced properties [13] to the nano-fabrication of revolutionary devices and materials for drug delivery purposes [14], from the functionalized nanoparticle coated membranes for waste water treatment [15] to the synthesis and application of nanoparticle based biosensor for detection of proteins with ultra-sensitivity [16], so on and so forth.

The aim of the dissertation herein, however, is not to thoroughly discuss the full spectrum of the nanotechnology application. Rather, the dissertation will mainly focus on the nanotechnology application in the following three topics: biomass pretreatment in biofuel

production, functional material fabrication and surface modification. The topics will be discussed in detail in the following sections.

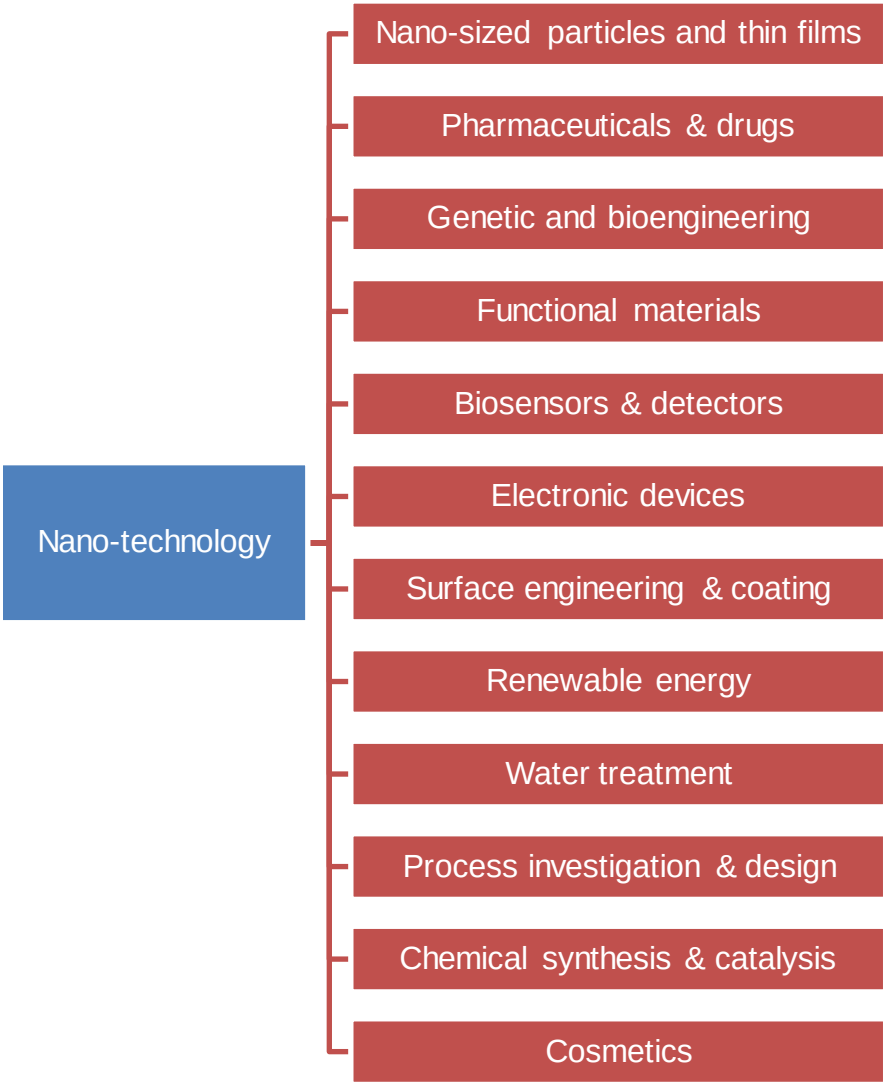

Figure 1.1 Diverse applications of nanotechnology. (For interpretation of the references to color in this and all other figures, the reader is referred to the electronic version of this dissertation.)

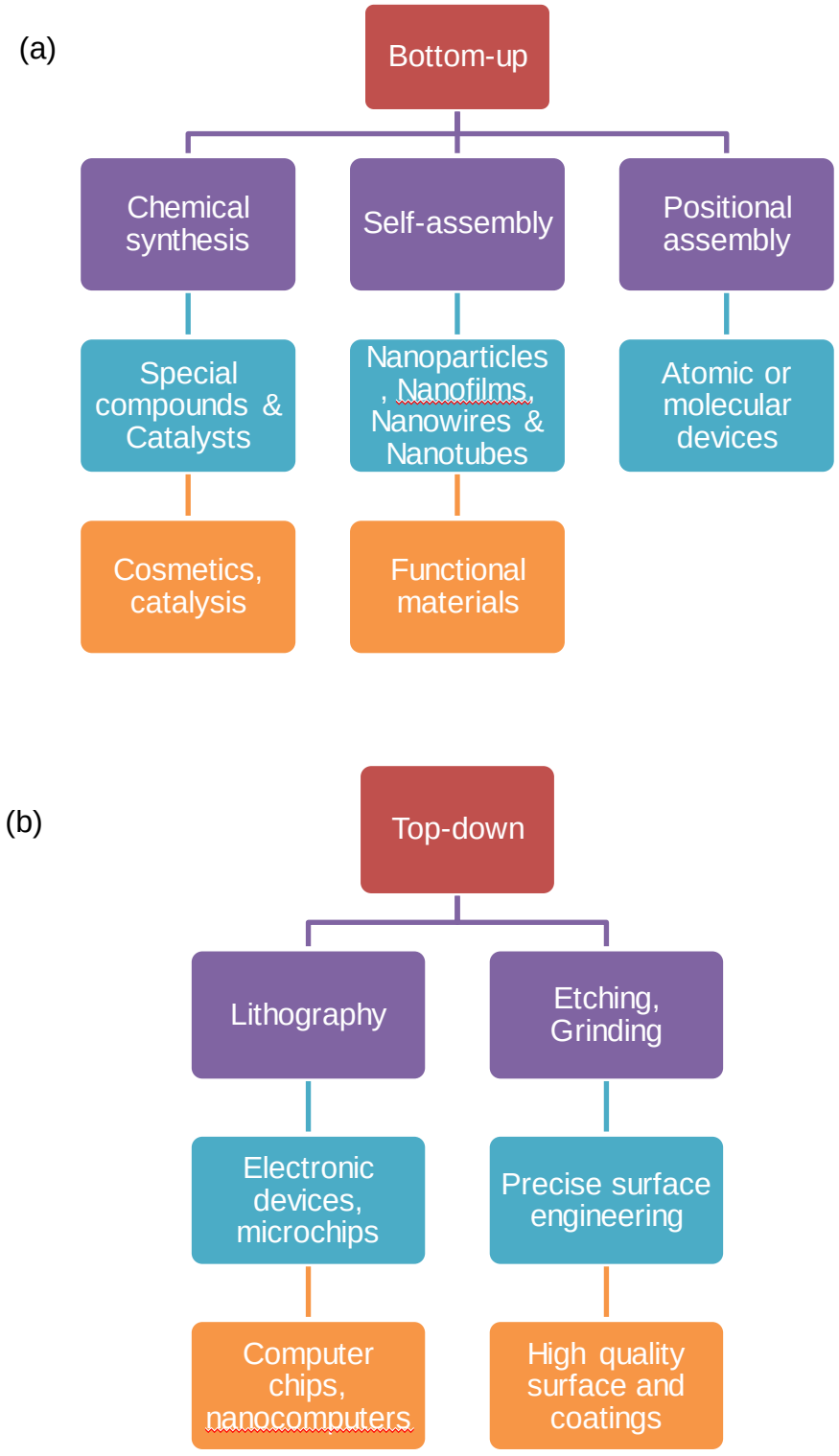

Figure 1.2 The Bottom-up (a) and Top-down (b) approaches in nanotechnology application. Reproduced with permission from Ref [17].

1.2 Nanotechnology for biofuel production

Concerns about decreasing petroleum supplies vs. increasing demands, and environmental consequences of fossil fuels (e.g., greenhouse gas emission) have motivated the research and development of renewable biofuel production in the recent decade [18]. The lignocellulosic biomass has been recognized as the sustainable resource to produce biofuels with environmental benefits (less greenhouse gas emissions) [19-21], and abundant quantities without reducing food supplies [22, 23].

The lignocellulosic biomass refers to plants or agricultural residues that are majorly composed of cellulose (38-50 %), hemicellulose (23-32 %) and lignin (15-25 %), as well as other minor components (e.g., protein, pectins, extractives) [24]. Cellulose is a homopolysaccharide of glucose, linked by β-1,4 glycosidic bonds. Hydrogen bonds are formed to associate cellulose within chains (intramolecular) and between chains (intermolecular). Hemicellulose is a heteropolysaccharide of pentoses (e.g., xylose, arabinose) and hexoses (e.g., glucose, mannose, galactose). It also contains uronic acids, acetate and phenolic groups. Lignin is a complex heteropolymer of three different polyphenolic compounds, *p*-coumaryl, coniferyl and sinapyl alcohol.

Three primary strategies have been proposed and developed for biofuel production from lignocellulosic biomass, including gasification and fuel derivation, bio-oil production by fast pyrolysis or liquefaction, as well as ethanol production by hydrolysis and fermentation [25]. Gasification of biomass is a process in which biomass reacts with steam, oxygen or air to produce syn-gas (i.e., CO and H_2), or producer gas (i.e., N_2, CO_2, CO, H_2) [26]. The syn-gas can be utilized to produce synthetic diesel, methanol or methanol-derived fuels [26-28]. Pyrolysis is thermal decomposition of feedstock without oxygen or steam [28-30]. Fast pyrolysis (or flash

pyrolysis) is usually applied at a high temperature (400-650 °C) and moderate pressure (1-5 atm) with an extremely short residence time (less than 2 seconds) for a high liquid yield (> 50 %). Liquefaction is a process to liquefy the feedstock under a high pressure (50-200 atm) and a high temperature (250-325 °C) [28, 31]. Compared with the aforementioned two strategies, conversion of lignocellulosic biomass to ethanol requires lower temperature and pressure, with high selectivity. Conversion of lignocellulosic biomass to ethanol is a multistep process, in which polysaccharides are depolymerized by either acid or specific enzymes to monomeric sugars (pentoses or hexoses), and the resulting sugars are fermented to ethanol by yeasts [32, 33]. A simultaneous saccharification and fermentation (SSF) process is developed to reduce the reactor cost and reaction time [34, 35].

During the advances of science and technology in biofuel production, the nanotechnology has played a significant role, from at least two aspects.

The instrumentation with nano-scale or sub nano-scale resolution facilitated a comprehensive understanding of the ultrastructure of the cell wall and the microscopic investigation on cell wall deconstruction and enzymatic mechanisms. This aspect of nanotechnology has been a long-term contribution to the biofuel production fields and is continuing to make contributions with the invention of more sophisticated instrumentation and advances in sample preparation techniques. For example, with the help of AFM, the diameter of a cellulose fibril is found to be around 3-5 nm [22]. With electron microscopy, AFM and other characterization methods, a multi-scale study on visualization of lignocellulosic biomass cell wall deconstruction during pretreatment was carried out [36]. The highly porous cell wall structure with a pore size from 10 to 1000 nm was formed within the plant cell walls and found to be beneficial for enzyme accessibility to cellulose. In another study, by applying the tapping

mode of AFM, the enzymatic hydrolysis of cellulose was visualized [37]. The observation significantly enhanced understanding of the mechanism of interactions between the enzyme and the cellulose fibrils.

The other aspect of the nanotechnology for biofuel production, however, is on the processing and development of new catalysts/materials at a nano-scale. This aspect of nanotechnology is more recent and diverse and is gaining more attention in the scientific community. Many solid acid catalysts, including zeolites [38, 39], transition metal oxides [40-42], supported carbonaceous solid acid catalysts [43-45] have been applied. Zeolites are widely used in chemical catalysis because they are non-toxic, easy to recover and reuse. Zhang and Zhao [38] performed cellulose hydrolysis with an H-zeolite catalyst in ionic liquid in a microwave reactor, and achieved a 37 % glucose yield in 8 min. Macromolecular Lewis acid compounds supported by zeolites are named heteropoly compounds [46, 47]. Heteropoly compounds (e.g., $H_3PW_{12}O_{40}$) may possess acidic strength as strong as sulfuric acid. Therefore, with the zeolite support, they exhibited catalytic activity in cellulose hydrolysis with thermal stability. A glucose yield of 30 % was reported under 160 °C for 6 hours of reaction time [47]. Transition-metal oxides have been found with catalytic activity for cellulose hydrolysis, and are also easy to recover and reuse. Tagusagawa *et al*. [40] found the mesoporous Nb-W oxides (Nb:W=3:7) compound a recyclable, highly active solid acid catalyst for cellulose hydrolysis. Carbonaceous solid acid catalysts are prepared by carbonizing D-glucose or sucrose at 400 °C under N_2 and then sulfonating the materials at 150 °C [43]. The catalyst was used to catalyze the transesterification of vegetable oil for biodiesel production [44]. Carbonaceous solid acid catalysts manufactured in the nano-scale (10-100 nm) were also studied for cellulose hydrolysis [48]. A high catalytic performance and excellent recyclability were observed.

Nanoparticle catalysts have also been found interesting in the biofuel production area due to its high surface area to volume ratio and recyclability. For example, in a recent study, cellulase was immobilized on polyvinyl alcohol/Fe_2O_3 magnetic nanoparticles, resulting in a three times improvement in glucose yield, and a 40 % enzymatic activity after four cycles of reuse [49]. Chang *et al.* [50] used mesoporous silica nanoparticles as scaffolds for the cellulase immobilization, the results showed an 80 % cellulose-to-glucose conversion with excellent stability. Fang *et al.* [51] synthesized hydrotalcite nanoparticles and activated it with $Ca(OH)_2$ to hydrolyze cellulose. A maximum yield of 47 % was achieved, with high selectivity (85 %) and stability.

1.3 Nanotechnology for functional material fabrication

Nanotechnology is also a versatile approach to fabricate functional materials. As introduced in previous sections, the methodologies are described as "top-down" and "bottom-up" approaches. The top-down approach, which usually involves patterning with lithography and etching, has gained its tremendous success in microelectronics. However, the research interest in the scientific community has shifted to the "bottom-up" approach, due to the introduction and development of nano-scale building blocks [52].

The nano-scale building blocks have to fulfill the requirement that at least one dimension falls into the nanometer scale. Regardless of the geometries, those nano-sized materials can be colloidal, crystalline, semi-crystalline, polymeric, metallic or metallic oxide.

Nanowires [52-54], nanorods [55, 56] and nanobelts [57, 58] are typical examples for one-dimensional (1-D) nano-scale building blocks. They can be concentric, ring-shape, round, hexagonal, square or triangular in cross section. They are anisotropic, with high aspect ratio.

These 1-D nano-scale building blocks can be used or modified with various functionalities/applications, including nano-scale electronic devices enabled by electron transport property [59], nanosensing applications enabled by interactions with DNA [60], charge storage behavior enabled by a functionalized molecule on the nanowire surface [61], enhanced optical and electromagnetic property enabled by the nonlocal dielectric function [62], and so on.

Nanosheets [63, 64] and nanolayers [65, 66] are examples for two-dimensional (2-D) nano-scale building blocks. They usually have high width-to-thickness ratio, and can be modified with surface properties. For example, Sasaki and Watanabe [67] obtained a nanosheet of quasi-TiO_2 by delaminating titanate, and found the nanosheet with subnanometer thickness with enhanced optical properties. In another study, Hosono *et al*. [68] fabricated and applied nanocrystalline ZnO sheets in dye-sensitized solar cells, obtained a higher conversion efficiency for 1.5 AM illumination. Vu *et al*. [66] dispersed clay nanolayers into synthetic and epoxidized natural rubber and obtained an enhanced mechanical property. Graphene nanosheet is another typical kind, which consists of sp2 bonded carbon atoms with one-atomic thickness [64]. The invention of graphene nanosheet won the Nobel Prize for Physics in 2010 [69]. And it is attracting a growing amount of research attention because of its unique and superior electronic, optical, magnetic, thermal and mechanical properties, as well as its facile way of preparation [70]. Because of that, an intensive research effort is to incorporate graphene nanosheets in polymers to form graphene-polymer composite materials for enhanced electrical and thermal conductivity, and mechanical strength [71]. The intrinsic chemical structure of the graphene also gives rise to other properties when chemically modified or paired with other chemical compounds. For example, an enhanced electrocatalytic activity of platinum (Pt) clusters supported on graphene nanosheets was observed for methanol oxidation reaction [64].

Nanoparticles or nanospheres [72, 73] are typical examples for three-dimensional (3-D) nano-scale building blocks. This area of research also has received a considerable attention for decades. The idea to incorporate nanoparticles was developed initially to enhance the mechanical strength of polymers [74, 75]. While the renewing research interests persist even at present due to the development of new fabrication methodologies and application of new materials, the research attention is somewhat branched to the functionalization of the nanoparticle surface and utilization of these newly developed material/structure for advanced uses. Magnetic nanoparticles have been used in medical diagnoses, such as application for magnetic resonance imaging and diagnose for cancer [76]. The mono-dispersed polystyrene nanoparticles with or without surface functional group have been commercially available for a long time and widely used in biomedical applications [77]. With the emulsion polymerization method and help of surfactants, the size of the resultant polystyrene can be precisely controlled with a variation less than 5 %. Also, the nanoparticles can be surface modified with polymer brushes [78], self-assembly monolayers [79], and polyelectrolyte multilayers [80] for unique characteristics and/or special purposes.

Although starting from the nano-scale, the nanotechnology can also be useful for macro/bulk applications and functionalities. For example, in civil infrastructures, smart concrete (concrete integrated with carbon nanofiber or carbon black) has been used in the past decade [81, 82]. The smart concrete was used to sense strain due to its piezoresistance, and to sense damage due to the relationship between damage and resistance. Han *et al*. [83] used the self-sensing smart concrete pavement for traffic flow detection. Veedu [84] presented the potential for bridges made of the smart concrete to monitor structural health, integrity and traffic information over the bridge, as well as the highway made of the same material to track traffic information *in*

situ. In solid mechanics, other than numerous study on mechanical enhancement of carbon based material fillers (graphene, graphite, carbon nanotube, etc.) in polymer matrix, Qu and Dai [85] mimicked the lizard's feet and fabricated carbon nanotube based dry adhesive surfaces, and showed a 473 g stainless steel was hung on a 4 mm × 4 mm SiO_2/Si-wafer-supported single wall nanotube dry adhesive film.

1.4 Nanotechnology for surface modification

Nanotechnology is a powerful tool for surface modification and engineering. With designated purposes, surfaces can be deliberately modified by making use of various surface interactions between homogeneous/heterogeneous materials. The surface interactions to cause adhesion phenomena generally include the following: covalent bonding, hydrogen bonding, electrostatic interaction, van der Waals interaction, and hydrophobic interaction. In general, the orders of strength are as follows: covalent bonding > electrostatic interaction > hydrophobic interaction > hydrogen bonding > van der Waals interaction.

Covalent bonding is a strong chemical linkage that shares a pair of electrons between atoms [86]. It forms when the bonded atoms have a total energy that is lower than the separate ones. In the surface application in nanotechnology, the covalent bond has been applied to functionalize nanoparticles for various purposes. For example, Yamanoi *et al*. [87] immobilized a series of omega-alkene-1-thiol-stablized gold nanoparticles onto silicon surfaces by Si-C covalent bonds. Zhou *et al*. [88] implanted functionalized Fe_3O_4 nanoparticles onto the functionalized multi-walled carbon nanotube (MWCNT) and observed a stronger magnetic performance. In their research, poly (acrylic acid) (PAA) was grafted onto the hydroxyl modified MWCNT and facilitated the covalent bonding between the amino groups of functionalized

Fe_3O_4 and the carboxyl groups of PAA. He *et al*. [89] reported a similar methodology to immobilize Fe_3O_4 nanoparticles to graphene oxide through covalent bonding, induced by the amino groups of functionalized nanoparticles and the carboxyl groups of functionalized graphene oxide.

Electrostatic interaction is another type of strong interaction which represents attractive (oppositely charged) or repulsive (with the same charge) forces between charged atoms or molecules [90]. The electrostatic interactions have been extensively used in construction of multicomposite films of charged substances (mostly polyelectrolytes) through layer-by-layer assembly from aqueous solution, since the early 1990s [8, 91]. With electrostatic attraction forces, polycations and polyanions can be alternatively deposited onto designated substrates, regardless of their size, geometry and topology. The methodology and its mechanism have received great attention and have led to a wide range of applications. For example, Caruso *et al*. [92] reported an electrostatic self-assembly of silica nanoparticles onto positively charged polystyrene particles, which are surface modified by polyelectrolyte multilayers. Wang *et al*. [93] electrostatically assembled hydrolyzed poly[2-(3-thienyl) ethanol butoxy carbonyl-methyl urethane] onto the surface of cellulose acetate electrospun nanofibrous membranes, and obtained a high optical sensitivity. Agarwal *et al*. [94] investigated the polyelectrolyte multilayer coated drug nanoparticles and found that the coating prevents nanoparticle aggregation, and the drug release rate could be controlled.

Hydrophobic and hydrophilic interactions [90] are ubiquitous interactions occurring in aqueous solution. They are moderate interactions, weaker than covalent bonding, stronger than hydrogen bonding and van der Waals interaction in aqueous environment. In hydrophobic interaction, non-polar substances (water insoluble molecules) exhibits a “water-repulsive”

behavior and tends to aggregate with each other [90, 95]. On the contrary, hydrophilic interaction is an interaction between water molecule and other molecules in which they tend to attract to each other [90]. Hydrophobic interaction is more widely used for many purposes due to these characteristics. By making use of the hydrophobic interaction, Akagi *et al.* [96] developed a way to stabilize polyelectrolyte complex nanoparticles, and expected a great potential to apply those nanoparticles as multifunctional carriers for pharmaceutical and biomedical applications. Song *et al.* [97] studied attachment of modified silver nanoparticles to hydrophobic glass beads, and suggested that the hydrophobic interaction plays a significant role to increase the attachment efficiency by at least 2-fold.

Hydrogen bonding is a relatively weak interaction in which a hydrogen atom of one molecule is attracted to an electronegative atom of another molecule [86]. Hydrogen-bonded architectures are abundant in biological systems (e.g., hydrogen bonding in cellulose fibrils), and are found useful in many nanotechnology applications. Russell and Ward [98] exhibited an interesting study, in which hydrogen bonded molecular crystals are designed and synthesized with dimension control. Examples included one-dimensional hydrogen bonded wires, two-dimensional hydrogen bonded layers and nanoporous hydrogen bonded lattices. In another study, Zhang *et al.* [99] investigated the self-assembly of polyaniline nanotubes in the presence of carboxylic acids. It was found that the hydrogen bonds between the polymer chain and the hydroxyl group of the carboxylic acids are responsible to form aggregated nanotube dendrites. Lee and Han [100] studied viscoelastic properties of hydrogen bonded polycarbonate/organoclay nanocomposites, and found that organoclay platelets are well dispersed in hydrogen bonded nanocomposites.

Van der Waals interaction is a weak interaction that induced by electrical interactions between atoms or molecules that are close to each other [86]. It is the weakest intermolecular interaction, but occurs ubiquitously in nature. Despite of its weak strength, it is applied in many aspects in nanotechnology. For example, Sato and Sano [101] demonstrated a methodology to deposit single-walled carbon nanotubes on to a substrate surface and develop a 2D network that is held by van der Waals interaction. Researchers put many efforts into mathematical simulation to describe the van der Waals interaction with nanomaterial/nanostructures. For example, Blagov *et al*. [102] developed Lifshitz-type formulas to describe van der Waals interaction between an atom/molecule and a single-walled carbon nanotube. Another effort by Gatica *et al*. [103] calculated van der Waals forces between spherical, cubic and core-shell nanoparticles in vacuum, using the Axilrod-Teller-Muto 3-body formulation.

1.5 Scope of the dissertation

The dissertation is committed to comprehensively describing and discussing the three research projects conducted by the author during his PhD program.

In the second chapter, a fast and efficient nano-scale shear hybrid alkaline (NSHA) pretreatment method of lignocellulosic biomass is introduced. In this work, corn stover was pretreated in a modified Taylor-Couette reactor with alkali (sodium hydroxide) at room temperature, with a two-minute retention time and a 12500 s^{-1} shear rate. A nanomixer was used as the modified Taylor-Couette reactor to perform the NSHA pretreatment process. The synergistic effects (chemical, physical and thermal effects) induced by the nanomixer aimed to disrupt the naturally-formed recalcitrance of biomass that prevents itself from chemical or biological attacks. Results showed that the NSHA pretreatment caused an efficient structural

breakdown and substantially enhanced the accessibility of enzymes to polysaccharides. An up to 82 % of high cellulose content in the remaining solid was achieved with the NSHA pretreatment process. Compared with untreated corn stover, an approximately 4-fold increase in enzymatic cellulose conversion and a 5-fold increase in hemicellulose conversion were achieved. SEM images revealed that a severe disruption of biomass structure and exposure of cellulose microfibril aggregates in NSHA pretreated corn stover. The highly efficient nano-scale hybrid process has a potential to be economical, and therefore to decrease the overall cost of biomass conversion which is critical to accomplish an economic biofuel production from biomass.

In the third chapter, a nano-deposition strategy was developed to enhance the energy absorption capacity of aluminum (Al) open-cell foams. Open cell Al foams have been used as energy absorbers for decades, due to their unique compressive stress-strain responses. Their energy absorption capacity can be enhanced by thickening the foam struts, or increasing the foam's relative density. However, the enhancement is compromised by the inherent characteristics of its stress-strain property relationship, whereby upon homogeneous strut thickening, an increase in the plateau stress without a reduction in densification strain cannot be achieved. The nano-reinforcement exhibits the potentials of providing superior mechanical properties over the conventional not only at the micro-scale but also at the macro-scale level. Unlike homogeneously thickening the foam struts, the heterogeneous nano-reinforcement has potentials to favor a higher plateau stress and a longer densification strain, which is a promising feature to enhance the energy absorption capacity of cellular foams. In this chapter, nano-crystalline copper (Cu) was uniformly deposited onto the Al foam and novel 3-D Cu/Al, heterogeneously thickened, composite foam structured materials were fabricated and tested for the first time. A featured non-cyanide nano-crystalline copper electro-deposition system was

setup for the coating of open-cell Al foam, and, the energy absorption capacity as a function of foam pore size and Cu coating thickness was investigated. The x-ray diffraction tests confirmed the crystallinity of the Cu deposition and the crystallite size was calculated to be 38 nm. The energy absorption capacity of Al foams (with average strut thickness of 192 μm) reinforced with a 60 μm Cu coating was 3 times greater than that of plain foams. The compressive stress-strain response of the composite samples showed no significant reduction of the densification strain compared to the uncoated foams due to the small change in the foam strut thickness and pore size. A comparison between thin Cu-coated and uncoated Al foam samples with the same overall strut thickness (i.e., same effective volume density and porosity) showed that the nano-reinforced foams had superior energy absorption capacity over plain foams with the same overall thickness, with almost a 2-time enhancement.

In the fourth chapter, a facile "dip & rinse" method for nickel (Ni) electroless deposition on hydrophobic polymer surfaces was developed. The electroless deposition is widely used because of its equipment simplicity and versatility. Electroless metal deposition is a catalytic, redox reaction of a metal ion in an aqueous solution (with a reducing chemical agent), without external electrical field being applied. It usually includes three main steps: 1) a surface treatment or conditioning; 2) application of an appropriate catalyst (typically noble metal catalyst, e.g. tin, palladium) on the substrate surface; 3) metal electroless deposition. Rinsing is required between the steps. However, in the first step, in order to modify the functionality of the substrate surface so that catalyst can be sequentially attached, harsh or/and toxic surface conditioning steps are usually employed. To eliminate the need for harsh and toxic treatment of the substrate, this chapter demonstrated a facile method of electroless Ni deposition on various hydrophobic polymer substrates, by making use of the hydrophobic interactions between Poly(allylamine

hydrochloride) (PAH) and polymer substrates for catalyst adsorption/immobilization. Various hydrophobic polymer surfaces with different geometries and dimensions, including low density polyethylene (LDPE), high density polyethylene (HDPE), polypropylene (PP) and polystyrene (PS) thin sheets, and PE pellets were tested and Ni was successfully deposited onto all these surfaces. Studies showed that without the PAH, Ni coating was not able to form on any of these surfaces. Among these polymer thin sheets, with the same experiment condition and procedure, coverage of Ni coating can be ranked in the following order: PS > PP ≈ HDPE > LDPE. A kinetic study on polymer thin sheets examples showed that with 2 hours of deposition, an approximately 2 μm thickness was achieved. A prove-of-concept study showed that Ni coated polymer thin sheets can be further electroplated with heterogeneous metal (Cu), hence enabling a faster thickness growth over time.

REFERENCES

REFERENCES

1. Maynard AD, Aitken RJ, Butz T, Colvin V, Donaldson K, Oberdörster G, et al. Safe handling of nanotechnology. Nature 2006;444(7117): 267-269.

2. Feynman RP. Plenty of Room at the Bottom. 1959; Available from: www.its.caltech.edu/~feynman/plenty.html.

3. Tersoff J, Hamann D. Theory and application for the scanning tunneling microscope. Physical Review Letters 1983;50(25): 1998-2001.

4. Tersoff J, Hamann D. Theory of the scanning tunneling microscope. Physical Review B 1985;31(2): 805-813.

5. Binnig G, Quate C, Gerber C. Atomic force microscope. Physical Review Letters 1986;56(9): 930-933.

6. Martin Y, William C, Wickramasinghe H. Atomic force microscope force mapping and profiling on a sub 100-A scale. Journal of Applied Physics 1987;61(10): 4723-4729.

7. Mijatovic D, Eijkel J, Berg Avd. Technologies for nanofluidic systems: top-down vs. bottom-up - a review. Lab on a Chip 2005;5(5): 492-500.

8. Decher G. Fuzzy nanoassemblies: toward layered polymeric multicomposites. Science 1997;277(5330): 1232-1237.

9. Pauliac S, Landis S, Foucher J, Thiault J, Faynot O. Hybrid lithography process for nano-scale devices. Microelectronic Engineering 2006;83(4-9): 1761-1766.

10. Phan N, Sluys MVD, Jones C. On the nature of the active species in palladium catalyzed Mizoroki-Heck and Suzuki-Miyaura couplings - homogeneous or heterogeneous catalysis, a critical review. Advanced Synthesis & Catalysis 2006;348(6): 609-679.

11. Campbell M, Sharp D, Harrison M, Denning R, Turberfield A. Fabrication of photonic crystals for the visible spectrum by holographic lithography. Nature 2000;404(6773): 53-56.

12. Mao SS, Chen X. Selected nanotechnologies for renewable energy applications. International Journal of Energy Research 2007;31(6-7): 619-636.

13. Novoselov K, Geim A, Morozov S, Jiang D, Zhang Y, Dubonos S, et al. Electric field effect in atomically thin carbon films. Science 2004;306(5696): 666-669.

14. Duncan R. The dawning era of polymer therapeutics. Nature Reviews Drug Discovery 2003;2(5): 347-360.

15. Pendergast MM, Hoek EMV. A review of water treatment membrane nanotechnologies. Energy & Environmental Science 2011;4(6): 1946-1971.

16. Nam JM, Thaxton CS, Mirkin CA. Nanoparticle-based bio-bar codes for the ultrasensitive detection of proteins. Science 2003;301(5641): 1884-1886.

17. Nanoscience and nanotechnologies: opportunities and uncertainties. Royal Society and Royal Academy of Engineering; 2004.

18. Hill J, Nelson E, Tilman D, Polasky S, Tiffany D. Environmental, economic, and energetic costs and benefits of biodiesel and ethanol biofuels. Proceedings of the National Academy of Sciences of the United States of America 2006;103(30): 11206-11210.

19. Wyman CE. Alternative fuels from biomass and their impact on carbon dioxide accumulation. Applied Biochemistry and Biotechnology 1994;45-46(1): 897-915.

20. Börjesson P. Good or bad bioethanol from a greenhouse gas perspective - what determines this? Applied Energy 2009;86(5): 589-594.

21. Wyman CE, Hinman ND. Ethanol fundamentals of production from renewable feedstocks and use as a transportation fuel. Applied Biochemistry and Biotechnology 1990;24-25(1): 735-753.

22. Himmel ME, Ding S-Y, Johnson DK, Adney WS, Nimlos MR, Brady JW, et al. Biomass recalcitrance: engineering plants and enzymes for biofuels production. Science 2007;315(5813): 804-807.

23. Sáncheza ÓJ, Cardona CA. Trends in biotechnological production of fuel ethanol from different feedstocks. Bioresource Technology 2008;99(13): 5270-5295.

24. Fengel D, Wegener G. Wood: Chemistry, Ultrastructure, Reactions. Munchen, Germany: Walter De Gruyter Inc; 1984.

25. Huber GW, Iborra S, Corma A. Synthesis of transportation fuels from biomass: chemistry, catalysts, and engineering. Chemical Reviews 2006;106(9): 4044-4098.

26. Sutton D, Kelleher B, Ross JRH. Review of literature on catalysts for biomass gasification. Fuel Processing Technology 2001;73(3): 155-173.

27. BRIDGWATER A. The technical and economic-feasibility of biomass gasification for power-generation. Fuel 1995;74(5): 631-653.

28. Klass DL. Biomass for Renewable Energy, Fuels, and Chemicals. San Diego, CA: Academic Press; 1998.

29. Mohan D, U.Pittman JC, Steele PH. Pyrolysis of wood/biomass for bio-oil: A critical review. Energy & Fuels 2006;20(3): 848-889.

30. Czernik S, Bridgwater A. Overview of applications of biomass fast pyrolysis oil. Energy & Fuels 2004;18(2): 590-598.

31. Demirbas A. Mechanisms of liquefaction and pyrolysis reactions of biomass. Energy Coversion and Management 2000;41(6): 633-646.

32. Lynd L, Cushman J, Nichols R, Wyman C. Fuel ethanol from cellulosic biomass. Science 1991;251(4999): 1318-1323.

33. Hamelinck C, Hooijdonk Gv, Faaij A. Ethanol from lignocellulosic biomass: techno-economic performance in short-, middle- and long-term. Biomass & Bioenergy 2005;28(4): 384-410.

34. Wyman C. Ethanol from lignocellulosic biomass - technology, economics and opportunities. Bioresource Technology 1994;50(1): 3-16.

35. Ballesteros M, Oliva J, Negro M, Manzanares P, Ballesteros I. Ethanol from lignocellulosic materials by a simultaneous saccharification and fermentation process (SFS) with Kluyveromyces marxianus CECT 10875. Process Biochemistry 2004;39(12): 1843-1848.

36. Chundawat SPS, Donohoe BS, Sousa LdC, Elder T, Agarwal UP, Lu F, et al. Multi-scale visualization and characterization of lignocellulosic plant cell wall deconstruction during thermochemical pretreatment. Energy & Environmental Science 2010;4(3): 973-984.

37. Liu H, Fu S, Zhu J, Li H, Zhan H. Visualization of enzymatic hydrolysis of cellulose using AFM phase imaging. Enzyme and Microbial Technology 2009;45(4): 274-281.

38. Zhang Z, Zhao ZK. Solid acid and microwave-assisted hydrolysis of cellulose in ionic liquid. Carbohydrate Research 2009;344(15): 2069-2072.

39. Onda A, Ochi T, Yanagisawa K. Selective hydrolysis of cellulose into glucose over solid acid catalysts. Green Chemistry 2008;10(10): 1033-1037.

40. Tagusagawa C, Takagaki A, Iguchi A, Takanabe K, Kondo JN, Ebitani K, et al. Highly active mesoporous Nb-W oxide solid-acid catalyst. Angewandte Chemie International Edition 2010;49(6): 1128-1132.

41. Kondo JN, Yamashita T, Nakajima K, Lu D, Hara M, Domen K. Preparation and crystallization characteristics of mesoporous TiO_2 and mixed oxides. Journal of Materials Chemistry 2005;15(20): 2035-2040.

42. Takagaki A, Tagusagawa C, Domen K. Glucose production from saccharides using layered transition metal oxide and exfoliated nanosheets as a water-tolerant solid acid catalyst. Chemical Communications 2008(42): 5363-5365.

43. Zong M-H, Duan Z-Q, Lou W-Y, Smith TJ, Wu H. Preparation of a sugar catalyst and its use for highly efficient production of biodiesel. Green Chemistry 2007;9(5): 434-437.

44. Toda M, Takagaki A, Okamura M, Kondo JN, Hayashi S, Domen K, et al. Green chemistry: biodiesel made with sugar catalyst. Nature 2005;438(7065): 178-178.

45. Fukuhara K, Nakajima K, Kitano M, Kato H, Hayashi S, Hara M. Structure and catalysis of cellulose-derived amorphous carbon bearing SO(3)H groups. ChemSusChem 2011;4(6): 778-784.

46. Okuhara T, Mizuno N, Misono M. Catalytic chemistry of heteropoly compounds. In: D.D. Eley WOH, Bruce G, editors. Advances in Catalysis: Academic Press; 1996. p. 113-252.

47. Tian J, Fang C, Cheng M, Wang X. Hydrolysis of cellulose over CsxH3–xPW12O40 (x = 1–3) heteropoly acid catalysts. Chemical Engineering & Technology 2011;34(3): 482-486.

48. Yamaguchi D, Kitano M, Suganuma S, Nakajima K, Kato H, Hara M. Hydrolysis of cellulose by a solid acid catalyst under optimal reaction conditions. The Journal of Physical Chemistry C 2009;113(8): 3181-3188.

49. Liao H, Chen D, Yuan L, Zheng M, Zhu Y, Liu X. Immobilized cellulase by polyvinyl alcohol/Fe2O3 magnetic nanoparticle to degrade microcrystalline cellulose. Carbohydrate Polymers 2010;82(3): 600-604.

50. Chang RH-Y, Jang J, Wu KC-W. Cellulase immobilized mesoporous silica nanocatalysts for efficient cellulose-to-glucose conversion. Green Chemistry 2011;13(10): 2844-2850.

51. Fang Z, Zhang F, Zeng H-Y, Guo F. Production of glucose by hydrolysis of cellulose at 423 K in the presence of activated hydrotalcite nanoparticles. Bioresource Technology 2011;102(17): 8017-8021.

52. Lieber CM, Wang ZL. Functional nanowires. Mrs Bulletin 2007;32(2): 99-108.

53. Law M, Greene L, Johnson J, Saykally R, Yang P. Nanowire dye-sensitized solar cells. Nature Materials 2005;4(6): 455-459.

54. Cui Y, Wei QQ, Park HK, Lieber CM. Nanowire nanosensors for highly sensitive and selective detection of biological and chemical species. Science 2001;293(5533): 1289-1292.

55. Huynh WU, Dittmer JJ, Alivisatos AP. Hybrid nanorod-polymer solar cells. Science 2002;295(5564): 2425-2427.

56. Park WI, Yi GC. Electroluminescence in n-ZnO nanorod arrays vertically grown on p-GaN. Advanced Materials 2004;16(1): 87-90.

57. Wang ZL. ZnO nanowire and nanobelt platform for nanotechnology. Materials Science & Engineering R-Reports 2009;64(3-4): 33-71.

58. Zhao MH, Wang ZL, Mao SX. Piezoelectric characterization of individual zinc oxide nanobelt probed by piezoresponse force microscope. Nano Letters 2004;4(4): 587-590.

59. Cui Y, Lieber CM. Functional nanoscale electronic devices assembled using silicon nanowire building blocks. Science 2001;291(5505): 851-853.

60. Curreli M, Li C, Sun YH, Lei B, Gundersen MA, Thompson ME, et al. Selective functionalization of In_2O_3 nanowire mat devices for biosensing applications. Journal of the American Chemical Society 2005;127(19): 6922-6923.

61. Li C, Fan W, Straus DA, Lei B, Asano S, Zhang DH, et al. Charge storage behavior of nanowire transistors functionalized with bis(terpyridine)-Fe(II) molecules: Dependence on molecular structure. Journal of the American Chemical Society 2004;126(25): 7750-7751.

62. McMahon JM, Gray SK, Schatz GC. Optical properties of nanowire dimers with a spatially nonlocal dielectric function. Nano Letters 2010;10(9): 3473-3481.

63. Yoo E, Kim J, Hosono E, Zhou H, Kudo T, Honma I. Large reversible Li storage of graphene nanosheet families for use in rechargeable lithium ion batteries. Nano Letters 2008;8(8): 2277-2282.

64. Yoo E, Okata T, Akita T, Kohyama M, Nakamura J, Honma I. Enhanced electrocatalytic activity of Pt subnanoclusters on graphene nanosheet surface. Nano Letters 2009;9(6): 2255-2259.

65. Wang Z, Pinnavaia TJ. Nanolayer reinforcement of elastomeric polyurethane. Chemistry of Materials 1998;10(12): 3769-3771.

66. Vu YT, Mark JE, Pham LH, Engelhardt M. Clay nanolayer reinforcement of cis-1,4-polyisoprene and epoxidized natural rubber. Journal of Applied Polymer Science 2001;82(6): 1391-1403.

67. Sasaki T, Watanabe M. Semiconductor nanosheet crystallites of quasi-TiO2 and their optical properties. Journal of Physical Chemistry B 1997;101(49): 10159-10161.

68. Hosono E, Fujihara S, Honna I, Zhou HS. The fabrication of an upright-standing zinc oxide nanosheet for use in dye-sensitized solar cells. Advanced Materials 2005;17(17): 2091-2094.

69. Guo S, Dong S. Graphene nanosheet: synthesis, molecular engineering, thin film, hybrids, and energy and analytical applications. Chemical Society Reviews 2011;40(5): 2644-2672.

70. Geim AK, Novoselov KS. The rise of graphene. Nature Materials 2007;6(3): 183-191.

71. Stankovich S, Dikin DA, Dommett GHB, Kohlhaas KM, Zimney EJ, Stach EA, et al. Graphene-based composite materials. Nature 2006;442(7100): 282-286.

72. Shipway AN, Katz E, Willner I. Nanoparticle arrays on surfaces for electronic, optical, and sensor applications. Chemphyschem 2000;1(1): 18-52.

73. Haynes CL, Van Duyne RP. Nanosphere lithography: A versatile nanofabrication tool for studies of size-dependent nanoparticle optics. Journal of Physical Chemistry B 2001;105(24): 5599-5611.

74. Usukia A, Kojima Y, Kawasumi M, Okada A, Fukushima Y, Kurauchi T, et al. Synthesis of nylon 6-clay hybrid. Journal of Materials Research 1993;8(05): 1179-1184.

75. Kojima Y, Usuki A, Kawasumi M, Okada A, Fukushima Y, Kurauchi T, et al. Mechanical properties of nylon 6-clay hybrid. Journal of Materials Research 1993;8(5): 1185-1189.

76. Mornet S, Vasseur S, Grasset F, Duguet E. Magnetic nanoparticle design for medical diagnosis and therapy. Journal of Materials Chemistry 2004;14(14): 2161-2175.

77. Kim S, Kim CA, Choi YH, Jung MY. Synthesis of polystyrene nanoparticles with different surface modification by emulsion polymerization and measurement of IgG adsorption and stability for the application in latex-protein complex based solid-phase immunoassay. Polymer Bulletin 2009;62(1): 23-32.

78. Husseman M, Malmström EE, McNamara M, Mate M, Mecerreyes D, Benoit DG, et al. Controlled synthesis of polymer brushes by "living" free radical polymerization techniques. Macromolecules 1999;32(5): 1424-1431.

79. Bain CD, Whitesides GM. Molecular-level control over surface order in self-assembled monolayer films of thiols on gold. Science 1988;240(4848): 62-63.

80. Wang TC, Rubner MF, Cohen RE. Polyelectrolyte multilayer nanoreactors for preparing silver nanoparticle composites: Controlling metal concentration and nanoparticle size. Langmuir 2002;18(8): 3370-3375.

81. Nanotechnology in Civil Infrastructure: A Paradigm Shift. Gopalakrishnan K, Birgisson B, Taylor P, AttohOkine NO, editors. Berlin: Springer-Verlag Berlin; 2011. 1-272 p.

82. Xiao H, Li H, Ou J. Self-monitoring properties of concrete columns with embedded cement-based strain sensors. Journal of Intelligent Materials Systems and Structures 2011;22(2): 191-200.

83. Han B, Yu X, Kwon E. A self-sensing carbon nanotube/cement composite for traffic monitoring. Nanotechnology 2009;20(44): Article no. 445501.

84. Veedu VP, inventor; Oceanit Laboratories, Inc., assignee. Multifunctional cementitious nanocomposite material and methods of making the same. United States patent US007875211. 2011.

85. Qu L, Dai L. Gecko-foot-mimetic aligned single-walled carbon nanotube dry adhesives with unique electrical and thermal properties. Advanced Materials 2007;19(22): 3844-3849.

86. Atkins P, Jones L. Chemical Principles: The Quest for Insight, 4th edition. New York, NY: W.H. Freeman & Co.; 2008.

87. Yamanoi Y, Yonezawa T, Shirahata N, Nishihara H. Immobilization of gold nanoparticles onto silicon surfaces by Si-C covalent bonds. Langmuir 2004;20(4): 1054-1056.

88. Zhou HF, Zhang C, Li HQ, Du ZJ. Decoration of Fe_3O_4 nanoparticles on the surface of poly(acrylic acid) functionalized multi-walled carbon nanotubes by covalent bonding. Journal of Polymer Science Part a-Polymer Chemistry 2010;48(21): 4697-4703.

89. He FA, Fan JT, Ma D, Zhang LM, Leung C, Chan HL. The attachment of Fe3O4 nanoparticles to graphene oxide by covalent bonding. Carbon 2010;48(11): 3139-3144.

90. McQuarrie DA, Simon JD. Physical Chemistry: A Molecular Approach. Sausalito, CA: University Science Books; 1997.

91. Decher G, Hong J-D. Buildup of ultrathin multilayer films by a self-assembly process, 1 consecutive adsorption of anionic and cationic bipolar amphiphiles on charged surfaces. Makromolekulare Chemie Macromolecular Symposia 1991;46(1): 321-327.

92. Caruso F, Lichtenfeld H, Giersig M, Mohwald H. Electrostatic self-assembly of silica nanoparticle - polyelectrolyte multilayers on polystyrene latex particles. Journal of the American Chemical Society 1998;120(33): 8523-8524.

93. Wang XY, Kim YG, Drew C, Ku BC, Kumar J, Samuelson LA. Electrostatic assembly of conjugated polymer thin layers on electrospun nanofibrous membranes for biosensors. Nano Letters 2004;4(2): 331-334.

94. Agarwal A, Lvov Y, Sawant R, Torchilin V. Stable nanocolloids of poorly soluble drugs with high drug content prepared using the combination of sonication and layer-by-layer technology. Journal of Controlled Release 2008;128(3): 255-260.

95. Chandler D. Interfaces and the driving force of hydrophobic assembly. Nature 2005;437(7059): 640-647.

96. Akagi T, Watanabe K, Kim H, Akashi M. Stabilization of polyion complex nanoparticles composed of poly(amino acid) using hydrophobic interactions. Langmuir 2010;26(4): 2406-2413.

97. Song JE, Phenrat T, Marinakos S, Xiao Y, Liu J, Wiesner MR, et al. Hydrophobic interactions increase attachment of gum arabic- and PVP-coated Ag nanoparticles to hydrophobic surfaces. Environmental Science & Technology 2011;45(14): 5988-5995.

98. Russell VA, Ward MD. Molecular crystals with dimensionally controlled hydrogen-bonded nanostructures. Chemistry of Materials 1996;8(8): 1654-1666.

99. Zhang LJ, Long YZ, Chen ZJ, Wan MX. The effect of hydrogen bonding on self-assembled polyaniline nanostructures. Advanced Functional Materials 2004;14(7): 693-698.

100. Lee KM, Han CD. Effect of hydrogen bonding on the rheology of polycarbonate/organoclay nanocomposites. Polymer 2003;44(16): 4573-4588.

101. Sato M, Sano M. van der Waals layer-by-layer construction of a carbon nanotube 2D network. Langmuir 2005;21(24): 11490-11494.

102. Blagov EV, Klimchitskaya GL, Mostepanenko VM. Van der Waals interaction between a microparticle and a single-walled carbon nanotube. Physical Review B 2007;75(23): Article No. 235413.

103. Gatica SM, Cole MW, Velegol D. Designing van der Waals forces between nanocolloids. Nano Letters 2005;5(1): 169-173.

Chapter 2 Fast and efficient nanoshear hybrid alkaline pretreatment of corn stover for biofuel and materials production

2.0 Abstract

In this chapter, a fast and efficient nano-scale shear hybrid alkaline (NSHA) pretreatment method of lignocellulosic biomass is introduced. In this work, corn stover was pretreated in a modified Taylor-Couette reactor with alkali (sodium hydroxide) at room temperature for two minutes. An up to 82 % of cellulose content in the remaining solid was achieved with the novel NSHA pretreatment process. Compared with untreated corn stover, an approximately 4-fold increase in enzymatic cellulose conversion and a 5-fold increase in hemicellulose conversion were achieved. Compositional analysis proved significant removals of both lignin and hemicellulose after the NSHA pretreatment. SEM images revealed that the synergistic effect of NSHA pretreatment caused severe disruption of biomass structure and exposure of cellulose microfibril aggregates in NSHA pretreated corn stover.

2.1 Introduction

Alternatives for petroleum are urgently needed since worldwide oil depletion is approaching. Lignocellulosic biomass, such as corn stover, wheat straw, and switch grass *etc*. is believed to be the abundant and sustainable feedstock for biofuel, chemicals, and materials production [1]. Bioethanol production forms the carbon cycle in a more timely fashion compared to fossil fuel, which leads to the reduction of the greenhouse gas emission [2, 3].

Production of ethanol from lignocellulosic biomass is a multistep process, in which pretreatment step other than the power plant investment accounts for the largest cost portion, as high as 19 % [4]. Typically, lignocellulosic biomass pretreatment refers to an essential step to disrupt the natural polysaccharide-lignin shield that limits the accessibility of enzymes to cellulose and hemicellulose during saccharification. Intensive research has been conducted on this topic [5-8].

Over decades, much effort was continuously made to enable the pretreatment to be cost-competitive itself and beneficial to downstream processing as well. Chemical, physical, or thermal methods have been employed to enhance the biomass digestibility. Chemical effect is mainly made by inorganic alkalis and acids [9-14]. Different categories of chemicals, such as lime, sodium hydroxide, ammonia and sulfuric acid, are commonly used. By adding the alkali or acid, majority of lignin or hemicellulose is removed. Other chemicals, either added as a major component or additives, include oxidative chemical compounds [15-17] (e.g. hydrogen peroxide, ozone, etc.), organic solvents [18, 19] (e.g. ethylene glycol, acetylsalicylic and salicylic acids, ect.), and ionic liquids [20, 21] (e.g. 1-ethyl-3-methylimidazolium acetate, 1-n-butyl-3-methylimidazolium, etc.). Oxidative chemical compounds remove the hemicellulose and lignin to increase the accessibility of the cellulose. Organic solvents break the internal lignin and

hemicellulose bonds. Ionic liquid is used to extract lignin and reduce the crystallinity of cellulose. With the heat input to increase the pretreatment temperature, thermal effect takes place to increase the kinetic constant of the pretreatment, therefore reducing the retention time [22-24]. Physical methods mainly include milling, homogenization and flowthrough. Milling [25, 26] and homogenization [27] serve to reduce particle size and crystallinity as well as degree of polymerization of cellulose, which help to increase surface area and pore size. By applying flowthrough, a large portion of hemicellulose and lignin can be removed [28]. Recently, researchers have investigated a twin screw extrusion process [29-31] for the pretreatment process. The friction and high shear rate generated by the extruder enhanced the enzymatic accessibility of the woody biomass. Different effects are usually combined to make the polysaccharides more accessible to enzymes.

In this work, a novel NSHA pretreatment method is proposed for the first time. By applying the high velocity shearing along with synergistic mild chemical and thermal effects in a modified Taylor-Couette reactor, the high-shear shaft work can primarily be transferred to the nanostructure of biomass, allowing the efficient elimination of lignin and the exposure of polysaccharide in a very short time.

2.2 Experimental Sections

2.2.1 Materials

The corn stover (CS) was locally harvested at the cook farms (Okemos, MI, geographical coordinates 42.680164, 84.418455. Or 42° 40’ 48.59” North, 84° 25’ 6.44” West) in October 2009. The corn stover leaves and stalks were collected. After harvesting, the corn stover was washed with tap water and dried at 50 °C for 48 hrs. The dried corn stover was chopped and then

milled in a knife mill (Arthur H. Thomas Co., NJ, US), with a sieve size of 1 mm. The processed corn stover was stored in a freezer for future use. After the CS was transferred to the lab it was stored in a cold room at 4 °C.

Sodium hydroxide (NaOH, Spectrum Chemical mfg Co., CA, US) solution was prepared in stock for future use. Deionized (DI) water supplied by a Barnstead Nanopure-UV 4 stage purifier (Barnstead International Dubuque, Iowa), equipped with a UV source and final 0.2 μm filter with a resistance ≥18.0 MΩ·cm was used for aqueous solution preparation and washing.

2.2.2 Modified Taylor-Couette reactor (nanomixer)

T K Filmics nanomixer [32] (model 56-50, Primix Corporation, Japan) was used as a modified Taylor-Couette reactor to perform the NSHA pretreatment process. The nanomixer has an energy input of 5.5 kW. A schematic diagram of the nanomixer in batch operation is illustrated in Figure 2.1. The mixing unit mainly consists of 4 components, a shaft, driven by the motor, an overflow vessel and two concentric cylinders, a turbine and a vessel. The diameter of the turbine is 52 mm. The diameter of the vessel is 60 mm. The dimension of both the turbine and the vessel ensures the non-contact between the two components, and the resulting horizontal gap thickness between the turbine and vessel is 4 mm. In this study, the vessel volume is 80 mL. Before operation, the overflow vessel and the turbine are consecutively tightened to the shaft with hex nuts. Then, the vessel was clamped to the overflow vessel before operation, in order to avoid splash.

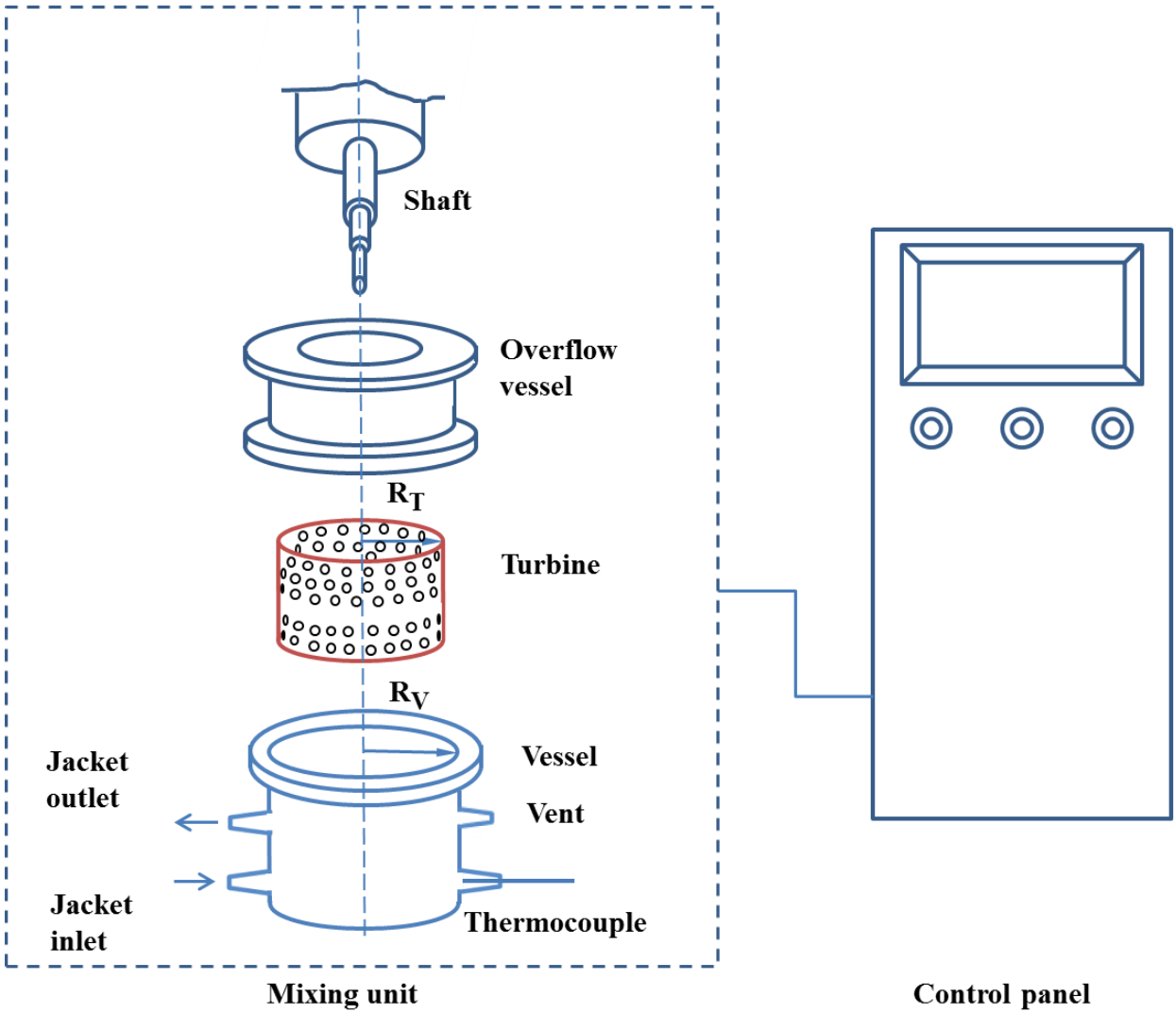

Figure 2.1 Schematic illustration of the modified Taylor-Couette reactor (nanomixer).

The mixing unit was connected to a control panel for a shear rate control and a temperature measurement. The shear rate can be controlled in the range from 2500 s^{-1} (~60 Hz) to 12500 s^{-1} (~300 Hz). The shear rate was defined as the peripheral rotating speed divided by the horizontal gap thickness between the turbine and the vessel [33]. Thus, a 10 m s^{-1} (~60 Hz) peripheral rotating speed is equivalent to a shear rate of 2500 s^{-1}. Water flow can be introduced through the jacket inlet and outlet, for cooling or heating purposes. The orientation of the vent is

deliberately designed to be reverse to the rotating direction of the turbine, to avoid splash during operation. A more detailed description of the nanomixer can be found in our previous work [34].

2.2.3 Nanoshear hybrid alkaline pretreatment

First, 2 g of stored CS was added into the vessel, with 50 mL DI water or NaOH solution at different concentrations. After the nanomixer vessel was tightly clamped to the overflow vessel, a 2-minute retention time was selected, with its maximum shear rate 12500 s^{-1}. No external removal or addition of heat to the system was provided. The vent on the vessel kept the chamber pressure at ambient pressure all the time during the pretreatment. The vessel temperature could reach up to 100 °C under ambient pressure. After the high shear spinning was completed, cooling water was introduced until the system temperature was brought down to 25 °C. The pretreated samples were collected and then taken to the washing step.

2.2.4 Washing

The washing step was necessary after the pretreatment to remove the soluble components and to adjust the pH. In each washing cycle, pretreated CS was diluted with DI water using 1 L beaker, after 10~15 min quiescence, the supernatant was vacuum filtered with a Kontes Ultra-Ware 47 mm microfiltration assembly (Thermo Fisher Scientific Inc., MA, US). Depending on the NaOH concentration, after 5~7 cycles the pH of homogenized suspension could reach ~7. It required more cycles for higher concentration of NaOH used.

2.2.5 Drying

In order to determine the mass of pretreated solid, the washed samples were air-dried prior to the next step. It should be noted that the drying before saccharification might have an impact on the maximum conversions achieved, due to cell wall collapse [35, 36]. The effect is still less severe as compared with the oven-drying process. However, the moisture content test was conducted and calculated on an oven-dried basis, as per Laboratory Analytical Procedure (LAP) 001 provided by National Renewable Energy Laboratory (NREL) [37].

2.2.6 Compositional analysis

The compositional analysis was then performed to determine the cellulose, hemicellulose, and lignin contents of the remaining solid in pretreated or untreated CS. The experiment was conducted according to NREL LAP 002 [38].

2.2.7 Enzymatic hydrolysis

The pretreated samples were enzymatically hydrolyzed using ACCELLERASE^{TM} 1000 (Danisco US Inc. Genencor Div., NY, US). Pretreated CS was immersed in pH 4.8 citrate buffer solution, then incubated in a water bath shaker (New Brunswick Scientific Co. Inc., NJ, US) at 2.5 Hz, 50 $^{\circ}$C up to 168 h. The procedure and calculation were performed as per NREL LAP 013 [36]. At least triplicate tests were performed to produce one data point. The glucose and xylose concentration were tested using high performance liquid chromatography (HPLC, Agilent Technologies Inc., CA, US) with a Bio-Rad ameinex HPX-87H HPLC column (Bio-Rad Laboratories, CA, US).

2.2.8 Scanning electron microscope (SEM) imaging

The dried pretreated samples were gold coated (EMSCOPE SC500 Sputter coater, Ashford, Kent, UK) for 3.5 minutes. In order to prevent structural collapse caused by surface tension force, higher magnification images were critical-point-dried (Blazers CPD 010 Critical point dryer, Bal Tec AG, Furstentum, Lichtenstein) prior to gold coating. All SEM images were taken using JEOL 6400V (Japan Electron Optics Laboratories, JP) with a LaB6 emitter.

2.3 Results and discussions

2.3.1 Compositional analysis

Figure 2.2 shows the compositional fractions of the remaining solid in the NSHA pretreated CS samples. As the concentration of NaOH increased, a higher cellulose content but lower lignin and hemicellulose contents were obtained. Up to 82 % cellulose content in the remaining solid of the NSHA pretreated CS was achieved. The removal of lignin and hemicellulose significantly enhanced the exposure of cellulose fibers to the environment. However, no further increase of cellulose content was observed, showing a plateau at the NaOH concentration of 80 g L^{-1}. In this work, no removal of lignin or hemicellulose by the single nano-shearing force (i.e., 0 g L^{-1} NaOH conc.) was found. Also, the fractional changes were not significant at the low concentration of NaOH (4 g L^{-1}).

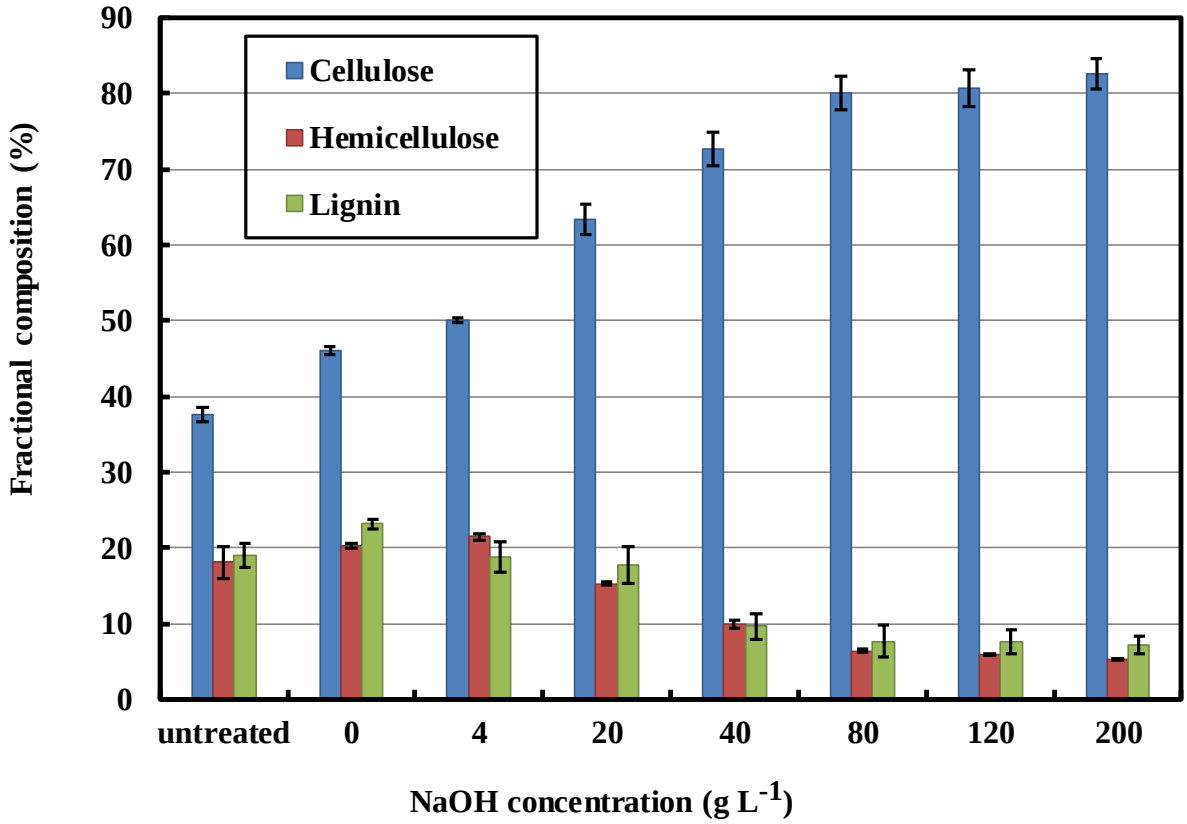

Figure 2.2 Major fractions of the remaining solid of CS before and after pretreatment at different conditions.

Note:

a. All samples were pretreated with a shear rate of 12500 s^{-1} and a retention time of 2 min.

b. NaOH concentrations were represented in g L^{-1}, 0 g L^{-1} NaOH represents water.

c. Values of lignin content included acid soluble lignin and acid insoluble residue.

Table 2.1 Major fractions[a] of the pretreated corn stover after pretreatment methods [8, 39].

Condition	Cellulose content (%)	Hemicellulose content (%)	Lignin content (%)
NSHA[b]	72.7	9.9	9.7
AFEX[c]	34.4	22.8	18.0
ARP[d]	61.9	17.9	8.8
Controlled pH[e]	52.7	16.2	25.2
Dilute acid[f]	64.4	2.9	26.4
Lime[g]	56.7	26.4	14.6
SO_2[h]	56.9	11.6	23.8
NH_4OH/HCl[i]	65.7	12.9	21.0
NaOH[j]	64.1	24.6	8.6

[a] Results are calculated on an oven-dried basis.

[b] Referred to as nanoshear hybrid alkaline pretreatment, 1:1 NaOH to biomass, room temperature nanoshear at a shear rate of 12500 s^{-1} for 2 min.

[c] Known as ammonia fiber explosion, 1:1 NH_3 to biomass, 90 °C, 1.5 $\times 10^6$ Pa for 5 min.

[d] Known as ammonia recycle percolation, 1:3 NH_3 to biomass, 170 °C, 2.2 $\times 10^6$ Pa for 20 min.

[e] 190 °C for 15 min.

[f] 1:20 H_2SO_4 to biomass, 160 °C for 20 min.

[g] 1:2 $Ca(OH)_2$ to biomass, 55 °C for 4 weeks.

[h] 3 % SO_2, 190 °C for 5 min.

[i] 10 % NH_4OH, 26 °C for 24 h, then 0.3 mol L^{-1} HCl, 100-108 °C for 1 h.

[j] 2 % NaOH, 120 °C for 30 min.

In Table 2.1, for comparison, the compositional fractions of the remaining solid in the pretreated CS by NSHA and other well-known pretreatment methods are listed. With 40 g L^{-1} NaOH (i.e. 1:1 NaOH to biomass), the NSHA pretreated CS has 72.7 % of cellulose content, 9.9 % of hemicellulose content and 9.7 % of lignin content in the remaining solid. Compared with other pretreatment methods, the cellulose content in the present study is significant and unique. The lignin left in the pretreated solid was low. This result is similar to the effect of most other alkali-based pretreatment methods. On the other hand, the hemicellulose content in the NSHA pretreated CS was found to be lower unlike other conventional alkali pretreatment methods. While most pretreatment methods had the retention time from 5 minutes (AFEX) to several weeks (Lime), the NSHA pretreatment method greatly shortened the retention time to only 2 minutes, but still showed a higher pretreatment efficiency (the highest cellulose content in the remaining solid) compared with other conventional methods. The high fraction of cellulose content implies two major potential applications of the NSHA pretreatment. First, this technology can be utilized to pretreat biomass for biofuel production. Second, the NSHA with higher NaOH concentration (above 80 g L^{-1}) can also be applied to pulping or related industry utilizing lignocellulosic biowastes.

2.3.2 Chemical and energy recovery

The remaining liquor after the 2-minute NSHA pretreatment was similar to the black liquor in pulping industry, which contained inorganic chemicals (mainly sodium hydroxide) and combustible compounds. The chemical and energy recovery processes such as the conventional Kraft recovery boiler [40] and the more recent black liquor gasification [41] have been well-

developed. Hence, there is a great potential to integrate an appropriate sodium hydroxide and/or energy recovery processes into our system.

2.3.3 Enzymatic hydrolysis

All existing and studied pretreatment methods, as listed in Table 2.1, primarily aim to disrupt the naturally formed resistance that protects plant from biological and chemical attacks, and therefore to enhance the accessibility of enzymes to cellulose and hemicellulose. In other words, in ethanol production, the reason to apply pretreatment is to reduce either the amount of the expensive enzymes or the required time during saccharification while achieving a fast and high conversion of pretreated biomass to monomeric sugars (glucose and xylose). Therefore, enzymatic hydrolysis of different batches of pretreated biomass at a certain enzyme loading and saccharification time was carried out in this study.

Figures 2.3-2.5 report the results of enzymatic conversion of CS after the 2-minute NSHA pretreatment. As the curves indicate, kinetics varied with enzyme loadings and pretreatment conditions. The Filter paper unit (FPU) was applied to describe the cellulase activity. FPU was defined as the activity to achieve 2 mg of glucose from 50 mg of filter paper in 1 h [42]. At an enzyme loading of 5 FPU (g cellulose)$^{-1}$, the cellulose in the pretreated CS with NSHA process at the NaOH concentration of 40 g L^{-1} was completely converted to glucose after a 7 days hydrolysis. The completion point shifted to an earlier time when a higher enzyme loading was applied. The complete cellulose conversion took 3 days at an enzyme loading of 20 FPU (g cellulose)$^{-1}$ and 1 day at that of 60 FPU (g cellulose)$^{-1}$. And it was noticed that the cellulose conversion was 92 % already in 1 day at the enzyme loading of 20 FPU (g cellulose)$^{-1}$.

A similar trend was found for hemicellulose. After pretreated under the NaOH concentration of 40 g L^{-1}, the hemicellulose in the NSHA pretreated CS was completely converted to xylose in 3 days, at the enzyme loading of 60 FPU (g cellulose)$^{-1}$. However, when the pretreatment was carried out under the NaOH concentration of 4 g L^{-1}, the hemicellulose conversion in the NSHA pretreated CS only reached 91 % in 7 days at the enzyme loading of 60 FPU (g cellulose)$^{-1}$.

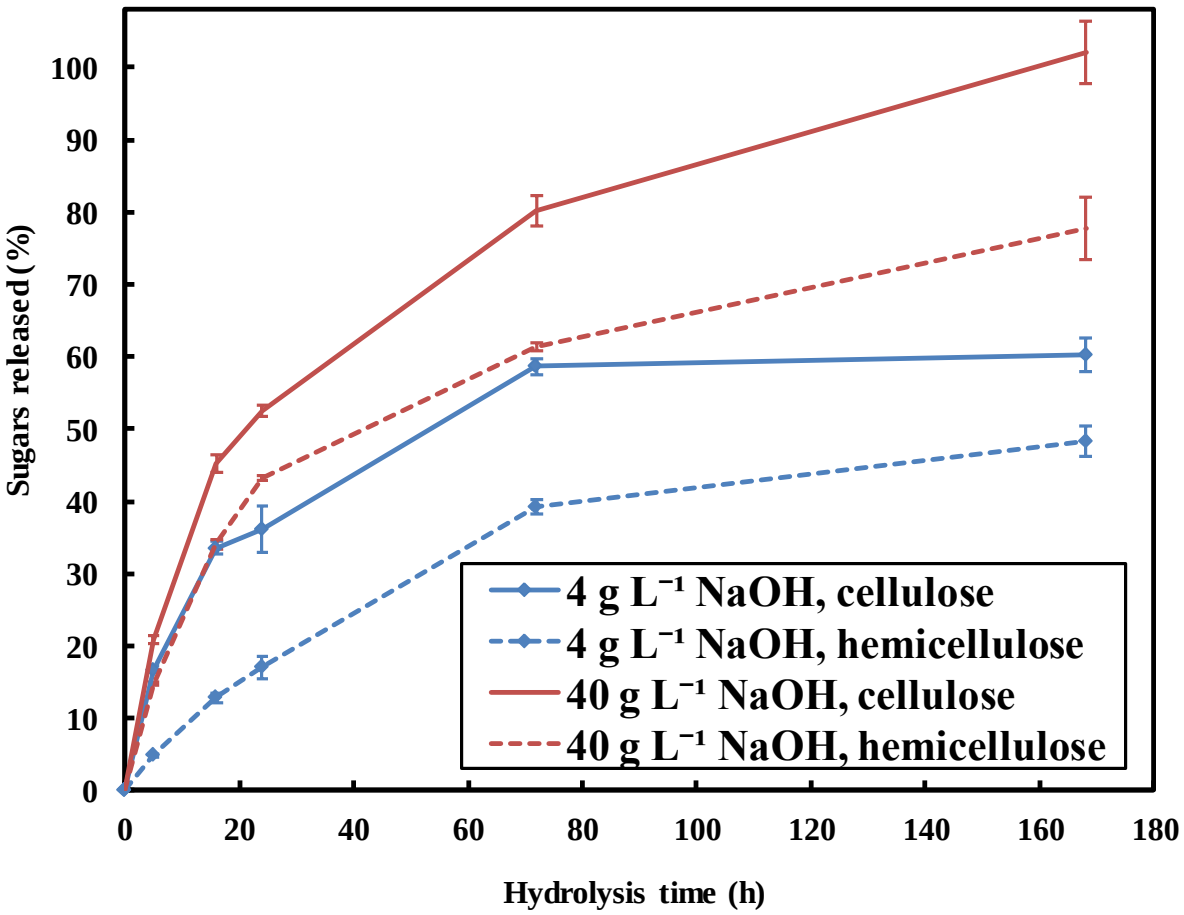

Figure 2.3 Cellulose and hemicellulose conversion profile of the NSHA pretreated CS with 4 g L^{-1} and 40 g L^{-1} NaOH, with a 5 FPU (g cellulose)$^{-1}$ enzyme loading, and a 50 °C incubation temperature.

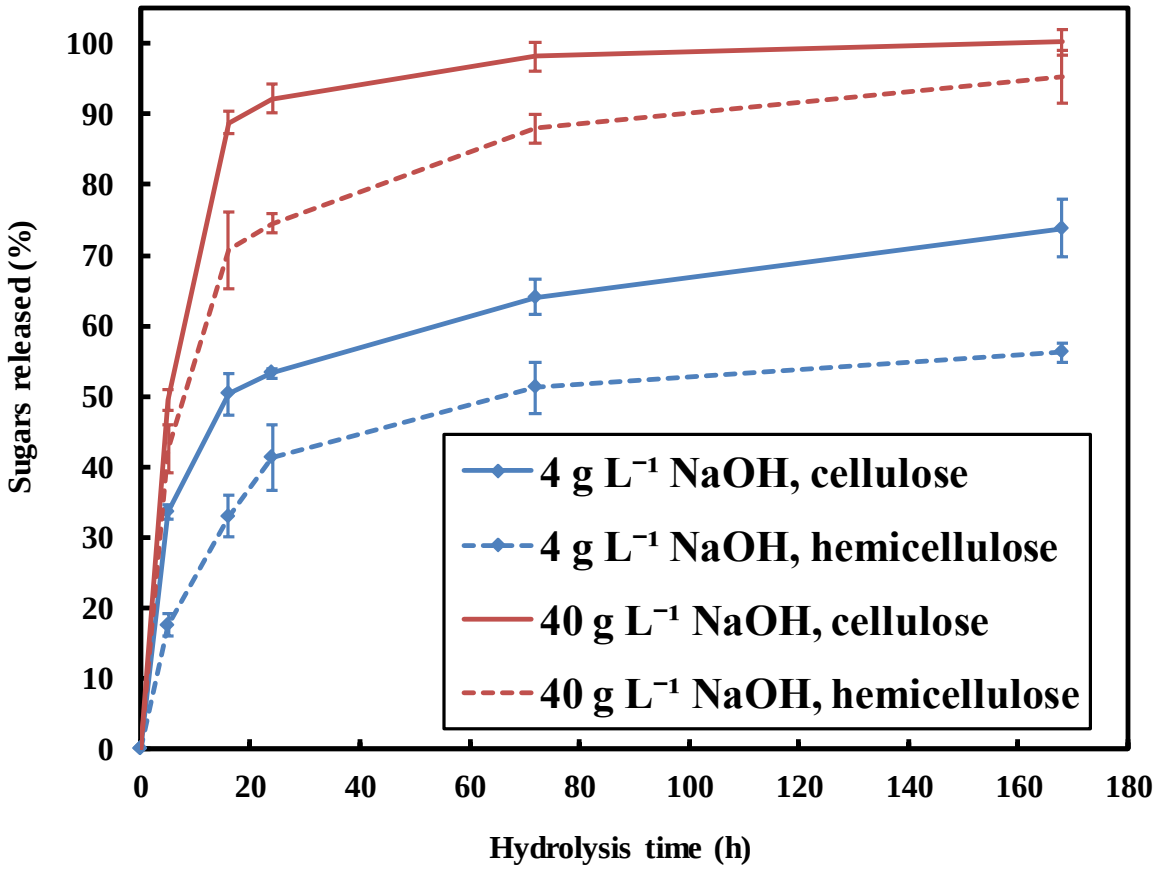

Figure 2.4 Cellulose and hemicellulose conversion profile of the NSHA pretreated CS with 4 g L^{-1} and 40 g L^{-1} NaOH, with a 20 FPU (g cellulose)$^{-1}$ enzyme loading, and a 50 °C incubation temperature.

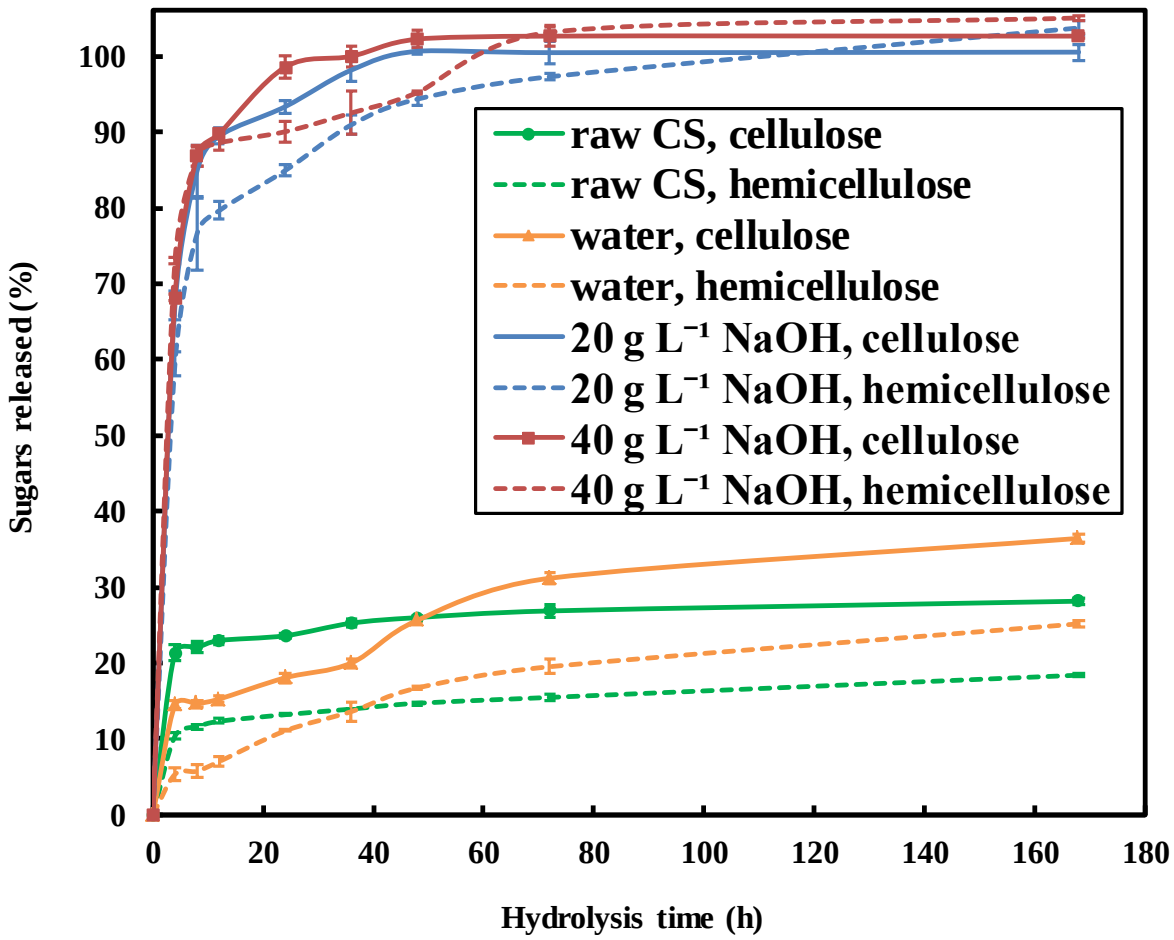

Figure 2.5 Cellulose and hemicellulose conversion profile of the NSHA pretreated CS, with a 60 FPU (g cellulose)$^{-1}$ enzyme loading, and a 50 °C incubation temperature.

As shown in Figure 2.5, when the NSHA pretreatment was applied at the NaOH concentration of 40 g L^{-1} (1:1 NaOH to biomass), the cellulose conversion was nearly 100 % in 1 day. The conversion of cellulose in the untreated CS was 28 % after 7 days saccharification. Meanwhile, the hemicellulose conversion was approximately 100 % after 3 days, whereas the conversion of hemicellulose in the untreated CS was only 19 % after 7 days saccharification. A 4-fold increase in the cellulose conversion and a 5-fold increase in the hemicellulose conversion were exhibited. When the NaOH concentration was decreased to 20 g L^{-1} (1:2 NaOH to

biomass), the conversions of both components were still remarkable. The cellulose conversion was 93 % in 1 day and almost 100 % after 36 h, and the hemicellulose conversion was 97 % after 3 days. The NSHA pretreatment without any usage of alkali was not sufficient to obtain a good enzymatic digestibility.

The high efficiency of the NSHA pretreatment on lignocellulosic biomass came from the smart and synergistic combination of many positive effects. The mechanical nano-scale shearing generated by the turbine would cause the twist of corn stover in the perpendicular axis to the fiber and the degradation of the nano-structured cell wall complex along with the NaOH chemical effect and generate a thermal effect simultaneously due to the severe friction between the turbine and heterogeneous biomass/solvent. All those thermochemical and mechanical effects are reported to be beneficial for the improvement of enzyme digestibility [8]. However, the single application of shearing force for a few minutes was found to be insufficient to make the biomass accessible to enzymes, similarly as the application of single alkali chemical force in such a short time. The natural shield of biomass formed by hemicelluloses and lignin aiming to protect plants from biological attacks still existed. When alkali such as NaOH was synergistically combined into the nano-shearing force, the hybrid pretreatment effect was taking place. Sodium hydroxide is one of the major chemicals that are used to delignify biomass and to solubilize hemicelluloses [12, 39]. But it is reported that the reaction itself takes long (30 minutes to several hours), and may be longer when heat-up is required to reach high temperature and/or high pressure [43, 44]. With the synergistic smart use of high shearing force under alkaline conditions, the efficiency of lignin removal was greatly enhanced resulting in the significant decrease of the reaction time to just a couple of minutes. The reason was that because of high shear rate of the turbine, the diffusion boundary layer between the solid-liquid interphase was

remarkably getting thinner so that NaOH (i.e., OH^-) could interact with biomass cell wall easily in a very short time. Meanwhile, the micro- and nanoscale cavitation generated by the nano-mixer, combined with high shear force, tended to cause the fibrillation of cell walls [45-48], that is, structural disruption both perpendicular to the fiber axis and longitudinally along the fiber axis. Temperature rising up to 100 °C in the vessel also helped increase the delignification reaction rate simultaneously.

The proposed mechanism indicates positive aspects to incorporate the high shear to the existing pretreatment methodologies and with many other chemicals, due to the synergistic effects aroused by the high shear rate. Other than the NaOH that is applied in this work, many other non-volatile chemical compounds, including potassium hydroxide, sulfuric acid, hydrogen peroxide and ionic liquids can be incorporated with the high shear to enable a fast and efficient pretreatment. However, for pretreatment with volatile chemical compounds (e.g. organic solvents, ammonia, ozone, etc.), the reactor is usually sealed (otherwise the chemicals will be vaporized and exhausted). Thus the high shear will cause an increasing temperature and pressure at the same time, leading to a reactor run-away. The safety concerns are relatively lessened when a short retention time (e.g. a few minutes or less) is selected. Without a temperature control, calcium hydroxide, which has a decreasing solubility with increasing temperature [9, 10], is not recommended to be incorporated with the high shear rate. Because the rising temperature caused by the high shear will result in an even more heterogeneous solid-solid phases system, and therefore greatly weaken the synergistic effects.

2.3.4 Scanning electron microscope (SEM) imaging

To further investigate the micro- and nano-scopic mechanism of the NSHA pretreatment, SEM images of the untreated and NSHA pretreated CS samples were reported in Figures 2.6 and 2.7. Gradual changes of the microscopic structures as a function of NaOH concentration, revealed in Figure 2.6, indicated that the NSHA pretreatment could efficiently disintegrate cellulose microfibril aggregates, and open up mini-pores on the surface in such a short time (i.e., 2 minutes). The biomass cell walls were significantly disrupted when the NSHA pretreatment was applied even at a moderate NaOH concentration.

As discussed in the previous section, the high shear rate helped significantly reduce the diffusion boundary layers between solid-liquid phases so that well permeated NaOH (OH^-) significantly enhanced lignin removal in a very short time. And thus, the high shearing force could further extend its impact on the cellulose structure, as shown in Figure 2.7, in which tassel-like fibrils represent the cellulose nano-fibril aggregates. Apparently the exposed fibrils increased the cellulose surface area and benefited for the enzyme accessibility. Meanwhile, with the same retention time and shear rate, no such fibrils were found in the solid pretreated by the high shear without using alkali, as shown in Figure 2.6(b).

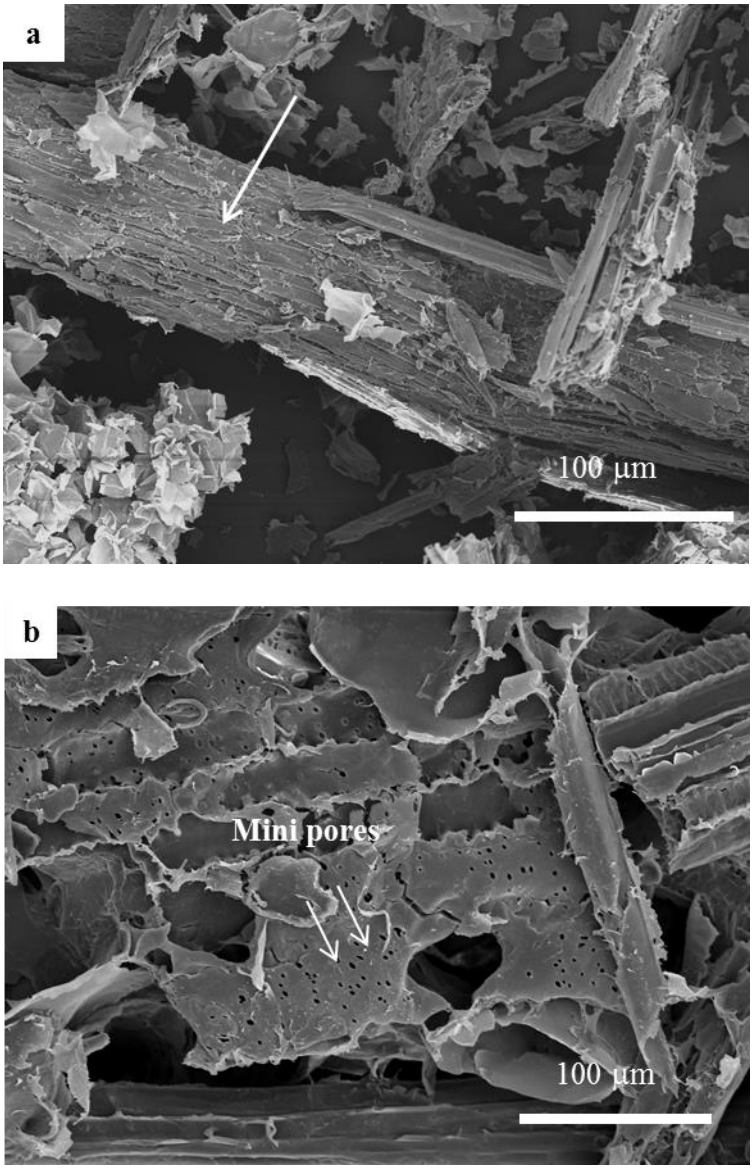

Figure 2.6 From crystalline to disrupted structure – before and after pretreatment at different conditions. a) Untreated corn stover, area pointed by the arrow is an intact cell wall; b) nanoshear hybrid water pretreated CS; c) 4 g L^{-1} NaOH NSHA pretreated CS, area pointed by the arrow is a discontinued structure with a reduced fiber length (fibrillation); d) 20 g L^{-1} NaOH NSHA pretreated CS, area indicated by the circle is where cellulose crystalline structure breaks apart (another form of fibrillation); e) 40 g L^{-1} NaOH NSHA pretreated CS, minipores and more disrupted fibers.

Figure 2.6 (cont'd)

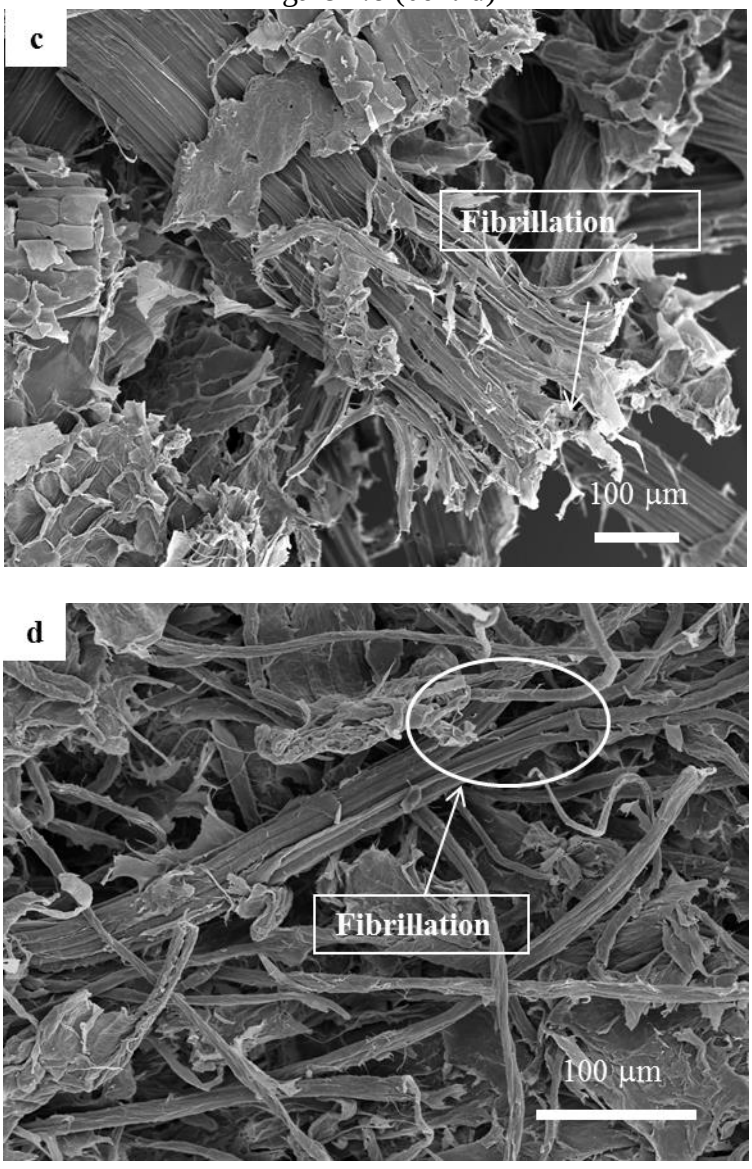

Figure 2.6 (cont'd)

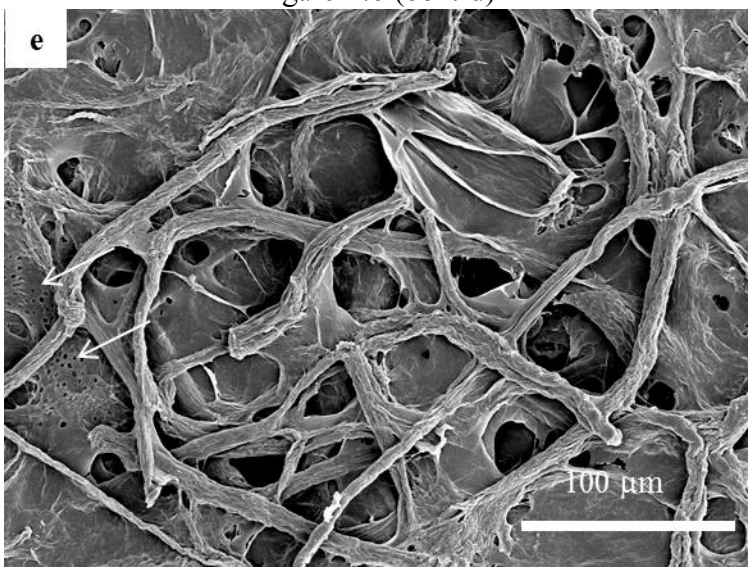

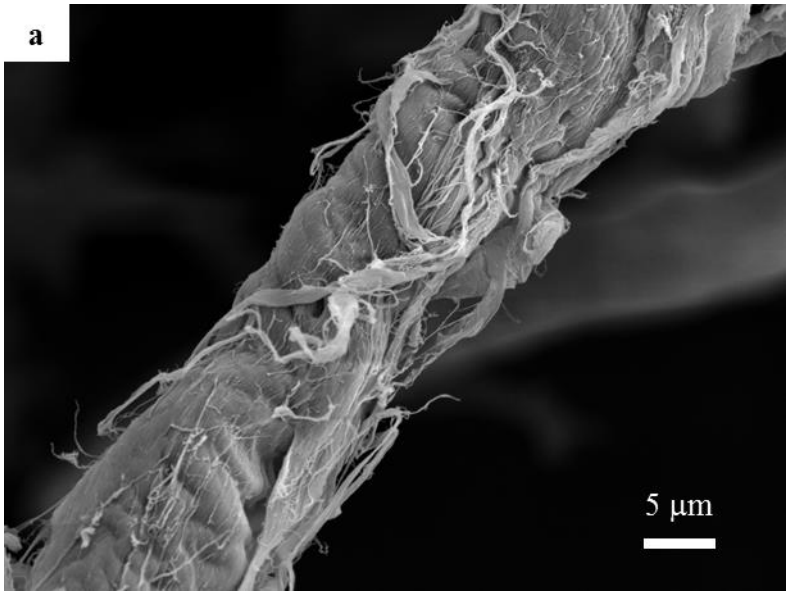

Figure 2.7 Fibril aggregates on the surface of the cellulose crystalline structure. a) 40 g L^{-1} NaOH NSHA pretreated CS, nano-fibril aggregates retained on the surface of a single cellulose fiber, diameters are around 300-500 nanometers; b) 40 g L^{-1} NaOH NSHA pretreated CS, more fibril aggregates with thinner diameters.

Figure 2.7 (cont'd)

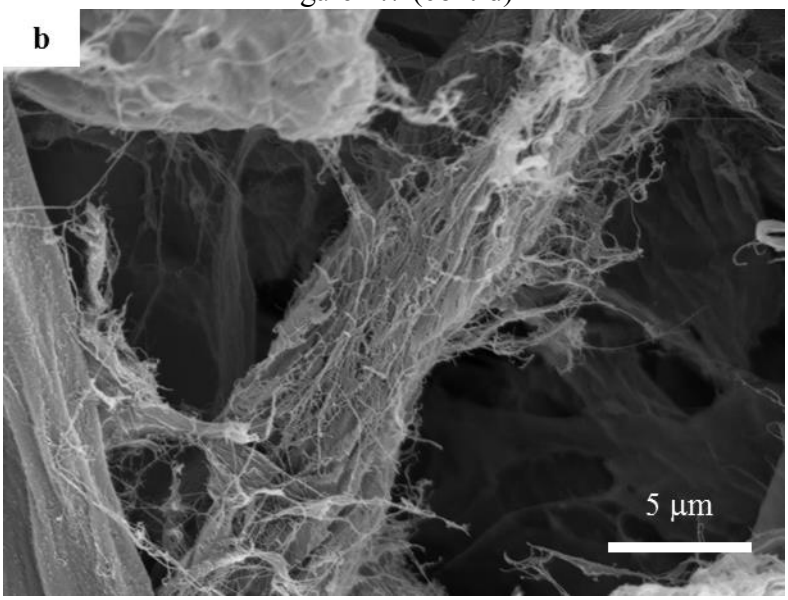

2.4 Conclusions

A novel and fast nano-scale hybrid pretreatment named nanoshear hybrid alkaline pretreatment method was introduced in this work. The macro-scale study (e.g., enzymatic hydrolysis) demonstrated a great enhancement in digestibility of CS with the NSHA pretreatment. The saccharification rate and overall conversion of cellulose and hemicellulose were greatly improved over the untreated CS sample. At the same time, a near-theoretical maximum enzymatic conversion of the NSHA pretreated sample was achieved in one day. The NSHA pretreatment was proved to facilitate a significant lignin and hemicellulose removal and a disruption of cellulose nanostructure. All these merits could contribute to a better digestibility of CS, in terms of reduced enzyme loading and saccharification time. Moreover, considering that in the performed enzymatic hydrolysis no optimization of enzyme cocktail was conducted, a further enhancement of saccharification rate and reduced enzyme loading could be expected.

In addition, the enhancement of digestibility was explored and explained by micro-scale study (e.g., SEM imaging), in terms of inherent microstructural changes of the remaining solid in

the pretreated biomass. According to the SEM images, the NSHA pretreatment was found to help greatly disrupt the biomass cell walls, and also disintegrate cellulose microfibril aggregates in a fast and efficient way. There are still great potentials for further improvement and optimization on this newly-introduced method, and extended research on this topic is under investigation.

REFERENCES

REFERENCES

1. Sanchez OJ, Cardona CA. Trends in biotechnological production of fuel ethanol from different feedstocks. Bioresource Technology 2008;99(13): 5270-5295.

2. Börjesson P. Good or bad bioethanol from a greenhouse gas perspective - what determines this? Applied Energy 2009;86(5): 589-594.

3. Lave L, MacLean H, Hendrickson C, Lankey R. Life-cycle analysis of alternative automobile fuel/propulsion technologies. Environmental Science & Technology 2000;34(17): 3598-3605.

4. Wooley R, Ruth M, Glassner D, Sheehan J. Bioprocess engineering and biobased industrial products process design and costing of bioethanol technology: a tool for determining the status and direction of research and development. Biotechnology Progress 1999;15(5): 794-803.

5. Wyman CE, Dale BE, Elander RT, Holtzapple M, Ladisch MR, Lee YY. Coordinated development of leading biomass pretreatment technologies. Bioresource Technology 2005;96(18): 1959-1966.

6. Mosier N, Wyman C, Dale B, Elander R, Lee YY, Holtzapple M, et al. Features of promising technologies for pretreatment of lignocellulosic biomass. Bioresource Technology 2005;96(6): 673-686.

7. Hendriks ATWM, Zeeman G. Pretreatments to enhance the digestibility of lignocellulosic biomass. Bioresource Technology 2009;100(1): 10-18.

8. Kumar R, Mago G, Balan V, Wyman CE. Physical and chemical characterizations of corn stover and poplar solids resulting from leading pretreatment technologies. Bioresource Technology 2009;100(17): 3948-3962.

9. Kaar WE, Holtzapple MT. Using lime pretreatment to facilitate the enzymic hydrolysis of corn stover. Biomass and Bioenergy 2000;18(3): 189-199.

10. Kim S, Holtzapple MT. Lime pretreatment and enzymatic hydrolysis of corn stover. Bioresource Technology 2005;96(18): 1994-2006.

11. Kim TH, Lee YY. Pretreatment and fractionation of corn stover by ammonia recycle percolation process. Bioresource Technology 2005;96(18): 2007-2013.

12. Li Y, Ruan R, Chen PL, Liu Z, Pan X, Lin X, et al. Enzymatic hydrolysis of corn stover pretreated by combined dilute alkaline treatment and homogenization. Transactions of the ASAE 2004;47(3): 821-825.

13. Lloyd TA, Wyman CE. Combined sugar yields for dilute sulfuric acid pretreatment of corn stover followed by enzymatic hydrolysis of the remaining solids. Bioresource Technology 2005;96(18): 1967-1977.

14. Teymouri F, Laureano-Perez L, Alizadeh H, Dale BE. Optimazation of the ammonia fiber explosion (AFEX) treatment parameters for enzymatic hydrolysis of corn stover. Bioresource Technology 2005;96(18): 2014-2018.

15. Vidal PF, Molinier J. Ozonolysis of lignin - improvement of in vitrodigestibility of poplarsawdust. Biomass 1988;16(1): 1-17.

16. Gould JM. Alkaline peroxide delignification of agricultural residues to enhance enzymatic saccharification. Biotechnology and Bioengineering 2004;26(1): 46-52.

17. Neely WC. Factors affecting the pretreatment of biomass with gaseous ozone. Biotechnology and Bioengineering 2004;26(1): 59-65.

18. Chum HL, Johnson DK, Black S, Baker J, Grohmann K, Sarkanen KV, et al. Organosolv pretreatment for enzymatic hydrolysis of poplars: I. Enzyme hydrolysis of cellulosic residues. Biotechnology and Bioengineering 2004;31(7): 643-649.

19. Pan X, Arato C, Gilkes N, Gregg D, Mabee W, Pye K, et al. Biorefining of softwoods using ethanol organosolv pulping: Preliminary evaluation of process streams for manufacture of fuel-grade ethanol and co-products. Biotechnology and Bioengineering 2005;90(4): 473-481.

20. Dadi AP, Varanasi S, Schall CA. Enhancement of cellulose saccharification kinetics using an ionic liquid pretreatment step. Biotechnology and Bioengineering 2006;95(5): 904-910.

21. Lee SH, Doherty TV, Linhardt RJ, Dordick JS. Ionic liquid-mediated selective extraction of lignin from wood leading to enhanced enzymatic cellulose hydrolysis. Biotechnology and Bioengineering 2009;102(5): 1368-1376.

22. Avellar BK, Glasser WG. Steam-assisted biomass fractionation. I. process considerations and economic evaluation. Biomass and Bioenergy 1998;14(3): 205-218.

23. Glasser WG, Wright RS. Steam-assisted biomass fractionation. II. fractionation behavior of various biomass resources. Biomass and Bioenergy 1998;14(3): 219-235.

24. Liu C, Wyman CE. Patial flow of compressed-hot water through corn stover to enhance hemicellulose sugar recovery and enzymatic digestibility of cellulose. Bioresource Technology 2005;96(18): 1978-1985.

25. Millett MA, Effland MJ, Caulfield DF. Influence of fine grinding on the hydrolysis of cellulosic materials - acid vs. enzymatic. In: Brown RD, Jurasek L, editors. Hydrolysis of Cellulose: Mechanisms of Enzymatic and Acid Catalysis. Washington DC: American Chemical Society; 1979:71-89 (Advances in Chemistry Series; vol 181).

26. Rivers DB, Emert GH. Lignocellulose pretreatment: a comparison of wet and dry ball attrition. Biotechnology Letters 1987;9(5): 365-368.

27. Paakko M, Ankerfors M, Kosonen H, Nykanen A, Ahola S, Osterberg M, et al. Enzymatic hydrolysis combined with mechanical shearing and high-pressure homogenization for nanoscale cellulose fibrils and strong gels. Biomacromolecules 2007;8(6): 1934-1941.

28. Liu C, Wyman CE. The effect of flow rate of compressed hot water on xylan, lignin, and total mass removal from corn stover. Industrial & Engineering Chemistry Research 2003;42(21): 5409-5416.

29. Senturk-Ozer S, Gevgilili H, Kalyon DM. Biomass pretreatment strategies via control of rheological behavior of biomass suspensions and reactive twin screw extrusion processing. Bioresource Technology 2011;102(19): 9068-9075.

30. Lee S-H, Teramoto Y, Endo T. Enzymatic saccharification of woody biomass micro/nanofibrillated by continuous extrusion process I – Effect of additives with cellulose affinity. Bioresource Technology 2009;100(1): 275-279.

31. Lee S-H, Teramoto Y, Endo T. Enhancement of enzymatic accessibility by fibrillation of woody biomass using batch-type kneader with twin-screw elements. Bioresource Technology 2010;101(2): 769-774.

32. Asa T, inventor; Tokushu Kika Kogyo Kabushiki Kaisha, assignee. Method of, and appararus for, agitating treatment liquid. United States patent US 5582484. 1996 Dec 10.

33. Mezger TG. The Reology Handbook. 2nd ed. Hannover, Germany: Vincentz; 2006.

34. Lee I, Wang W, Ji S, inventors; Board of Trustees of Michigan State University, assignee. Device and method for pretreatment of biomass. United States patent US 20120036765. 2012 Feb 16.

35. Viamajala S, McMillan JD, Schell DJ, Elander RT. Rheology of corn stover slurries at high solids concentrations - effects of saccharification and particle size. Bioresource Technology 2008;100(2): 925-934.

36. Selig M, Weiss N, Ji Y. Enzymatic Saccharification of Lignocellulosic Biomass. Golden, Colorado: National Renewable Energy Laboratory; 2008,March, 7p.

37. Sluiter A, Hames B, Hyman D, Payne C, Ruiz R, Scarlata C, et al. Determination of Total Solids in Biomass and Total Dissolved Solids in Liquid Process Samples. Golden, Colorado: National Renewable Energy Laboratory; 2008,March, 8p.

38. Sluiter A, Hames B, Ruiz R, Scarlata C, Sluiter J, Templeton D, et al. Determination of Structural Carbohydrates and Lignin in Biomass. Golden, Colorado: National Renewable Energy Laboratory; 2008,April, 17p.

39. Chen M, Zhao J, Xia L. Comparison of four different chemical pretreatments of corn stover for enhancing enzymatic digestibility. Biomass and Bioenergy 2009;33(10): 1381-1385.

40. Adams TN, Frederick WJ. Kraft recovery boiler physical and chemical processes. New York: The American Paper Institute, Inc.; 1988.

41. Kohl AL. Black liquor gasification. The Canadian Journal of Chemical Engineering 1986;64(2): 299-304.

42. Adney B, Baker J. Measurement of Cellulase Activities. Golden, Colorado: National Renewable Energy Laboratory; 2008,January, 10p.

43. He X, Miao Y, Jiang X, Xu Z, Ouyang P. Enhancing the enzymatic hydrolysis of corn stover by an integrated wet-milling and alkali pretreatment. Applied Biochemistry and Biotechnology 2010;160(8): 2449-2457.

44. Montane D, Farriol X, Salvado J, Jollez P, Chornet E. Fractionation of wheat straw by steam-explosion pretreatment and alkali delignification. cellulose pulp and byproducts from hemicellulose and lignin. Journal of Wood Chemistry and Technology 1998;18(2): 171-191.

45. Thorre DV, inventor; Process for obtaining bio-functional fractions from biomass. United States patent US 20050095331. 2004 Jul 15.

46. Stuart ED, Tex B, inventors; Colorado State University Research Foundation, assignee. Treatment of fibrous lignocellulosic biomass by high shear forces in a turbulent couette flow to make the biomass more susceptible to hydrolysis. United States patent US 5370999. 1994 Dec 6.

47. Bouchard J, Nguyen TS, Chornet E, Overend RP. Analytical methodology for biomass pretreatment - part 1: solid residues. Biomass 1990;23(4): 243-261.

48. Bouchard J, Nguyen TS, Chornet E, Overend RP. Analytical methodology for biomass pretreatment. part 2: characterization of the filtrates and cumulative product distribution as a function of treatment severity. Bioresource Technology 1991;36(2): 121-131.

Chapter 3 Nano-deposition on 3-D open-cell aluminum foam materials for improved energy absorption capacity

3.0 Abstract

Open cell aluminum (Al) foams have been used as energy absorbers for decades. Their energy absorption capacity can be enhanced by thickening the foam struts, or increasing the foam's relative density. However, the enhancement is compromised by the inherent characteristics of its stress-strain property relationship, whereby upon homogeneous strut thickening, an increase in the plateau stress without a reduction in densification strain cannot be achieved. In this chapter, to overcome this inherent barrier, nano-crystalline copper (Cu) was deposited onto the Al foam and novel 3-D Cu/Al, heterogeneously thickened, composite foam structured materials were fabricated and tested for the first time. A non-cyanide nano-crystalline copper electro-deposition system was setup for the coating of open-cell Al foam, and, the energy absorption capacity as a function of foam pore size and Cu coating thickness was investigated. A variety of characterization methods confirmed the nano-crystalline structure of the Cu deposition (38 nm). The energy absorption capacity of Al foams (with average strut thickness of 192 μm) reinforced with a 60 μm Cu coating was 3 times greater than that of plain foams. The compressive stress-strain response of the composite samples showed no significant reduction of the densification strain compared to the uncoated foams due to the small change in the foam strut thickness and pore size. A comparison between thin Cu-coated and uncoated Al foam samples with the same overall strut thickness (i.e., same effective volume density and porosity) showed that the nano-reinforced foams had superior energy absorption capacity over plain foams with the same overall thickness, (~2 times greater).

3.1 Introduction

Metallic foams are cellular metals with pores integrated in their structure [1]. The pores can be closed-cell in which the solid metal forms the face of the cells, or open-cell in which the solid metal forms the edge of the cells [2, 3]. The fabrication of metallic foams was first reported in the 1920s in France [4]. The first reference of the fabrication of metallic foams in the United States was reported in the 1940s [5, 6]. Since then, the techniques for the preparation of metallic foams have been developed and advanced. Metallic foams have been commercially used in many sectors, and different materials have been utilized for various applications. Metals used in foams include aluminum and its alloys (most common), copper, zinc, bronze, iron, nickel, titanium and gold [1].

Metallic foams with different morphologies can be manufactured in various ways [2, 3, 7-10]. The different methods can be classified based on the state in which the metal is initially processed [9]: metal vapor, liquid metal, powdered metal, and metal ions. Among those processes, one of the typical methodologies is to produce foams from the liquid metal, where the molten metal is mixed with a thickening agent (e.g., CaO) above the melting point of the metal. A blowing agent (e.g.,TiH_2) is added afterwards to facilitate direct foaming of the metal [11, 12]. A cooling step is needed to produce a foamed block of metal. Metallic foams have various applications because of their unique mechanical, thermal, electrical, and acoustic properties. Applications include, but are not limited to, energy absorbers, heat dissipation media, heat exchangers, battery electrodes, silencers, and sound damping devices [2, 8, 9, 13-19].

Metallic foams have been recognized as excellent energy absorbers for decades due to their unique compressive stress-stain behavior and their high stiffness-to-weight ratio [13]. The compressive constitutive response of metal foams is defined by three major stages: the linear

elastic region, the plastic collapse region, and the densification region. Two parameters are important. The plateau stress is the upmost point of the elastic region and represents the highest stress that can be sustained without permanent damage. The densification strain is the deformation after which the stress ramps up sharply as it progressively compacts approaching the behavior of the solid material. Thus, a foam structure with a longer and a higher stress plateau is considered to have better energy absorbing capacity.

Efforts have been made to reinforce foams for improved energy absorption capacity [19] by thickening the struts with the same base material, but success has been limited. The underlying barrier has been that with increased foam strut thickness the plateau stress increases but the densification strain decreases [13, 14, 19]. Thus, by thickening the foam struts with the same material the improvement of the energy absorption capacity might be compromised.

Self-assembled nano-composites or nano-coatings have been introduced to provide materials with multifunctional properties or to reinforce substrates for enhancements not only at the micro-scale but also at the macro-scale level [20-32]. Hybrid nanocrystalline Ni/Al metal foams were fabricated and identified as composite material system with reinforced mechanical properties [33, 34]. The strategy exhibits the potential to obtain coatings with mechanical properties superior to those of conventional materials. With the goal of enhancing the energy absorption capacity of metal foams self-assembled nano-reinforcement could help increase the plateau stress with a reduced effect on the densification strain. Recently, Jung *et al*. [35] reported the use of nano-crystalline nickel (Ni) depositions to reinforce aluminum foam. With a 250 μm Ni coating thickness the plateau stress was considerably increased. However, the thick coating notably reduced the densification strain, which significantly compromised the energy absorption capacity.

To overcome the inherent opposing goals of maximizing plateau stress without significantly affecting the densification strain the coating thickness needs to be limited so that the original foam porosity is not changed significantly. The hypothesis of this study was that a stiffer metal coating would limit the foam strut thickness and porosity changes, consequently limiting the reduction of the densification strain. Copper was used as an illustrative example in this study based on the following rationale. Copper electro-deposition is well established and developed over several decades [10, 36]. Copper fulfills the noted stiffness requirement with a Young's modulus that is almost twice that of aluminum (69 GPa [37]). Meanwhile, although the stiffness of copper (123 GPa [37]) is less than nickel (206 GPa [37]), copper is less expensive than nickel. In the presented study open-cell aluminum foams were reinforced by copper nanocrystalline coating to obtain an enhanced energy absorption capability. Unlike the recently reported work on Ni coated Al foam [35], this paper reports on nano-crystalline Cu coatings for enhanced energy absorption of Al foams, and reports on new 3-D Cu nano-deposition techniques and controls for foam materials. In addition, a systematic experimental characterization that highlights the unique behavior of nano-reinforced open-cell metal foams is presented.

3.2 Experimental Methods

3.2.1 Materials and equipment

The chemicals used for pretreatment of the Al foams were sodium carbonate (Na_2CO_3, $\geq$ 99.0 %), sodium phosphate (Na_3PO_4, 96 %), sodium hydroxide (NaOH, $\geq$ 97.0 %), nitric acid (HNO_3, $\geq$ 90.0 %), and ammonium hydrogen difluoride ($(NH_4)HF_2$, 95 %), all purchased from Sigma-Aldrich (St. Louis, MO).

The Al open-cell foam (ERG Aerospace Co., Oakland, CA) samples were rectangular bars (25.4 mm × 25.4 mm × 50.8 mm). Foams with different pore sizes (10, 20 and 40 pores per inch, PPI) and different relative densities (3.5 (±0.5) %, 6 (±1) %, 12 (±1) %) were acquired. Relative density is the density of the foam divided by the density of the solid parent material. For the same sample volume, higher relative density means thicker struts.

Deionized (DI) water supplied by a Barnstead Nanopure-UV 4 stage purifier (Barnstead International Inc., Dubuque, IA), equipped with a UV source and final 0.2 μm filter with a resistance ≥ 18.0 MΩ·cm was used for aqueous solution preparation and washing.

The electro-deposition setup featured the following components. A potentiostat (Allied Plating Supplied, Inc., Hialeah, FL) with a maximum output of 15 amperes and 12 volts. Non-cyanide copper electrolytes (Uyemura International Co., Ontario, CA), which mainly contained copper pyrophosphate as the copper source. And a Pyrex glass container (World Kitchen LLC, Greencastle, PA) supported by a stirrer/hot plate model 11-300-49 SHP (ThermoFisher Scientific, Barrington, IL) with a stirring speed range of 60 to 1200 rpm and temperature control up to 540 °C.

The anode was niobium mesh plated with platinum (Larry King Co., Rosedale, NY), with dimensions of 140 mm (L) × 55 mm (W) × 65 mm (H). The copper anode (Mcmaster-Carr, Santa Fe Springs, CA) was attached to the mesh.

3.2.2 Sample pretreatment

Pretreatment of the Al foam before electro-deposition is important to ensure proper adhesion of the metals that will be subsequently applied to the base material. Pretreatment is also critical to have the same boundary conditions for different samples. Aluminum foam samples

were pretreated as per ASTM B253-87 [38] in the following order. The sample was degreased in a carbonate-phosphate cleaning solution (25 g/L Na_2CO_3 and 25 g/L Na_3PO_4) at 60 °C for 30 seconds. Afterwards, it was etched in a 50 g/L NaOH solution at 50 °C for 30 seconds. Finally, the sample was deoxidized with a solution of 500 mL/L HNO_3 and 30 g/L $(NH_4)HF_2$ at room temperature for 30 seconds. The sample was rinsed thoroughly after each step with DI water, dried, and immediately subjected to electro-deposition.

3.2.3 Electro-deposition

The copper electro-deposition system was set up as illustrated in Figure 3.1. A glass container was placed on top of a stirrer/hot plate, with a thermocouple placed into the electrolyte for temperature control. Obtaining a uniform coating thickness is challenging because of the geometry and topology of the foam sample. Thus, instead of using a metal sheet as an anode, a rectangular niobium mesh that mimics the foam geometry was used. The aluminum foam sample was placed in the middle of the anode mesh without contacting any side of it. In this way, each side of the foam specimen had the same distance to the anode, enabling a uniform transfer of electrons and copper cations. Meanwhile, each side of the mesh was attached with a copper anode. The attachment of the copper anode was critical to maintain the copper concentration and pH value within the electrolyte. An electrolyte of 40 g/L Cu was used at 65 °C and a pH of 7.5. A stirring bar was applied throughout the entire deposition process at 180 revolutions per minute (rpm). The current density was maintained at 4 mA/cm^2 until the desired amount of deposition was achieved. The classic Faraday's law of electrolysis [36] was applied to determine the coating mass gain as a function of time at various current densities (see Figure 3.2). It can be seen that at

lower current densities (i.e., 1 mA/cm^2 and 2 mA/cm^2), the experimental data agreed with the theoretical calculation very well, up to 6 hours of electro-deposition. However, when a higher current density (i.e., 4 mA/cm^2) was applied, the experimental data agreed with the theoretical calculation for the first 6 hours of electro-deposition, and started to level off afterwards. There are two possible reasons for this observation. First, the deposition efficiency might be lower after a thick Cu coating on the Al foam struts. Second, diffusion limitation might start to play a significant role when a thick coating thickness is gained.

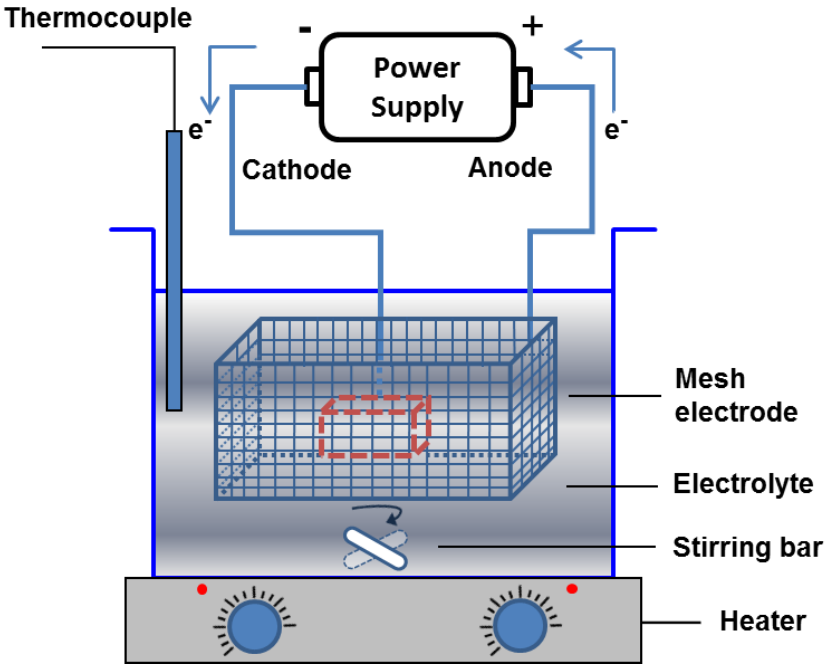

Figure 3.1 The electro-deposition system applied in this study. A rare metal rectangular bar mesh attached with copper sheets was used as the anode in the system. The aluminum foam was connected to the cathode and centered in the mesh to enable the uniform transfer of electrons and copper cations.

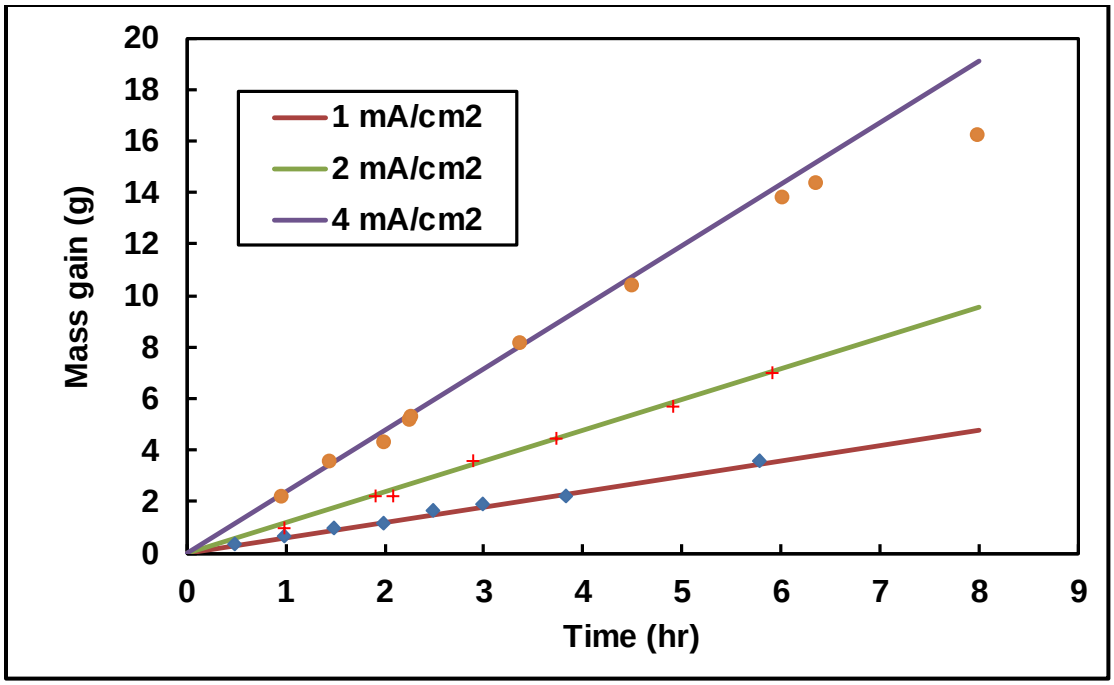

Figure 3.2 Electro-deposition kinetic studies on open-cell Al foams. Straight lines are theoretical values based on Faraday's law of electrolysis. Dots in different shapes are experimental data.

3.2.4 Scanning electron microscope (SEM) imaging

The coated and uncoated aluminum foam samples were evaluated through scanning electron microscope (SEM) imaging using a Zeiss EVO LS 25 variable pressure SEM. The microscope is equipped with an energy dispersive x-ray (EDX) detector to determine atomic compositions. The dried foams were placed into the chamber without further conditioning and a high vacuum mode was selected during the imaging. Unless otherwise stated, all SEM images were taken under a high vacuum mode at a 16 kV accelerating voltage and a 25 mm working distance. All EDX tests were done at a 16 kV accelerating voltage and a 9 mm working distance.

3.2.5 Crystallite size determination using X-ray diffraction (XRD)

The crystallite size of the nano-Cu coating was assessed through X-ray diffraction (XRD). XRD patterns were obtained on a Bruker D8 DaVinci diffractometer equipped with Cu X-ray

radiation operating at 40 kV and 40 mA. The coated foams were sliced before XRD analysis. Peak intensities were obtained by counting with the Lynxeye detector every 0.01° at sweep rates of 0.5° 2θ / min. The sample was placed in a poly(vinyl methacrylate) (PVMA) sample holder. The sample was rotated at 5 degrees per minute. No background correction was applied to the raw data. The crystallite size of deposited Cu was reported using a single Cu peak according to the Scherrer formula [39, 40].

3.2.6 Quasi-static compression test

Quasi-static compression tests of plain (uncoated) and coated foam samples were performed on a universal testing frame (United Testing Systems model SFM-20). The foam samples (25.4 mm × 25.4 mm × 50.8 mm) were tested along their long dimension. Aluminum plates (6 mm thick) were bonded (with DP-110 adhesive from 3M, St. Paul, MN) to the ends of the foam samples before testing to obtain uniform loading regions. All tests were performed at 0.1 in/min until 80 % strain was achieved. Triplicate samples of each kind were tested.

3.3 Results and discussions

When a voltage is applied, the following anodic and cathodic reactions will occur:

Anode: $Cu(s) \rightarrow Cu^{2+}(aq) + 2e^-$ (major); (Equation 3.1)

$4OH^-(aq) \rightarrow 2H_2O(l) + O_2(g) \uparrow + 4e^-$ (minor). (Equation 3.2)

Cathode: $Cu^{2+}(aq) + 2e^- \rightarrow Cu(s)$ (major); (Equation 3.3)

$2H^+(aq) + 2e^- \rightarrow H_2(g) \uparrow$ (minor). (Equation 3.4)

The Al foam is thus being deposited with Cu when it is connected to the cathode. It is known that aluminum is reactive to acid and alkali. Thus a pyrophosphate Cu electrolyte was selected because its optimum working pH is 7.5. A preliminary study using an acid Cu sulfate bath was conducted. However, the Al foam structure was partially dissolved, thus severely damaging its energy absorption capacity. Other researchers have reported applying a thin metal film before the electro-deposition in order to protect the aluminum from dissolving in harsh pH solutions [35]. However, using an electrolyte that works at neutral pH eliminates the need for this step.

3.3.1 3-D deposition visualization and uniformity

Figure 3.3 shows the deposition of copper on an open-cell Al foam sample. The foam samples were visually reddish-orange after the Cu nanocrystalline deposition. A comparison of uncoated Al foams and Cu coated composite (Cu/Al) foams with various porosities can be seen in Figure 3.4. The EDX results of a selected area reveal the full coverage (98 wt %) of Cu on top of Al. A sample was cut in middle to investigate the coating inside of the foam. Figure 3.5 is an overall top view image of the sample at the cut area. Figures 3.6 (a) and (b) are the top-view SEM images of the Cu coated sample at a sample section cut. A color contrast between the foam core material (Al) and coating (Cu) can be seen at the cross section of the cut struts. The SEM and EDX elemental mapping shown in Figure 3.7 reveal the aggregation of copper on top of the aluminum foam struts. A series of SEM images of Cu coated Al foam struts with different magnifications are provided in Figure 3.8.

(a)

(b)

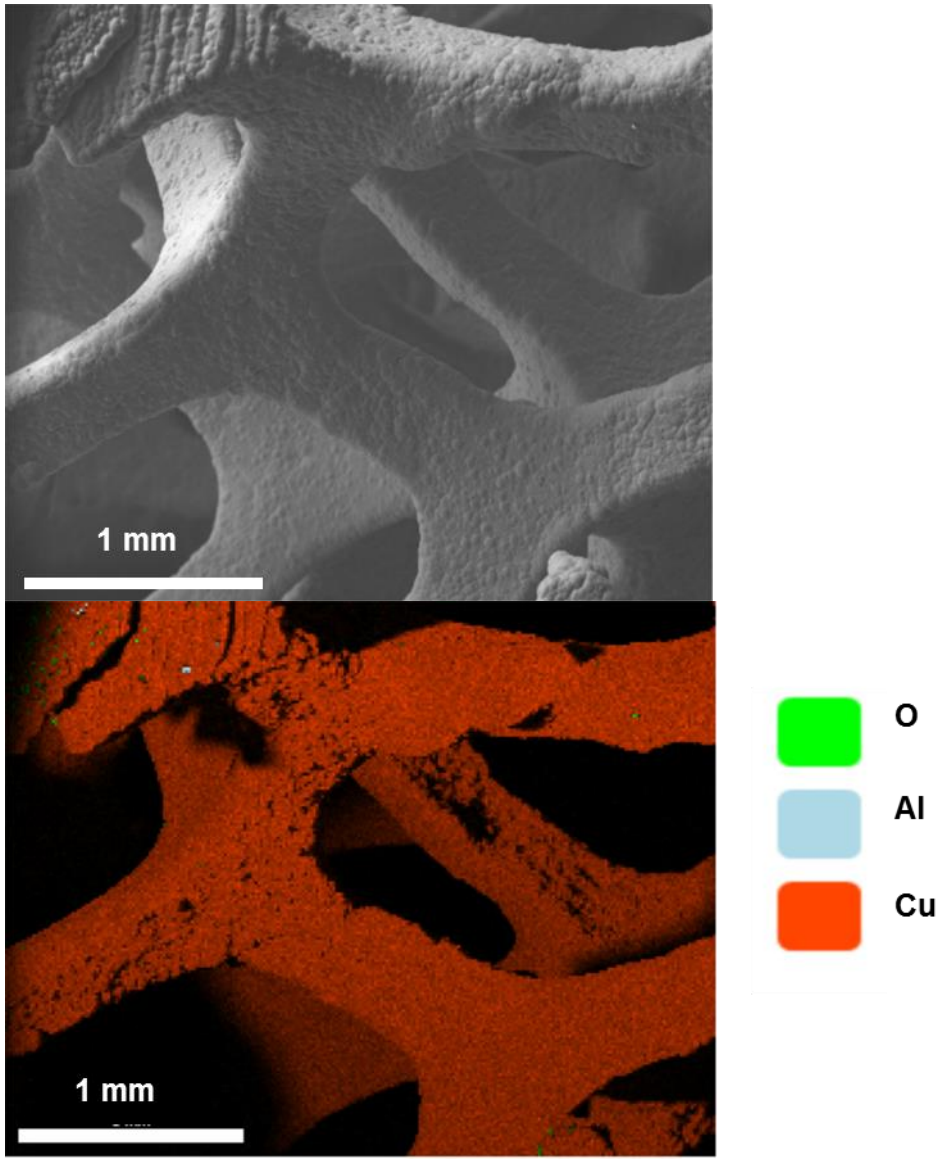

Figure 3.3 SEM (a) and EDX elmental mapping (b) on a Cu coated Al foam. The distribution of each element is: 97.6 wt % (or 91.8 at %) of Cu, 0.4 wt % (or 0.9 at %) of Al and 2.0 wt % (or 7.3 at %) of O.

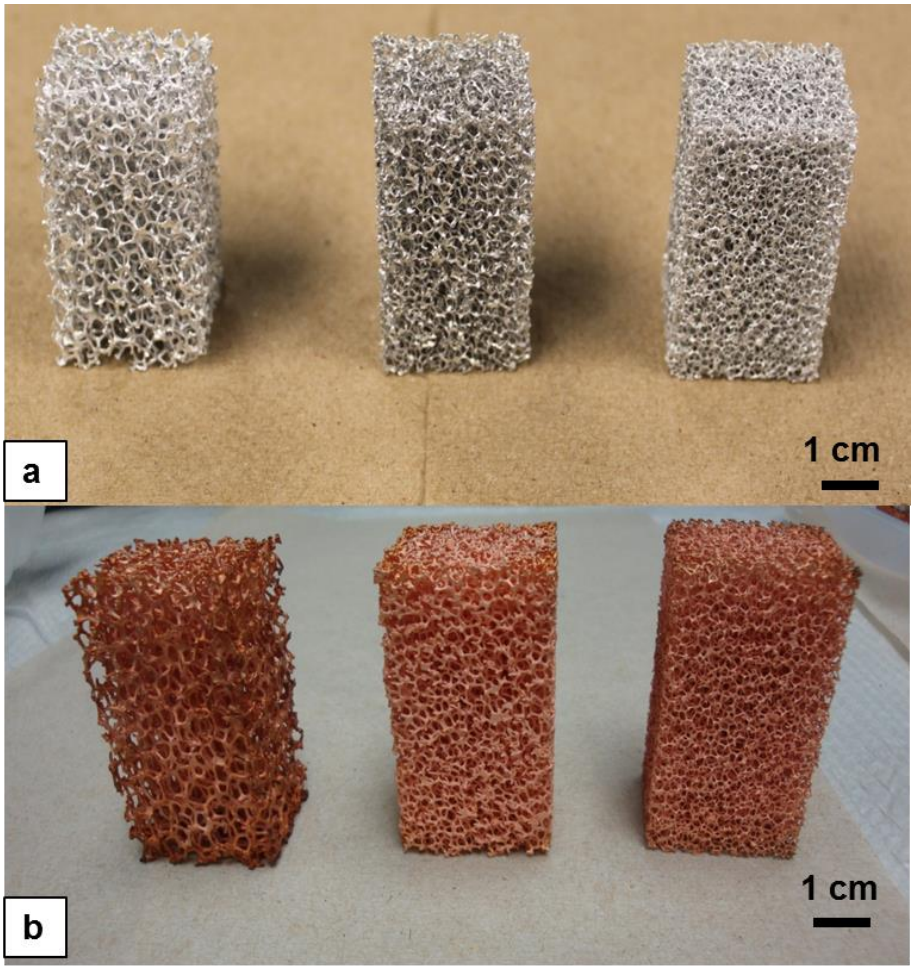

Figure 3.4 Uncoated Al foams (a) and Cu coated Al foams (b). Left: 10 PPI; middle: 20 PPI; right: 40 PPI

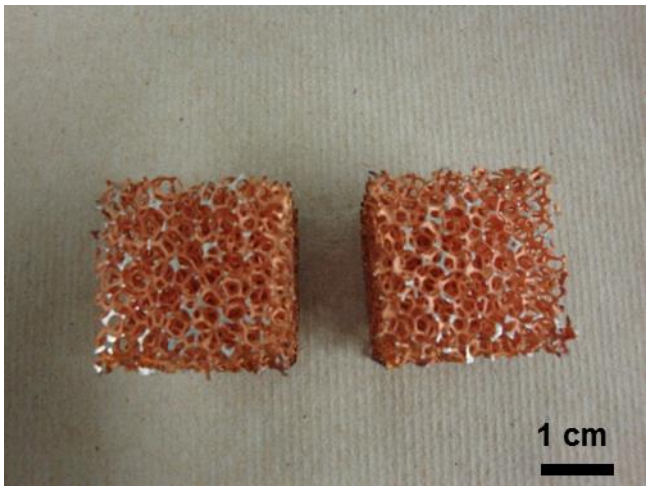

Figure 3.5 Top view digital image of Cu coated Al foams at cut area

(a)

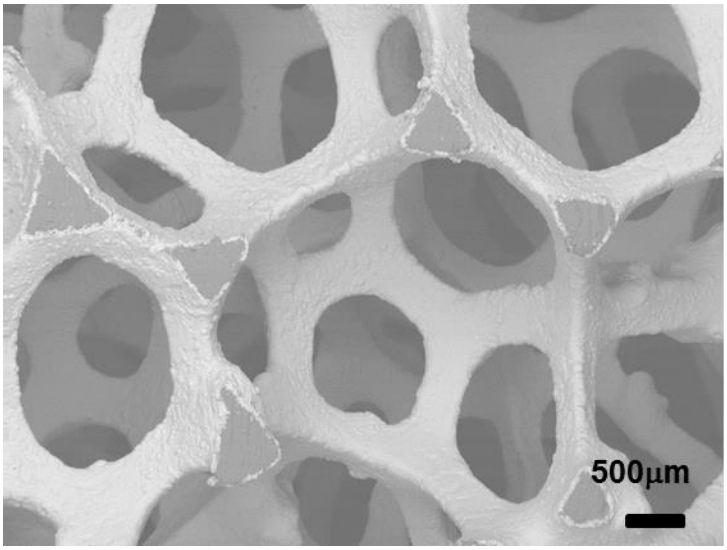

(b)

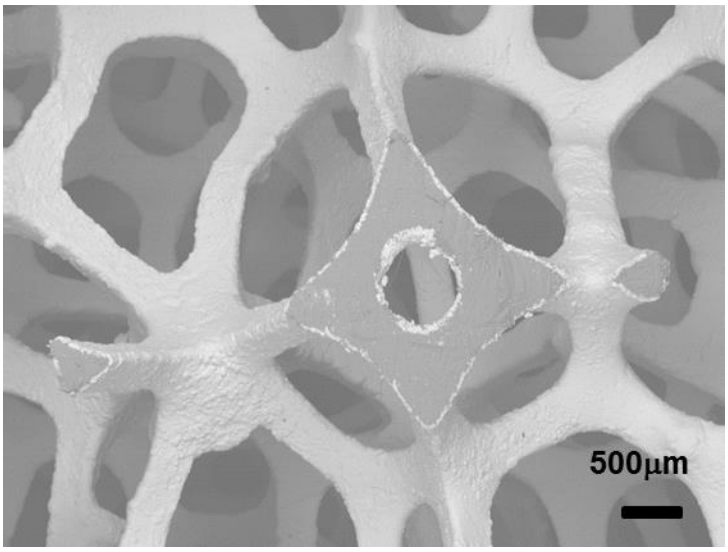

Figure 3.6 Middle section of a copper electrodeposited Al foam. a) and b) SEM images of selected areas.

(a)

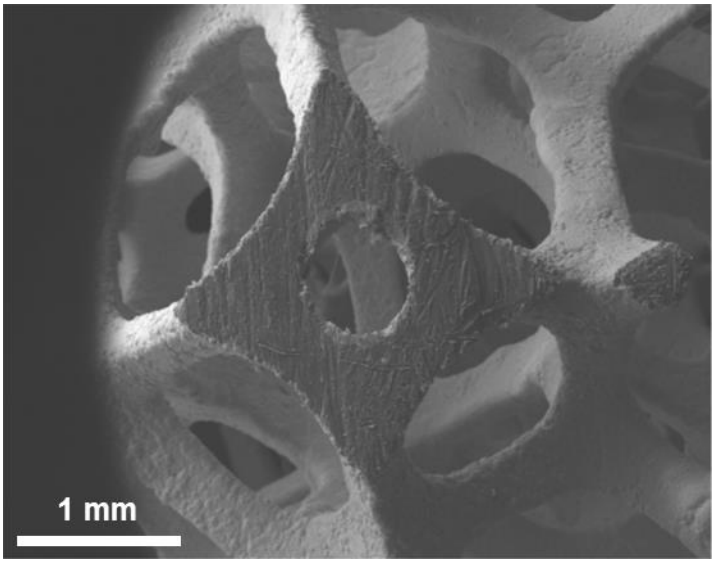

(b)

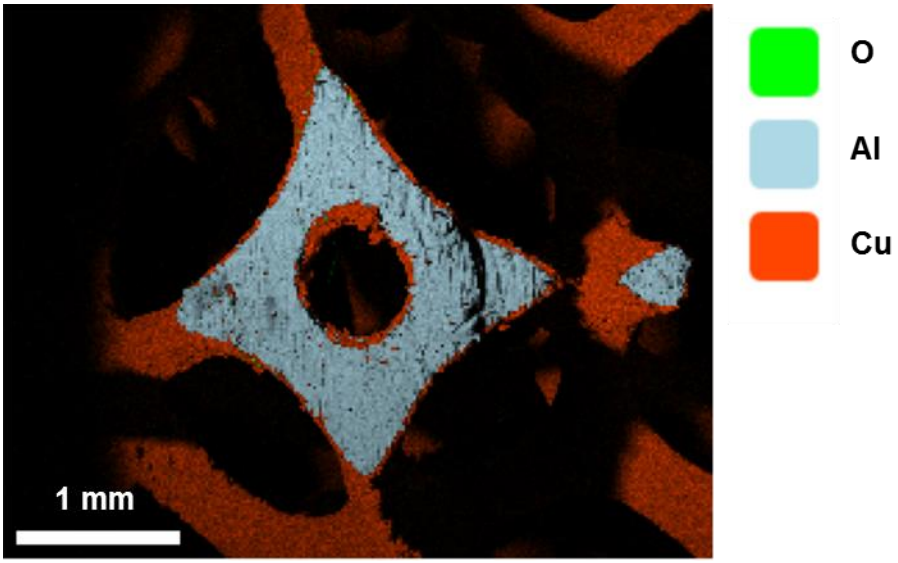

Figure 3.7 SEM (a) and EDX elemental mapping (b) at sample cut area, where Al and Cu can be seen at the same time. The distribution of each element is: 72.0 wt % (or 50.0 at %) of Cu, 24.3 wt % (or 39.7 at %) of Al and 3.7 wt % (or 10.3 at %) of O.

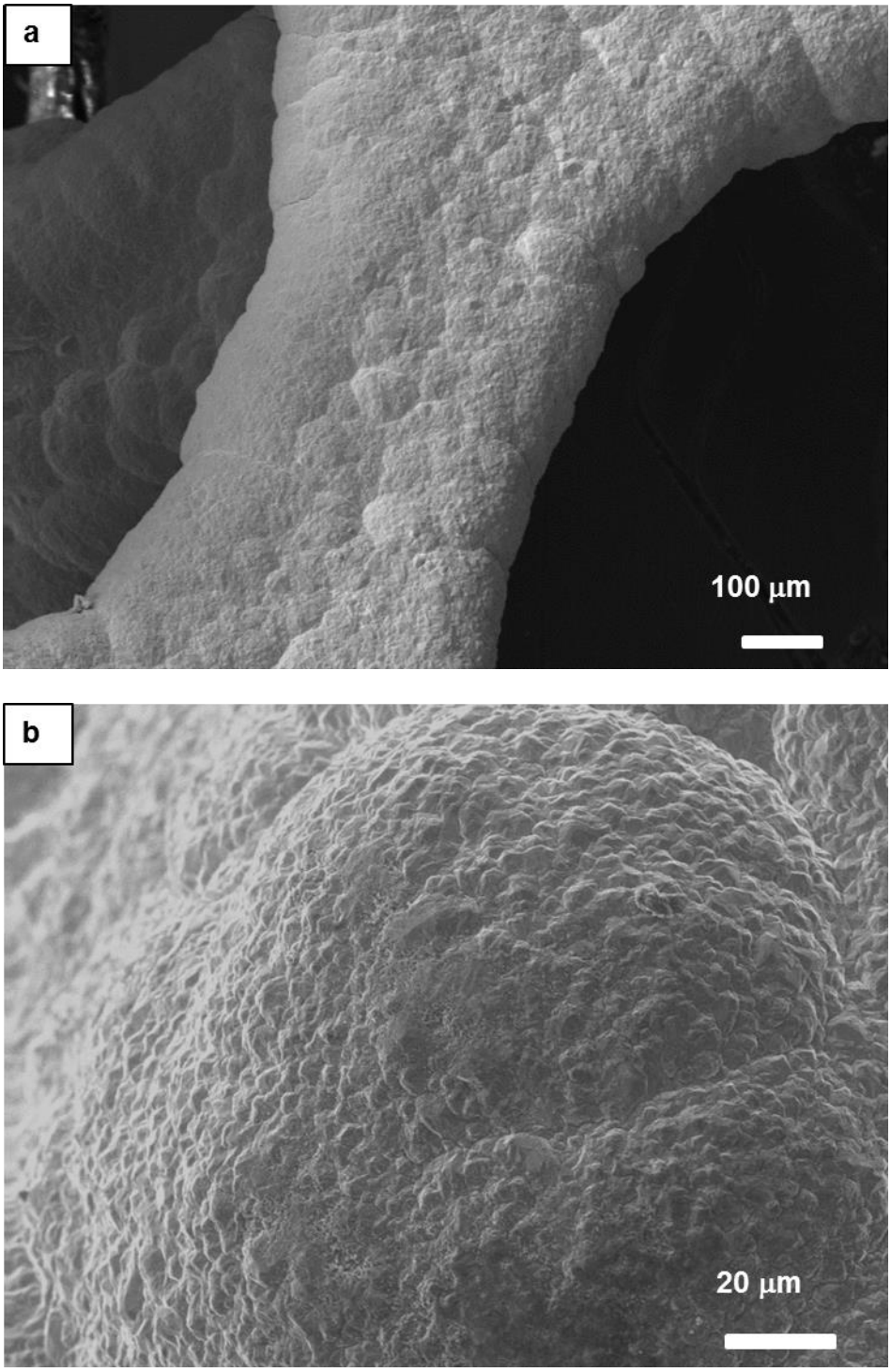

Figure 3.8 SEM images of Cu coated Al foams at different scales

Figure 3.8 (cont'd)

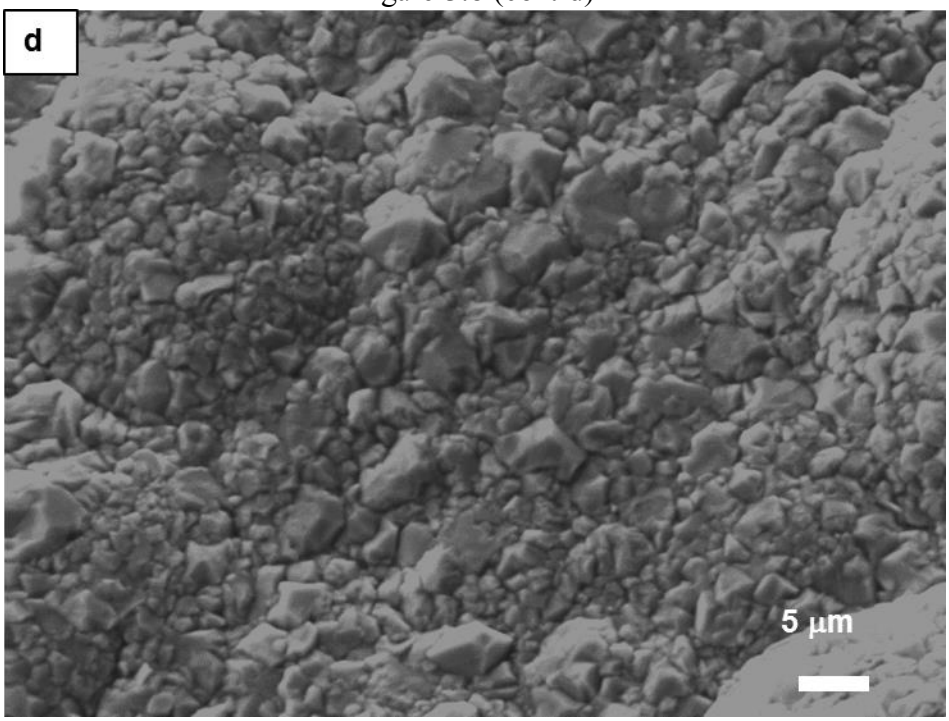

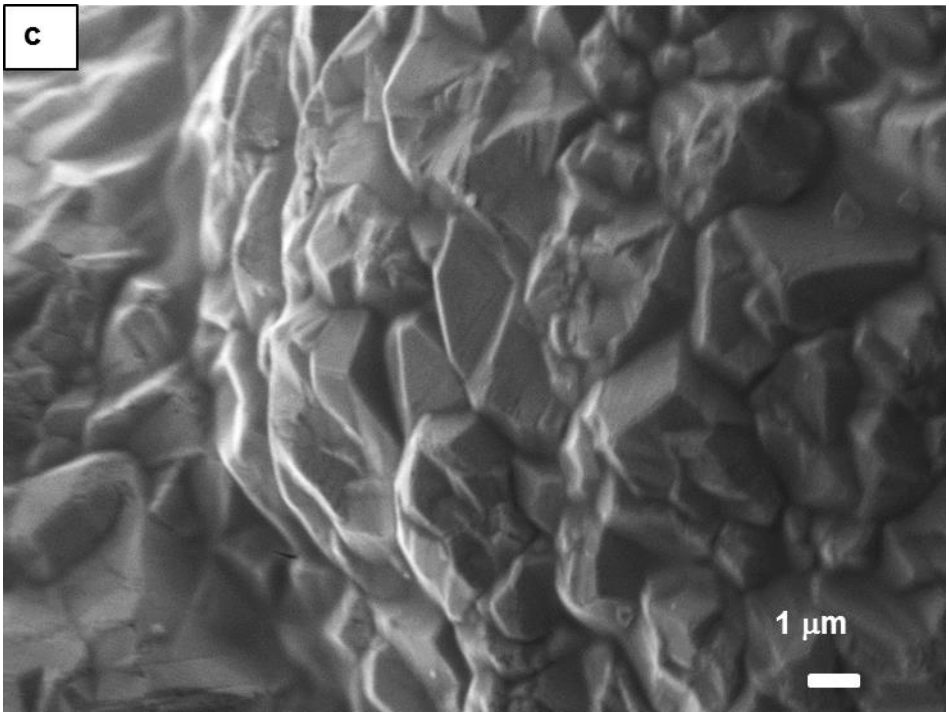

The crystallite size of the Cu coating is of interest because it has a direct impact on the macro-scale mechanical properties [41]. Crystallite size is a measure of each individual

crystallographic phase, which represents the average size of a coherent scattering domain [40]. The principle of crystallite size measurements by X-ray diffraction is based on the fact that the diffraction peak width is inversely proportional to crystallite size [4, 40]. One of the advantages of using XRD to determine the crystallite size is that XRD provides bulk sampling. Figure 3.9 shows an XRD diagram of the Cu coated foam struts. Al peaks were not observed. Cu peaks were observed at 43.3° and 50.4°, in accordance with reference values [42]. Crystalline grain size was calculated using the Scherrer formula [39, 40], as follows:

$$e = \frac{K\lambda}{b\cos\theta} \qquad \text{(Equation 3.5)}$$

where e is the crystallite size, K is the Scherrer constant, λ is the wavelength of the applied radiation, b is the full width at half maximum (FWHM) in radians, and θ is the peak position. Accordingly, using the Cu peak at 43.3°, the crystalline size of the deposited Cu was calculated to be 38 nm.

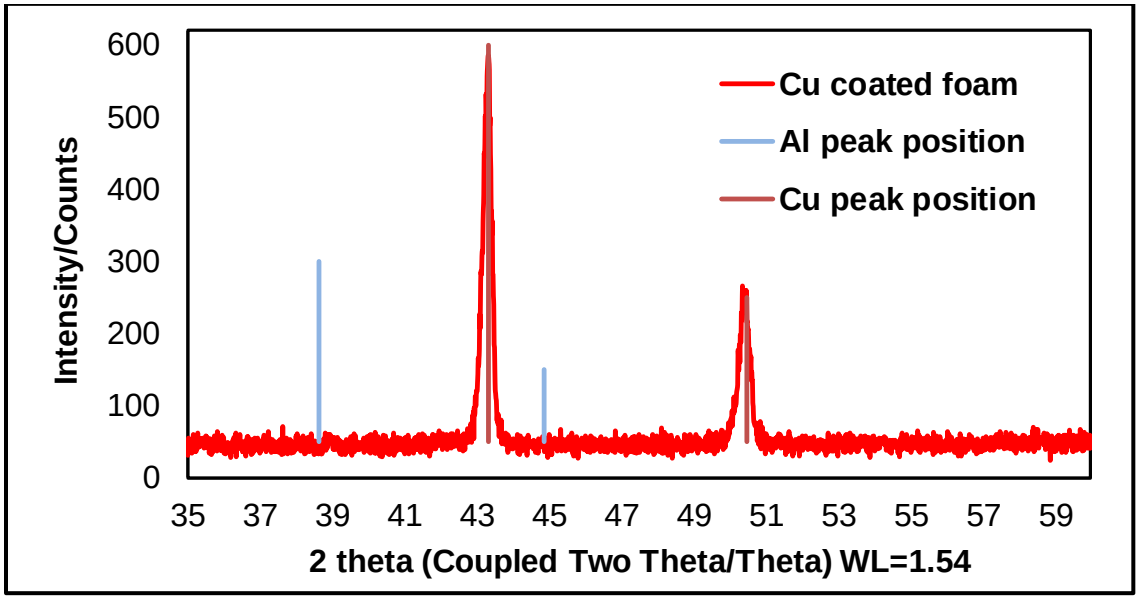

Figure 3.9 XRD pattern of a Cu coated Al foam. Crystallite size was calculated using the Cu peak at 43.3° in this curve. Using the Scherrer formula the crystalline size of deposited Cu was 38 nm.

Table 3.1 Specimen name designations and coating information

Sample ID[a]	Relative density, %	Mass gain[b], g	Average struts thickness[c], μm ± σ
US10[d]	6.08	-	390.9 ± 24.2
CS10-1[e]	6.36	7.36	478.4 ± 17.2
CS10-2	6.51	6.84	462.5 ± 20.5
CS10-3	6.39	3.25	431.6 ± 13.3
US20	5.72	-	264.9 ± 18.2
CS20-1	5.92	19.34	438.4 ± 15.4
CS20-2	6.63	6.23	339.6 ± 14.4
CS20-3	5.77	10.00	364.8 ± 13.6
CS20-4	5.79	13.58	393.8 ± 12.5
US40	6.00	-	192.0 ± 14.3
CS40-1	6.35	4.38	240.0 ± 9.6
CS40-2	6.35	14.31	314.0 ± 11.4
CS40-3	6.30	10.03	293.1 ± 18.8
CS40-4	6.30	14.30	309.3 ± 10.7

a. The samples have a relative density of 6 (±1) % unless otherwise specified.
b. Mass gain = the dry mass after deposition – the dry mass before deposition.
c. Data provided in this column is the average ± standard deviation.
d. "US" denotes uncoated sample (plain Al), and the following number is the foam pore size in pores per inch (PPI), e.g., 10 means 10 PPI foam sample.
e. "CS" denotes coated sample, the following number is the sample pore size in pores per inch (PPI) and the last number is the serial number of the sample of the same category.

A statistical evaluation was conducted to determine the uniformity of the coatings. After a varied amount of Cu was deposited on different PPI samples, the strut thicknesses (i.e., foam

ligament cross-sectional dimension) of coated and uncoated samples were compared. The average strut thickness value (see Table 3.1) was obtained based on at least 30 measurements at different locations of each sample. Compared with the uncoated samples, the strut thicknesses deviations of coated samples were almost unchanged, indicating that the Cu deposition did not introduce further deviation on the strut thickness, i.e., the Cu was uniformly deposited on to the Al foam struts.

3.3.2 Quasi-static compression test and energy absorption calculation

Uncoated (plain Al foam) and Cu coated Al foams were tested under quasi-static compression load to investigate the energy absorption capacity of the samples. Images of a series of Cu coated foams before and after the compression tests are shown in the supplementary data, SD5. For the tests reported in this section, all of the Cu coated samples were based on Al foams with the same relative density of 6 (±1) %. Using the corresponding stress-strain curve obtained from testing, the absorbed energy per volume can be calculated by integrating the area under the curve from 0 up to the densification strain, as follows [13]:

$$E_v = \int_0^{\varepsilon_D} \sigma \; d\varepsilon \qquad \text{(Equation 3.6)}$$

where σ represents the stress and ε_D represents the densification strain. Many algorithms have been proposed to calculate the densification strain [8, 13, 16], but most of them cannot be applied to the composite material system considered here. In this study, the densification strain was defined as the strain at which the stress was equal to 1.5 times the maximum stress before 50 % strain for all samples [16].

(a)

(b)

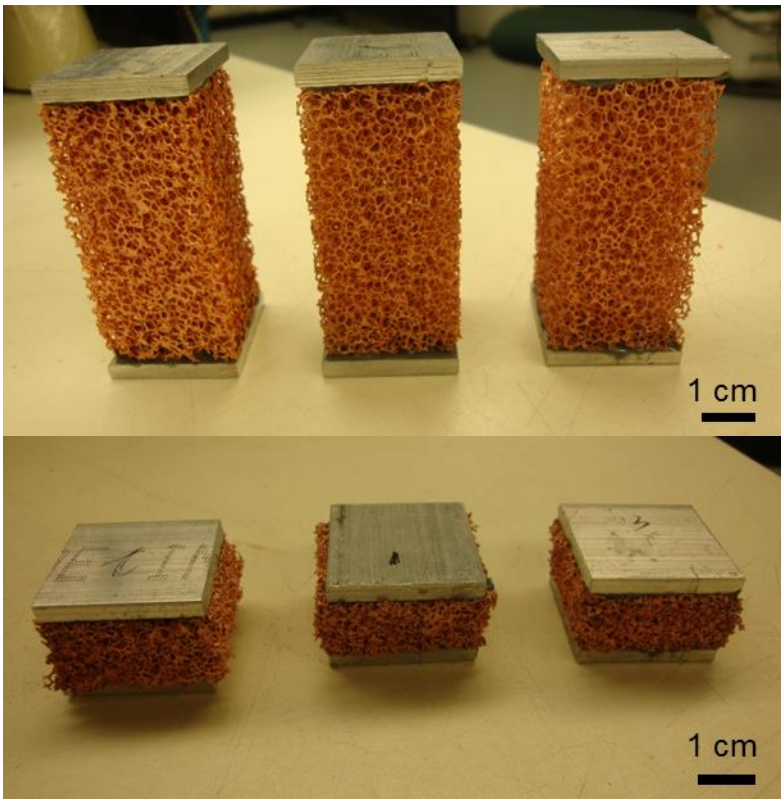

Figure 3.10 Cu coated Al foams before (a) and after (b) quasi-static compression tests

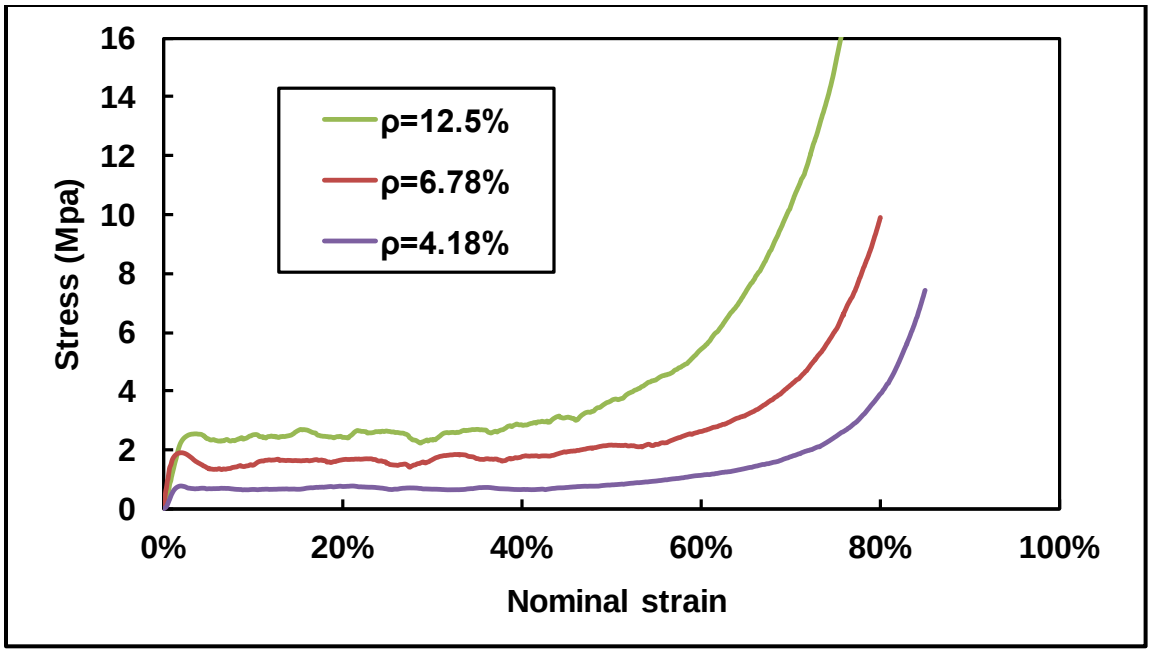

Figure 3.11 Compressive stress-strain response of 10 PPI open-cell Al foams with different relative densities (i.e., different strut thicknesses).

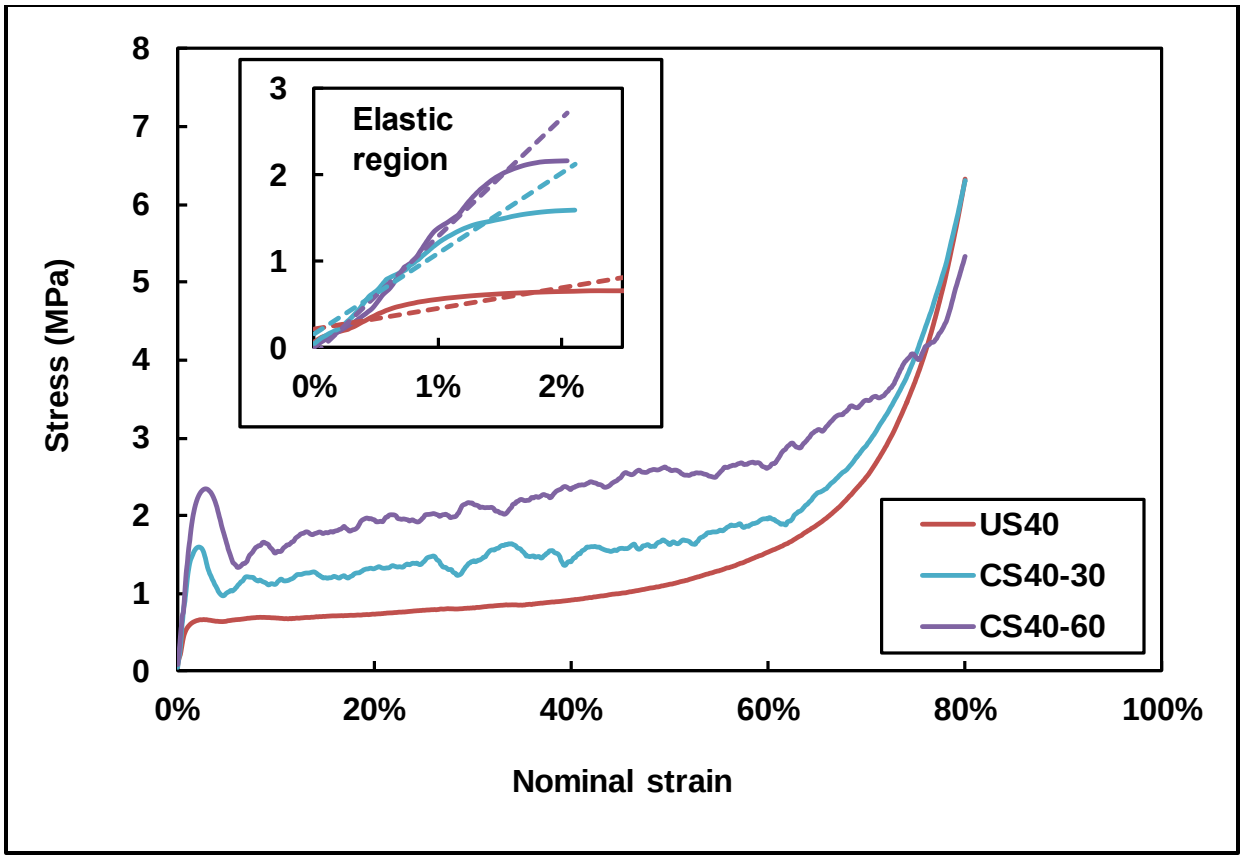

Figure 3.12 Compressive stress-strain responses of 40 PPI uncoated and coated foam samples. The samples were compressed at 0.1 in/min, until 80 % strain was achieved. The embedded figure represents the enlarged elastic region. Linear trend lines were used to fit the curve of the elastic region of each sample.

Table 3.2 Important parameters and calculations for 40 PPI uncoated and copper coated samples

Sample ID	Elastic modulus, MPa	Plastification stress, MPa	Densification strain, %	Energy absorbed, J	Enhancement
US40	33.49 ± 10.98	0.64 ± 0.12	62.42 ± 0.04	16.65 ± 2.32	--
CS40-30	84.82 ± 7.56	1.47 ± 0.13	67.75 ± 0.37	31.77 ± 1.39	91 %
CS40-60	114.95 ± 14.93	2.13 ± 0.19	72.00 ± 1.28	48.52 ± 6.31	192 %

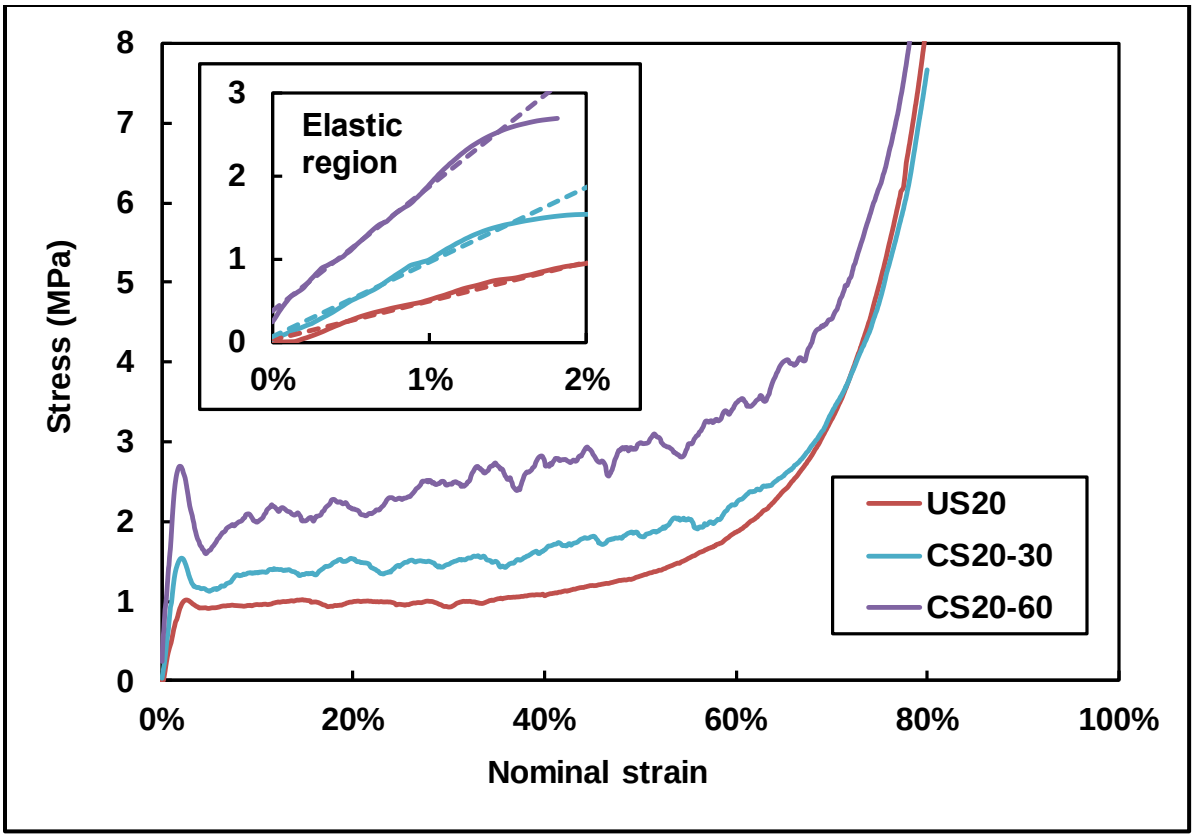

Figure 3.13 Compressive stress-strain responses of 20 PPI uncoated and coated foam samples. The embedded figure represents the enlarged elastic region. Linear trend lines were used to fit the curve of the elastic region of each sample.

Table 3.3 Important parameters and calculations for 20 PPI uncoated and copper coated samples

Sample ID	Elastic modulus, MPa	Plastification stress, MPa	Densification strain, %	Energy absorbed, J	Enhancement
US20	58.29 ± 8.24	1.08 ± 0.05	62.25 ± 0.68	20.69 ± 1.34	--
CS20-30	113.57 ± 26.60	1.67 ± 0.14	66.50 ± 0.70	36.76 ± 0.29	78 %
CS20-60	141.51 ± 15.29	2.46 ± 0.19	70.77 ± 0.60	53.16 ± 3.72	157 %

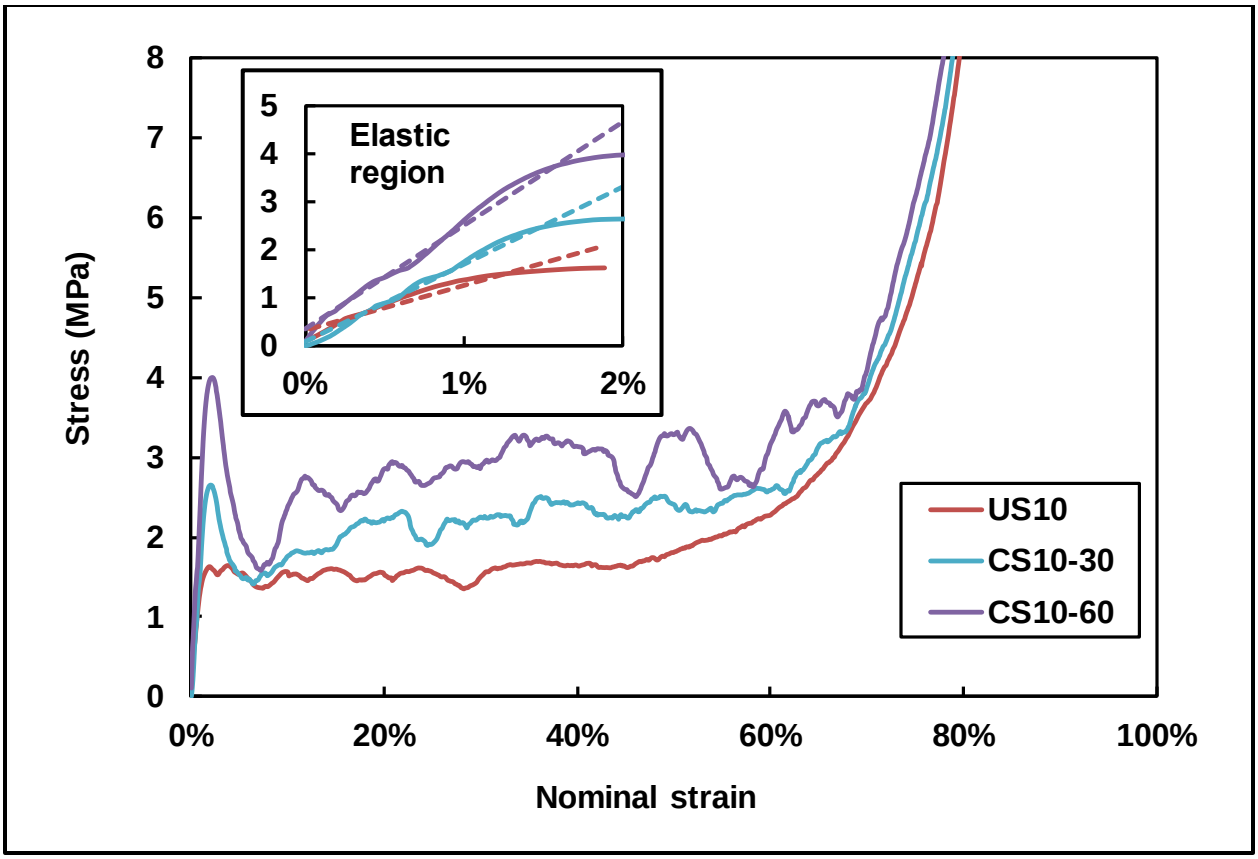

Figure 3.14 Compressive stress-strain responses of 10 PPI uncoated and coated foam samples. The samples were compressed at 0.1 in/min, until 80 % strain was achieved. The embedded figure represents the enlarged elastic region. Linear trend lines were used to fit the curve of the elastic region of each sample.

Table 3.4 Important parameters and calculations for 10 PPI uncoated and copper coated samples

Sample ID	Elastic modulus, MPa	Plastification stress, MPa	Densification strain, %	Energy absorbed, J	Enhancement
US10	99.07 ± 11.78	1.77 ± 0.11	64.58 ± 0.67	35.27 ± 1.39	--
CS10-30	157.07 ± 13.87	2.70 ± 0.07	69.86 ± 0.90	53.57 ± 0.64	52 %
CS10-60	192.87 ± 20.94	3.49 ± 0.39	74.49 ± 0.36	69.17 ± 4.41	96 %

A comparison of the stress-strain response among uncoated Al foam samples with different relative densities was made to assess the effect of this parameter on energy absorption capacity. A representative curve of each kind was selected for the comparison. For the same

sample volume, higher relative density means thicker foam struts. As expected, the plateau stress increases with higher strut thickness; but the densification strain decreases as shown in Figure 3.11. Thus, thickening the foam struts with the same material will compromise the improvement on energy absorption capacity.

Figures 3.12-3.14 show the stress-strain curves of coated and uncoated foam samples with different pore sizes (i.e., PPI). The embedded figures represent the enlarged elastic region of the curves. Tables 3.2-3.4 list the parameters and energy absorption calculations for each curve corresponding to the different pore size samples. In all cases, the Cu/Al composite foam samples had distinct features from the plain Al ones. In the elastic region, the stiffness, or effective modulus, of the coated samples was higher as indicated by the steeper slopes in the response. As expected, the stiffness gain increased for samples with thicker coating. The plastic or collapse stress of the coated samples was higher, indicating a larger flexural plastic capacity of the reinforced struts. The coated foams, however, showed a sudden drop in capacity upon initiating the plastic collapse region, a feature that was more pronounced for thicker coatings and for lower PPI foams This behavior is attributed to the combined effect of failure of the coating material and then the sudden loss of load-carrying capacity due to the inelastic buckling of the cell struts, for which the accumulated strain energy prior to instability will increase proportionally with the coating thickness. This behavior was also observed by Jung et al [22] in the response of Ni coated open-cell Al foams. In the plastic region, the coated samples exhibited a response with a sustained higher stress along with strain hardening effect that increased for increased coating thickness. A similar behavior in the plastic region has been observed on density-graded Al foams [43, 44]. However, more importantly, with the limited coating thicknesses (30 μm and 60 μm), the densification strain of the coated samples remained almost the same as that of the uncoated

samples. This is the first experimental data showing this unique behavior. As a result, the noted positive features of the Cu coated foams led to a higher energy absorption capacity with respect to their corresponding uncoated foam precursor.

The set of three curves shown in Figures 3.12-3.14, respectively, correspond to uncoated foam samples with the same relative density (6 ±1 %). The strut thickness of a plain uncoated foam samples varies with pore size. The US10 (uncoated samples, 10 PPI) have the largest strut thickness, around 391 μm; and the US40 samples have the smallest strut thickness, around 192 μm. For this reason, a given coating thickness will have a different level of improvement on energy absorption capacity for different PPI samples. It should be noted that all the coating thicknesses are defined as one half of the subtraction of foam ligament cross-sectional dimension after and before coating. The enhancement in energy absorption capacity for 40, 20 and 10 PPI samples with coating thicknesses of 30 and 60 μm is listed in Tables 3.2-3.4. The enhancement here is quantitatively defined as the difference of absorbed energy between coated and uncoated sample, divided by the absorbed energy of uncoated sample. As expected, all samples with thinner coatings exhibited less enhancement of energy absorption capacity. The CS40-60 samples had the most enhancement of energy absorption capacity over the corresponding plain foam: 192 % (see Table 3.2). For the same coating thickness, the CS10-60 samples had the least enhancement in energy absorption capacity (see Table 3.4).

The investigation in this section demonstrated that energy absorption capacity enhancement of the open-cell Al foams is a strong function of foam topology (i.e., foam pore size), relative density, and coating thickness. The results indicated beneficial strategies in improving energy absorption capacity of Al foam materials. That is, to reinforce foam struts with

a stiff material so that the impact on the foam porosity and structure would be limited. In this way a higher plastification will be achieved, without severely reducing the densification strain.

3.3.3 Comparison between coated and uncoated foam samples with same strut thickness

The comparison between coated (Cu/Al composite) and uncoated (plain Al) foam samples with the same overall strut thickness is of our interest because the coating will be meaningful only if the composite material system exhibits enhanced performance over an equivalent plain/homogeneous one. This was made possible with careful control of the 3-D foam coating technique described in this work. A set of 10 PPI samples with different relative densities was chosen to make the comparison. With the same pore size and sample volume, different relative densities result in different strut thicknesses. The strut thickness of 10 PPI Al foam with a 12 (±1) % relative density is around 580 μm, while the strut thickness of 10 PPI Al foam with a 6 (±1) % relative density is about 391 μm. With the same aforementioned electro-deposition setup, foam samples with a 6 (±1) % relative density were coated with Cu until an equivalent strut thickness to that in a foam with 12 (±1) % relative density was achieved. The quasi-static compressive stress-strain behavior of the plain and coated samples is shown in Figure 3.15. CS10-95 designates an Al foam of 6 (±1) % relative density with an approximately 95 μm Cu coating thickness. US10-HD refers to an uncoated Al foam with a 12 (±1) % relative density. Table 3.5 lists and compares the absorbed energy by these two samples, where each value is the average of three tests.

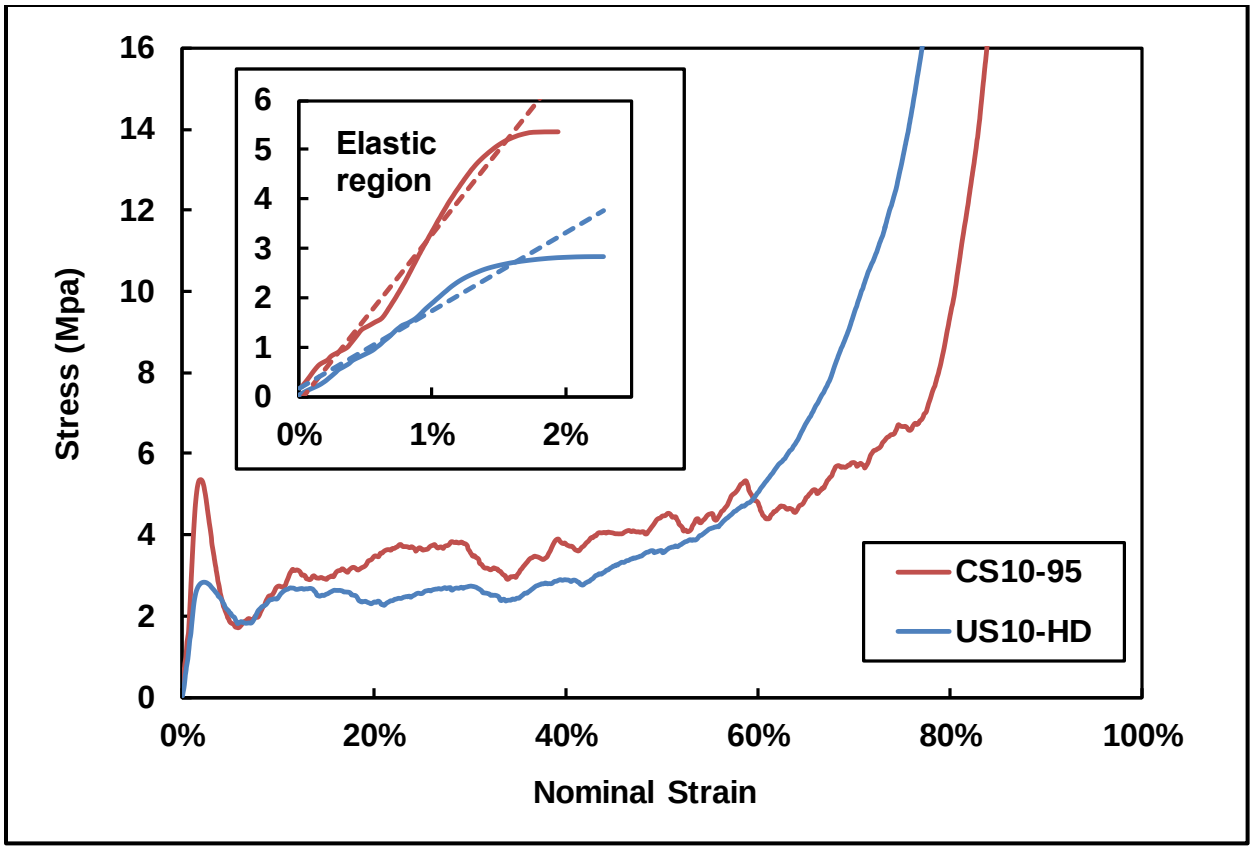

Figure 3.15 Compressive stress-strain responses of 10 PPI samples. "US10-HD" denotes an uncoated 10 PPI sample, with high density (12 (±1) % relative density), and a strut thickness around 580 μm; "CS10-95" represents a coated 10 PPI sample, starting from a 6 (±1) % relative density, with an approximately 95 μm coating thickness. Al foams with 6 (±1) % relative density were Cu coated until their strut thickness was equivalent to Al foams with 12 (±1) % relative density. All samples were tested under quasi-static compression at 0.1 in/min. The embedded figure represents the enlarged elastic region. Linear trend lines were used to fit the curve of the elastic region of each sample.

Table 3.5 Energy absorption calculations and comparison based on Figure 3.15

Sample ID	Energy absorbed, J	Enhancement
US10-HD[a]	54.36 ± 2.85	--
CS10-95[b]	94.12 ± 7.98	73 %

a. "US10-HD" denotes an uncoated 10 PPI sample with a high relative density (12 ±1 %). The strut thickness is around 580 μm.

b. "CS10-95" denotes a coated 10 PPI sample starting from a 6 (±1) % relative density foam. The coating thickness is approximately 95 μm.

From Figure 3.15 it can be seen that the CS10-95 sample had higher elastic modulus and a higher plastic capacity. As previously noted, the coated sample has a steep load drop upon initiation of the plastic region. As previously discussed, this effect is attributed to the larger strain energy accumulated by the stiffer coated struts, which upon suffering from inelastic buckling leads to increased loss of load capacity. Again, a similar behavior has been observed in Ni-coated Al foams [35]. However, two further points must be noted. First, it is hypothesized that the sudden loss of capacity of the coated struts may also be related to the sudden failure or debonding of the coating, which implies that the drop in capacity can be reduced if the coating material can fail in a more gradual manner or if the interfacial bonding between the Cu coating and the substrate is improved. This remains to be proven. The second point follows from the observation that the stress drop is also observed in the uncoated sample. In this case the drop is related to the larger strut thickness in the lower PPI sample, which leads to more stored strain energy before collapse. A situation that is analogous to the effect of increasing capacity and stiffness with added coating.

In the plastic region the coated foams exhibited strain hardening behavior similar to the coated samples in the previous section and very similar to the uncoated samples. However, the densification strain in the coated 10 PPI sample is notably higher than for the uncoated sample, which shows the efficiency of the coating material in improving energy absorption capacity. Calculations show a 73 % enhancement in terms of energy absorption capacity. The result indicates that the composite foam system has superior energy absorption capacity to the plain Al foam; or, that for a target energy absorption capacity, the required strut thickness of the composite foam system could be smaller.

3.4 Conclusions

This study presents a novel approach to enhance the energy absorbing characteristic of open-cell Al foams by reinforcing them through a 3-D copper nano-crystalline electro-deposition process. The presented investigation was aimed at demonstrating the hypothesis that a stiff nano-structured metal coating on an open-cell foam would lead to enhanced energy absorption under compressive load by increasing the elastic and plastic stress capacity of the composite foam material with minimum impact on the strut thickness and porosity, thus avoiding a significant reduction on the foam densification strain. A non-cyanide 3-D Cu electro-deposition system was developed and successfully implemented to achieve uniform deposition on complex 3-D open-cell Al foam samples. A variety of characterization methods were used to confirm that the processing setup helped achieve uniform Cu nano-crystalline (i.e., 38 nm) depositions.

Quasi-static compression tests of nano-Cu coated Al foams showed that the reinforcement strategy helped increase the plateau stress without compromising the densification strain. The energy absorption capacity enhancement from coated and uncoated foams was systematically investigated and proved to be a strong function of the foam relative density, cell topology (pore size, strut thickness, etc.) and the electro-deposition conditions. The advantage of a composite foam system was investigated by comparing the compressive performance of coated and uncoated foam samples with the same overall strut thickness, which showed that the Cu nano-crystalline coated Al foam possessed an elongated plastic region and therefore exhibited better energy absorbing capability.

REFERENCES

REFERENCES

1. Lefebvre L-P, Banhart J, Dunand DC. Porous metals and metallic foams: current status and recent developments. Advanced Engineering Materials 2008;10(9): 775-787.

2. Davis GJ, Zhen S. Metallic foams: their production, properties and applications. Journal of Materials Science 1983;18(7): 1899-1911.

3. Ashby MF, Medalist RFM. The mechanical properties of cellular solids. Metallurgical and Materials Transactions A 1983;14(9): 1755-1769.

4. Meller MA, inventor; Produit Métall. pour l'obtention d'objets Laminés,Moulés ou Autres, et Proc. Pour sa Fabrication. France patent 615.147. 1925.

5. Sosnick B, inventor; Process for making foamlike mass of metal. United States patent 2434775. 1948.

6. Elliott JC, inventor; Method of producing metal foam. United States patent 2751289. 1956.

7. Gibson LJ, Ashby MF. Cellular Solids: Structure and Properties. Cambridge, UK: Cambridge University Press; 1999.

8. Ashby MF. The properties of foams and lattices. Philosophical Transactions of the Royal Society, A 2006;364(1838): 15-30.

9. Banhart J. Manufacture, characterisation and application of cellular metals and metal foams. Progress in Materials Science 2001;46(6): 559-632.

10. Bicelli LP, Bozzini B, Mele C, D'Urzo L. A review of nanostructural aspects of metal electrodeposition. International Journal of Electrochemical Science 2008;3(4): 356-408.

11. Akiyama S, Ueno H, Imagawa K, Kitahara A, Nagata S, Morimoto K, et al., inventors; Foamed metal and method of producing same. United States patent 4713277. 1987.

12. Miyoshi T, Itoh M, Akiyama S, Kitahara A. ALPORAS aluminum foam: production process, properties, and applications. Advanced Engineering Materials 2000;2(4): 179-183.

13. Evans AG, Hutchinson JW, Ashby MF. Multifunctionality of cellular metal systems. Progress in Materials Science 1998;43(3): 171-221.

14. Gibson L. Mechanical behavior of metallic foams. Annual Review of Materials Science 2000;30: 191-227.

15. Jang W-Y, Kyriakides S. On the crushing of aluminum open-cell foams: Part I. experiments. International Journal of Solids and Structures 2009;46(3-4): 617-634.

16. Krishna BV, Bose S, Bandyopadhyay A. Strength of open-cell 6101 aluminum foams under free and constrained compression. Materials Science and Engineering A 2007;452-453(15): 178-188.

17. Lu TJ, Stone HA, Ashby MF. Heat transfer in open-cell metal foams. Acta Materialia 1998;46(10): 3619-3635.

18. Fuganti A, Lorenzi L, Hanssen AG, Langseth M. Aluminium foam for automotive applications. Advanced Engineering Materials 2000;2(4): 200-204.

19. Baumeister J, Banhart J, Weber M. Aluminum foams for transport industry. Materials & Design 1997;18(4-6): 217-220.

20. Hendricks TR, Lee I. Wrinkle-free nanomechanical film: control and prevention of polymer film buckling. Nano Letters 2007;7(2): 372-379.

21. Dingrevillea R, Qua J, Cherkaoui M. Surface free energy and its effect on the elastic behavior of nano-sized particles, wires and films. Journal of the Mechanics and Physics of Solids 2005;53(8): 1827-1854.

22. Jang W-Y, Kraynik AM, Kyriakides S. On the microstructure of open-cell foams and its effect on elastic properties. International Journal of Solids and Structures 2008;45(7-8): 1845-1875.

23. Hendricks TR, Wang W, Lee I. Buckling in nanomechanical films. Soft Matter 2010;6(16): 3701-3706.

24. Hendricks TR, Lu J, Drzal LT, Lee I. Intact pattern transfer of conductive exfoliated graphite nanoplatelet composite films to polyelectrolyte multilayer platforms. Advanced Materials 2008;20(10): 2008-2012.

25. Ahn JS, Hendricks TR, Lee I. Control of specular and diffuse reflection of light using particle self-assembly at the polymer and metal interface. Advanced Functional Materials 2007;17(17): 3619-3625.

26. Srivastava D, Hendricks TR, Lee I. Step-edge like template fabrication of polyelectrolyte supported nickel nanowires. Nanotechnology 2007;18(24): 245305.

27. Hendricks TR, Dams EE, Wensing ST, Lee I. Effects of catalyst introduction methods using PAMAM dendrimers on selective electroless nickel deposition on polyelectrolyte multilayers. Langmuir 2007;23(13): 7404-7410.

28. Hendricks TR, Lee I. A versatile approach to selective and inexpensive copper patterns using polyelectrolyte multilayer coatings. Thin Solid Films 2006;515(4): 2347-2352.

29. Lu J, Do I, Fukushima H, Lee I, Drzal LT. Stable aqueous suspension and self-assembly of graphite nanoplatelets coated with various polyelectrolytes. Journal of Nanomaterials 2010;Article ID 186486.

30. Lu J, Do I, Drzal LT, Worden RM, Lee I. Nanometal-decorated exfoliated graphite nanoplatelet based glucose biosensors with high sensitivity and fast response. Acs Nano 2008;2(9): 1825-1832.

31. Lee I, Wool RP. Controlling amine receptor group density on aluminum oxide surfaces by mixed silane self assembly. Thin Solid Films 2000;379(1-2): 94-100.

32. Lee I, Wool RP. Polymer adhesion vs substrate receptor group density. Macromolecules 2000;33(7): 2680-2687.

33. Bouwhuisa BA, McCreab JL, Palumbob G, Hibbard GD. Mechanical properties of hybrid nanocrystalline metal foams. Acta Materialia 2009;57(14): 4046-4053.

34. Gordona LM, Bouwhuisa BA, Suralvoa M, McCreab JL, Palumbob G, Hibbard GD. Micro-truss nanocrystalline Ni hybrids. Acta Materialia 2009;57(3): 932-939.

35. Jung A, Natter H, Diebels S, Lach E, Hempelmann R. Nanonickel coated aluminum foam for enhanced impact energy absorption. Advanced Engineering Materials 2011;13(1-2): 23-28.

36. Rieger PH. Electrochemistry. 2nd edition ed. New York, NY: Springer; 1994.

37. Avallone EA, III TB, Sadegh A. Marks' Standard Handbook for Mechanical Engineers, Eleventh Edition. New York: McGraw-Hill Professional; 2006.

38. Standard guide for preparation of aluminum alloys for electroplating. American Society for Testing and Materials; 2005.

39. Scherrer P. Bestimmung der grösse und der inneren struktur von kolloidteilchen mittels röntgenstrahlen. Gesellschaft der Wissenschaften zu Göttingen 1918;26: 98-100.

40. Langford JI, Wilson AJC. Scherrer after sixty years: A survey and some new results in the determination of crystallite size. Journal of Applied Crystallography 1978;11(2): 102-113.

41. Ibañez A, Fatás E. Mechanical and structural properties of electrodeposited copper and their relation with the electrodeposition parameters. Surface and Coatings Technology 2005;191(1): 7-16.

42. Swanson HE. Standard x-ray diffraction powder patterns: United States National Bureau of Standards; 1953.

43. Brothers AH, Dunand DC. Density-graded cellular aluminum. Advanced Engineering Materials 2006;8(9): 805-809.

44. Brothers AH, Dunand DC. Mechanical properties of a density-graded replicated aluminum foam. Materials Science and Engineering A 2008;489(1-2): 439-443.

Chapter 4 A facile method of nickel electroless deposition on various neutral hydrophobic polymer surfaces

4.0 Abstract

In this chapter, a facile "dip & rinse" method for nickel (Ni) electroless deposition on hydrophobic polymer surfaces is reported. The hydrophobic interactions between Poly (allylamine hydrochloride) (PAH) and polymer substrates help eliminate the need for toxic and/or harsh surface treatment steps for catalyst adsorption/immobilization. Various hydrophobic polymer surfaces with different geometries and dimensions, including low density polyethylene (LDPE), high density polyethylene (HDPE), polypropylene (PP) and polystyrene (PS) thin sheets, PE pellets, as well as non-functionalized PS microspheres, were tested. In all experiments, Ni was successfully deposited onto these hydrophobic polymer surfaces. Studies showed that, without the PAH, Ni coating was not able to form on any of these surfaces. Kinetic studies on polymer thin sheets examples showed that, with 2 hours of deposition, an approximately 2 μm thickness was achieved. A prove-of-concept study showed that Ni coated polymer thin sheets can be further electroplated with heterogeneous metal (Cu), hence enabling a faster thickness growth over time.

4.1 Introduction

Metal deposition onto heterogeneous materials (also referred to as "metallization") is of researchers' interest because merits of metals can be added to the substrate. The improved overall properties are usually ascribed to the properties associated with metals, such as abrasion resistance, friction reduction, electrical and thermal conductivity, or even mechanical hardening [1-5]. The complexity of the studies usually exists due to their inherent lack of affinity to each other, although can be overcome by surface modifications [1, 6-10]. The metal deposition onto polymer is a typical example.

Various metal deposition strategies have been applied for more than decades, or even a century. For non-conductive surfaces such as polymers, physical and chemical vapor deposition (PVD and CVD) [11-13], sputter deposition [3, 14], and electroless deposition [15-20] are all employed strategies. Among these methodologies, electroless deposition is widely used because of its equipment simplicity and flexibility. Electroless metal deposition is a catalytic, redox reaction of a metal ion in an aqueous solution (with a reducing chemical agent), without external electrical field being applied [21]. It usually includes three main steps [17, 18, 22]: 1) a surface treatment or conditioning; 2) application of an appropriate catalyst (typically noble metal catalyst, e.g. tin, palladium) on the substrate surface; 3) metal electroless deposition. Rinsing is required between the steps. However, in the first step, in order to modify the functionality of the substrate surface so that catalyst can sequentially be attached, harsh and/or toxic surface conditioning steps are usually employed. The surface conditioning includes a harsh chemical etching [21, 23] (e.g. sulfuric and chromic acids), or a plasma treatment [6, 16, 24], or a UV source radiation [7, 25, 26], or a laser induced seeding [27, 28].

There has been a great deal of efforts to improve or even eliminate that harsh treatment since the 1990s, through various surface modification strategies. For instance, recently, Garcia *et al*. [10] introduced poly (acrylic acid) covalent grafting, with which copper was electroless plated onto the acrylonitrile-butadiene-styrene (ABS). Tengsuwan and Ohshima [29] introduced a polypropylene-polyethyleneoxide copolymer to increase the hydrophilicity of polypropylene (PP) and supercritical carbon dioxide to improve infusion of the catalyst; therefore, Ni metal layer was successfully formed onto PP substrates. Nakagawa *et al*. [30] introduced ionic surfactants, rendering an electrostatic attraction of catalyst onto the substrate; thus a selective Ni-P electroless plating was implemented.

Apart from all these modification strategies, hydrophobic interaction is another promising methodology recognized by researchers [31]. Hydrophobic interaction is the ubiquitous phenomena that in aqueous solution, non-polar substances exhibits a "water-repulsive" behavior and tends to aggregate with each other [32, 33]. These non-polar substances usually contain hydrophobic groups, which are lack of affinity with water, such as long chain of carbons [33].

The adsorption of polyelectrolyte multilayers on polymer surfaces via hydrophobic interactions was first reported by Delcorte et al. [34]. In their work, poly (styrenesulfonate) and poly (choline methacrylate) were alternately deposited and formed a multilayer system onto various noncharged polymer surfaces. They also found the use of hydrophobically modified poly (choline methacrylate) improved the multilayer quality on hydrophobic substrates. Years later, Park and Hammond [35] identified the hydrophobic interaction between poly (allylamine hydrochloride) (PAH) with hydrophobic polymers (Teflon-AF, octadecyltrichlorosilane, and poly (dimethylsiloxane)). PAH is a hydrophobic weak polyelectrolyte, positively charged when it is protonated [35]. The hydrophobic nature of the PAH backbone can induce hydrophobic

interactions with other hydrophobic substances in aqueous solution [36]. Since discovered, the methodology has been applied in many bio-pharmaceutical aspects, including drug delivery [37, 38], protein adsorption and binding [39], and manipulation of bio-signaling [40].

In this work, we demonstrate a facile method of electroless Ni deposition on various hydrophobic polymer substrates. By making use of the hydrophobic interaction of PAH, the methodology eliminates the need for harsh and toxic treatment of the substrate. A thickness up to ~2 μm of Ni deposition was formed.

4.2 Experimental sections

4.2.1 Materials and equipment

Various hydrophobic polymer thin sheets, including low density polyethylene (LDPE, semi-clear white), high density polyethylene (HDPE, semi-clear white), polypropylene (PP, semi-clear white) and polystyrene (PS, opaque white) are thin sheets (30.5 mm × 30.5 mm × 0.16 mm, Mcmaster-Carr, Santa Fe Springs, CA) when purchased. The film sheets were merely rinsed with detergent when received and afterwards dried, stored in a cabinet at room temperature. No chemical treatment was applied. In the experiment, all polymer sheets were cut into a rectangular shape (2.54 mm × 50.8 mm). Polyethylene (PE) pellets were kindly provided by Baker Hughes Inc. (Houston, TX), with a nominal average diameter around 500 μm. These pellets were used as it is. Non-functionalized PS microspheres (w/v 2.5%) with a monodispersed diameter of 10 μm were purchase from Polysciences, Inc. (Warrington, PA). These samples were stored in a cold room at 4 °C and diluted 10 times before use.

A weak positively charged polyelectrolyte, Poly(allylamine hydrochloride), or PAH (average Mw ~58,000, Sigma-Aldrich, St. Louis, MO) solution was prepared at 1 g/L. The pH

was adjusted to 6.5 using 1 M sodium hydroxide (NaOH, Fisher Scientific, Pittsburgh, PA), unless otherwise noted.

The electroless nickel (Ni) plating catalyst, sodium tetrachloropalladate (II) ($Na_2[PdCl_4]$, 98 %, Sigma-Aldrich) was prepared at 5 mM in DI water. The pH was adjusted to 2 using 1 M hydrochloric acid (HCl, Fisher Scientific). It will be referred as "the Pd catalyst" in this chapter. Electroless Ni plating bath contained 4 g nickel sulfate (II) (99 %, Sigma-Aldrich), 2 g sodium citrate (≥ 97 %, Sigma-Aldrich), 0.2 Dimethylamine borane (DMAB, 97 %, Sigma-Aldrich), lactic acid (85 %, Sigma-Aldrich) in 100 mL DI water. The pH was adjusted to 6.5 using ammonium hydroxide (NH_4OH, 28 % - 30 %, Fisher Scientific). A more detailed experimental description can be found in our previous work [15].

Deionized (DI) water supplied by a Barnstead Nanopure-UV 4 stage purifier (Barnstead International Inc., Dubuque, Iowa), equipped with a UV source and final 0.2 μm filter with a resistance ≥ 18.0 MΩ·cm was used for all aqueous solution preparation and washing.

4.2.2 Ni electroless deposition

In this study, polymer thin sheets were sequentially interacted with the PAH solution for 30 min, the Pd catalyst for 15 min, and the Ni electroplating bath for 1 h, with a rinse after each step with DI water. A clamp was used to fix the sample. However, as for polymer pellets and spheres, the fixation and collection of samples became more complicated because of their size and properties (e.g., density). For PE pellets, since they have lower density (0.91 - 0.95 g/cm^3) than water, they float on the surface of an aqueous solution and can only interact with the aqueous solution partially. To overcome that problem, for each step, the PE pellets were sent into

a 15 mL centrifuge tube with the designated chemical solution and rotated in a tube rotator (Krackeler Scientific Inc., Albany, NY) at ~30 revolutions per minute (rpm) for the same amount of time. This procedure can ensure that the PE pellets fully interact with the designated chemicals and the floating issue can be addressed. After each step, PE pellets were vacuum filtered and washed on a whatman filter paper #1 (Fisher Scientific, retention particle size ~11 μm). For PS microspheres, since their density (1.06 – 1.12 g/cm^3) is higher than water, the tube rotator was not used. Amicon Ultra-15 centrifugal tubes (Millipore Co., Billerica, MA) were used for all steps for high recovery of the samples. A centrifuge and at 6000 rpm for 15 min followed by washing with DI water was applied after each step. After these three steps (PAH, the Pd catalyst and Ni electroless plating), all samples were air dried and stored in a desiccator.

4.2.3 Copper (Cu) electro-deposition

The Ni coated PS thin sheets were further coated with Cu using the electro-deposition. The copper electro-deposition system was set up as follows. A glass container (World Kitchen LLC, Greencastle, PA) was placed on top of a stirrer/hot plate (model no. 11-300-49SHP, ThermoFisher Scientific, Barrington, IL), with a thermocouple placed into a non-cyanide electrolyte (Uyemura International Co., Ontario, CA) for temperature control. To get rid of the directional effect of the anode sheet, a rectangular niobium mesh (Larry King Co., Rosedale, NY) was used. The PS thin sheet sample was placed in the middle of the mesh, and also in parallel with the long dimension of the anode mesh. Meanwhile, each side of the mesh was attached with a copper anode (Mcmaster-Carr, Santa Fe Springs, CA). An electrolyte of 40 g/L Cu was used at 65 °C and a pH of 7.5. A potentiostat (Allied Plating Supplied, Inc., Hialeah, FL) with a maximum output of 15 amperes and 12 volts was applied for this study. A stirring bar was

applied throughout the entire deposition process at 180 rpm. The current density was maintained at approximately 10 mA/cm^2 until the desired amount of deposition was achieved. A detailed description and illustration of the Cu electro-deposition system can be found in the previous chapter.

4.2.4 Scanning electron microscopy (SEM) imaging

The Ni coated samples were evaluated through scanning electron microscope (SEM) imaging using a Zeiss EVO LS 25 variable pressure SEM. The microscope is equipped with an energy dispersive x-ray (EDX) detector to determine atomic compositions. Colors with distinct contrast were deliberately chosen to label the present element in the designated area. Before imaging, polymer thin sheets were sputter coated with gold (Au) under vacuum (Leica EM MED020, Buffalo Grove, IL), until a 5 nm coating thickness was achieved.

The dried samples were sent into the chamber without further conditioning, and a high vacuum mode (less than 1×10^{-2} Pa) was selected during the imaging. Unless otherwise stated, all SEM images were taken under high vacuum mode at a 16 kV accelerating voltage and a 25 mm working distance. The EDX studies were performed at a 16 kV accelerating voltage and a 9 mm working distance.

4.2.5 Kinetic study of Ni deposition on polymers

Ni coated HDPE and PS thin polymer sheets were recorded with the mass and morphology change, as a function of coating time. At the designated time window, each specimen was pictured with a digital camera. Before each time the sample was weighed, it was dried with N_2 gas at room temperature.

4.2.6 Optical microscopy imaging

Samples were also observed using a Keyence optical microscope VHX-600 (Elmwood Park, NJ) with magnification ranging from 10× to 1000×. For all images acquired with the optical microscope, a reflection mode was selected unless otherwise noted.

4.3 Results and discussions

4.3.1 Visualization and microscopic analysis of polymer thin sheets

In this section, four different neutral hydrophobic polymers were selected as substrates for Ni electroless deposition. Three main steps were included in the following order: 1) an immersion in the PAH solution; 2) an immersion in the Pd catalyst solution; 3) an immersion in the Ni electroless plating bath.

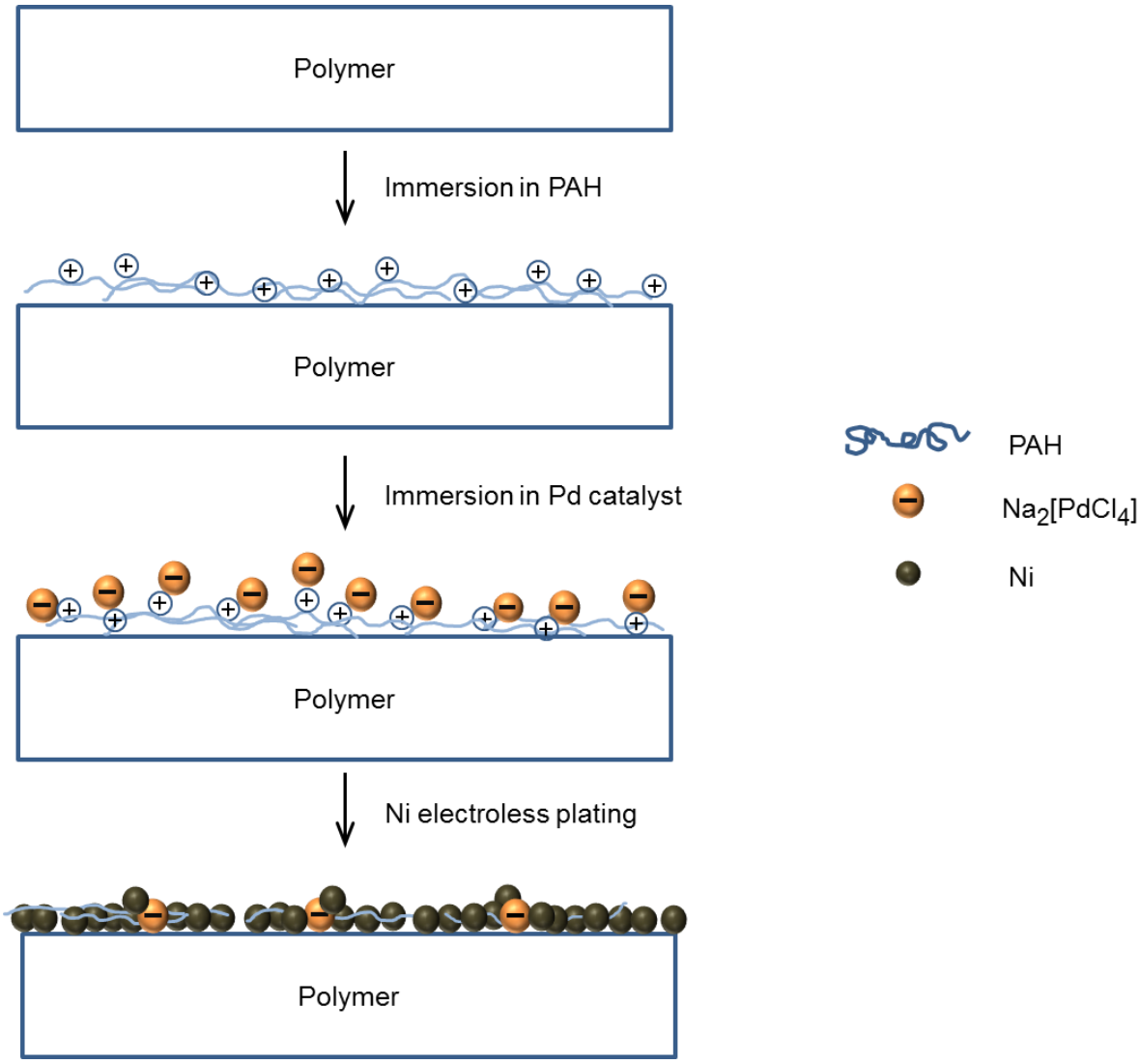

Figure 4.1 Overall scheme of Ni electroless deposition on a hydrophobic polymer thin sheet

Figure 4.1 shows an illustrative scheme of Ni electroless deposition on neutral hydrophobic thin polymer sheets. Firstly, the application of PAH induced hydrophobic interactions with the designated polymer surface, therefore, the PAH was adsorbed onto the polymer surface. As briefly mentioned in section 4.1, the long carbon chain backbones that exist in both the PAH and the polymer substrate are hydrophobic, therefore, exhibiting a repulsive nature to the aqueous solution and tend to assemble each other [32, 33]. It should be noted that even hydrophobic interaction is not a strong interaction, but stronger than van der Waals interactions and hydrogen bonds in aqueous environment [32]. A variety of conformation of PAH on hydrophobic surfaces was investigated in the previous studies [35, 41]. It should be mentioned that when the PAH chains are fully charged, a stretched conformation will be obtained due to the electrostatic forces between charged groups on the chains [35]. The weak polyelectrolyte nature of PAH has a reversible equilibrium of dissociation, which is largely dependent on its local pH and ionization. At a pH lower than p*K*a value (p*K*a of PAH is 8.7 [42]), PAH is primarily protonated, and therefore, spread on to the substrate surface [35]. An increasing ionic strength will give rise to a decreased layer thickness because of the spreading of the PAH chains to the surface [35, 43]. At the same time, because of the ionization the PAH chains are exhibiting a certain degree of "coiling conformation" [35], which is shown in Figure 4.1. The "coiling conformation" results in a random distribution of charged group, both on the substrate surface and throughout the thickness of the adsorbed PAH layer. Secondly, a catalyst deposition was achieved by immersing PAH modified substrate into the Pd catalyst solution, enabling an electrostatic interaction between the pronated PAH (positively charged) and the Pd catalyst (negatively charged). The electrostatic interaction between catalysts with different charges and the corresponding polyelectrolytes has been thoroughly investigated in our previous

studies [15, 44, 45]. In this work, because of the distribution of the positive charges, catalyst is attracted and catalytic sites are created throughout the PAH layer thickness too. Finally, when the designated polymer thin sheet was submerged into the Ni electroless plating bath, the redox reaction of Ni cations to nonvalent Ni occurred at the corresponding catalytic sites (where catalyst is present) and forms a thin layer of Ni coating.

A control experiment was performed with exclusion of the first step, in which PAH was adsorbed onto the designated polymer surfaces. Figure 4.2 shows a systematic comparison of designated polymers before and after Ni deposition. Without the inclusion of PAH, all designated polymers were not deposited with Ni at all. The previous research [45] has shown that, with the same Ni electroless plating bath, no Ni coating was formed without the Pd catalyst. Combined with that result, we were able to conclude that Ni coating was not formed on the polymer surface due to the fact that no catalyst was attached. However, with the inclusion of PAH, Ni was successfully formed on all the designated polymer surfaces.

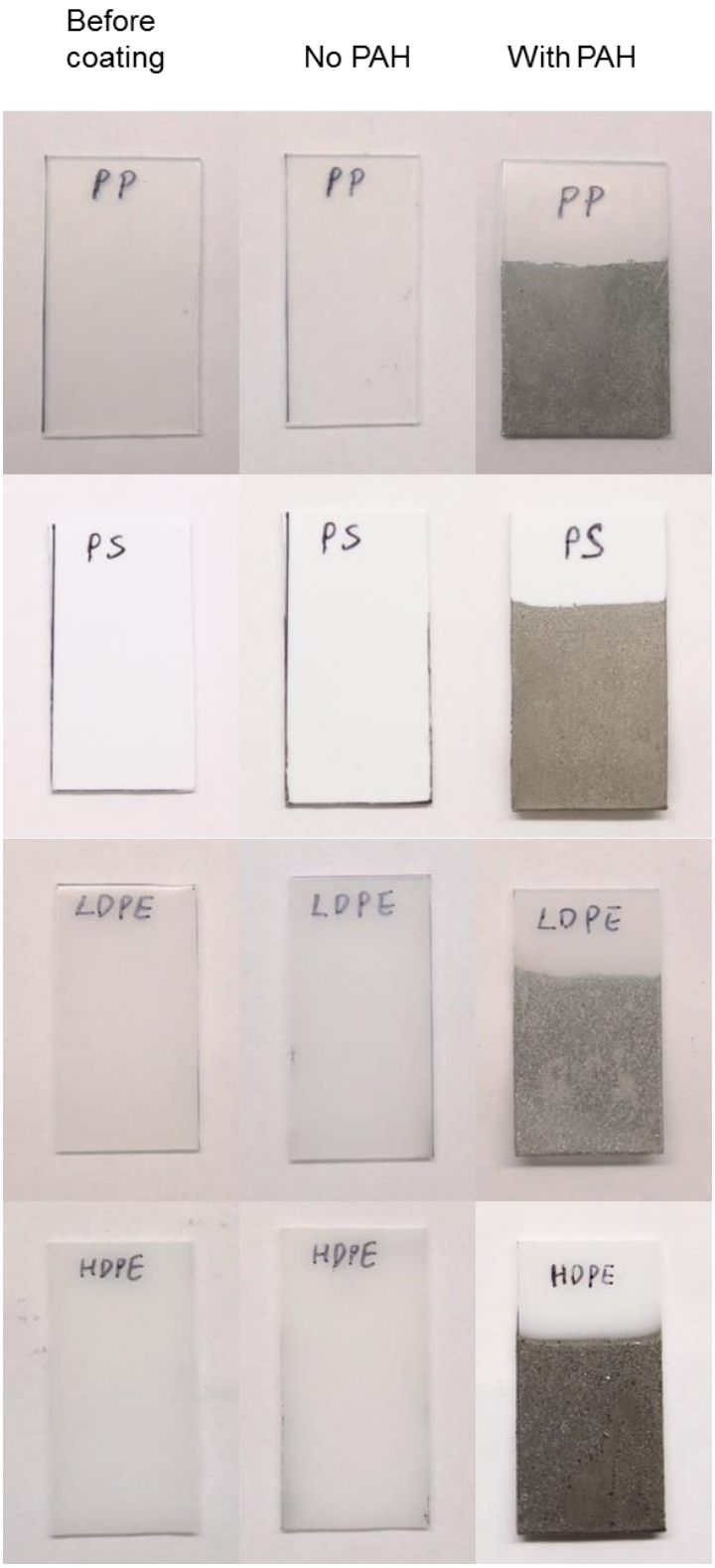

Figure 4.2 Visualization and comparison of Ni coating on various hydrophobic polymer thin sheets (LDPE, HDPE, PP, PS). Non-PAH modified polymer sheets were not able to form Ni coating.

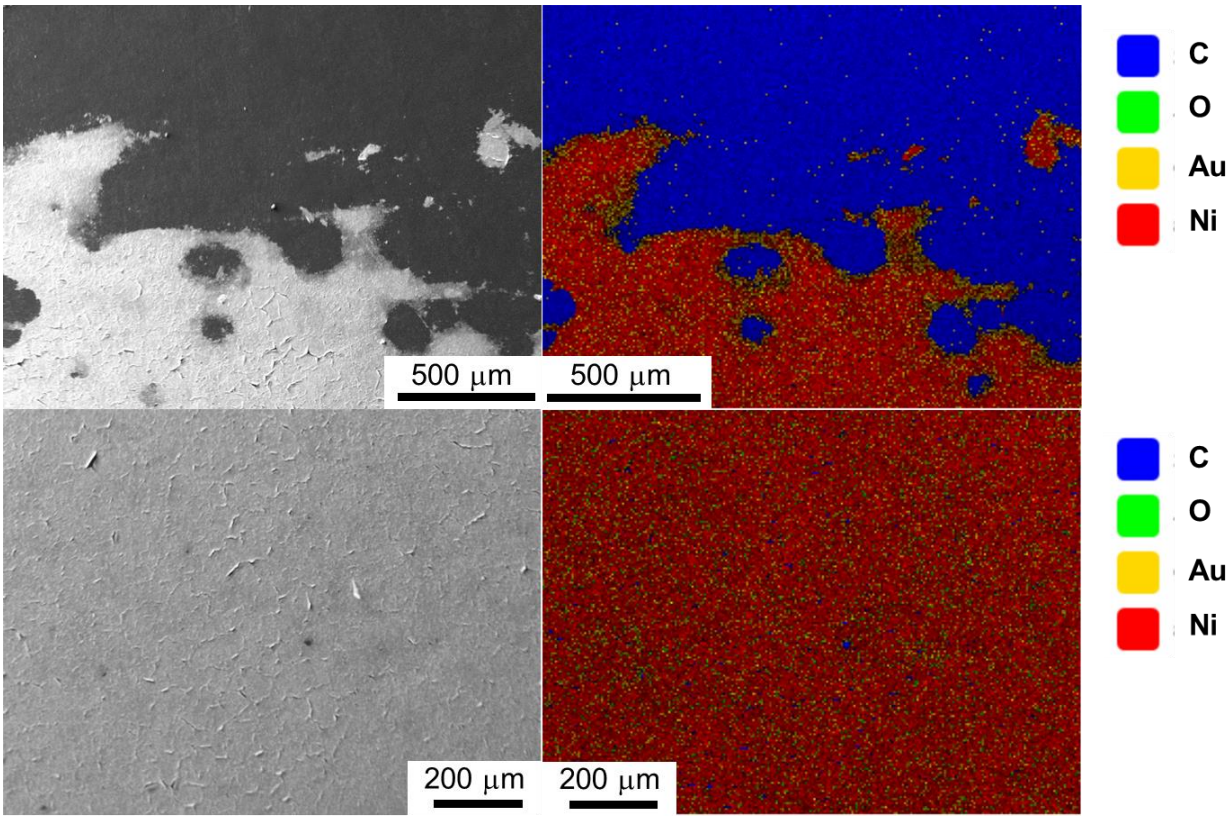

Figure 4.3 Visualization of Ni coating on a PP polymer thin sheet. Upper left is a SEM image at the edge of Ni coating; upper right is the corresponding EDX elemental mapping (60 wt % of C, 11 wt % of Au, 29 wt % of Ni); lower left is a SEM image at the main coating body; lower right is the corresponding EDX elemental mapping (6 wt % of C, 5 wt % of O, 18 wt % of Au, 71 wt % of Ni).

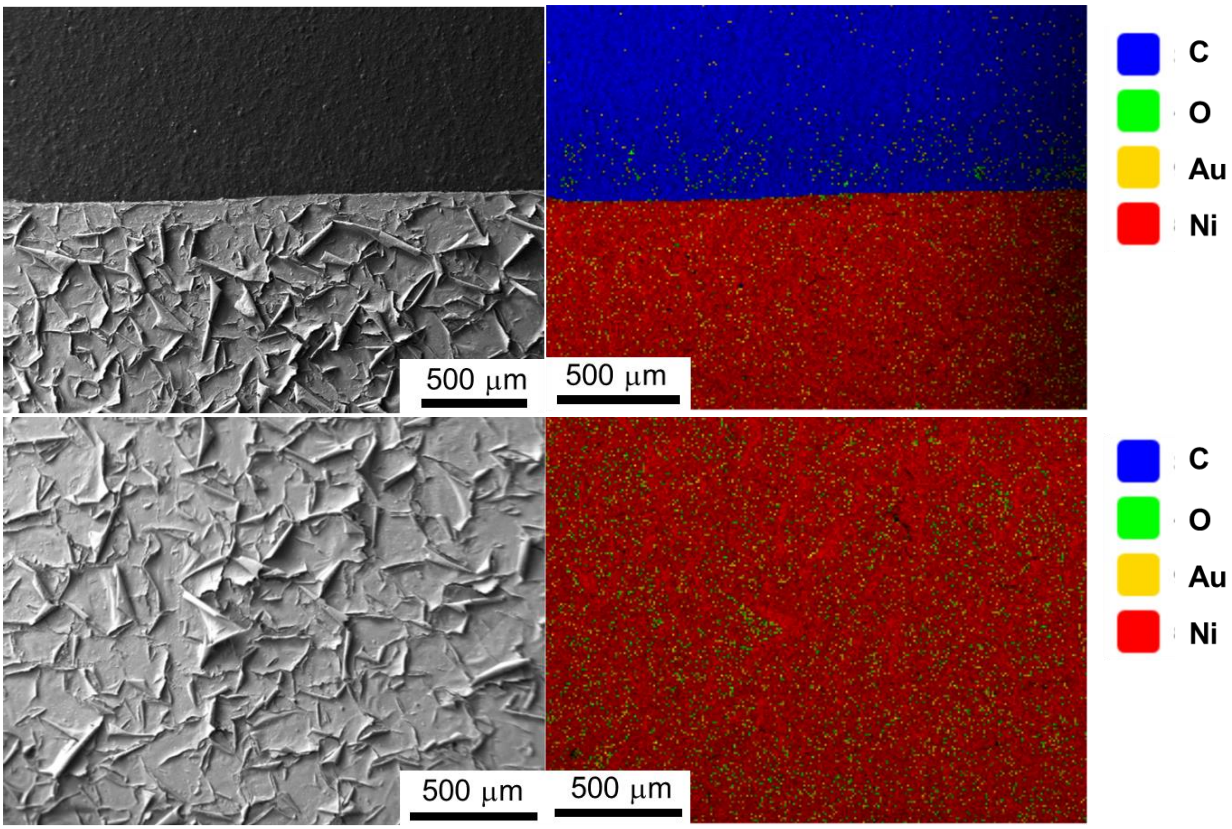

Figure 4.4 Visualization of Ni coating on a PS polymer thin sheet. Upper left is a SEM image at the edge of Ni coating; upper right is the corresponding EDX elemental mapping (44 wt % of C, 3 wt % of O, 8 wt % of Au, 45 wt % of Ni); lower left is a SEM image at the main coating body; lower right is the corresponding EDX elemental mapping (4 wt % of O, 12 wt % of Au, 84 wt % of Ni).

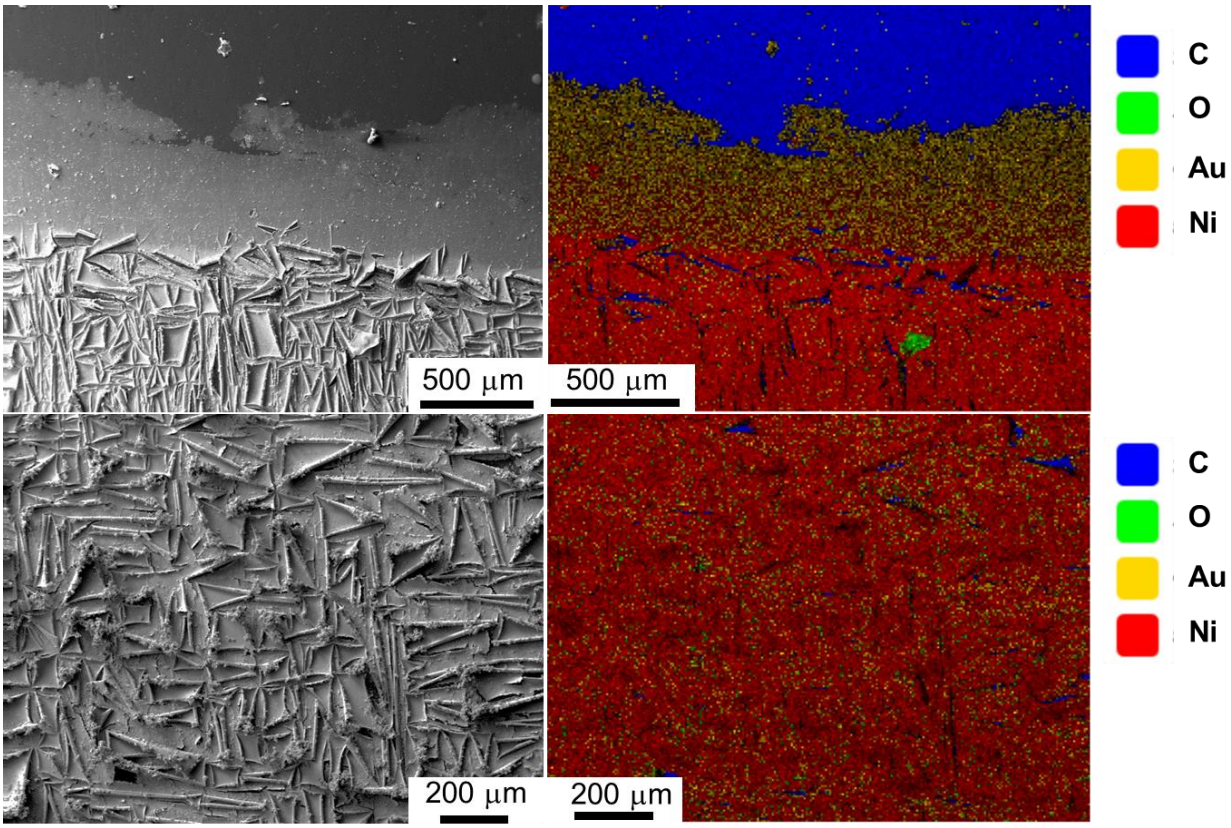

Figure 4.5 Visualization of Ni coating on a HDPE polymer thin sheet. Upper left is a SEM image at the edge of Ni coating; upper right is the corresponding EDX elemental mapping (37 wt % of C, 6 wt % of O, 9 wt % of Au, 48 wt % of Ni); lower left is a SEM image at the main coating body; lower right is the corresponding EDX elemental mapping (3 wt % of C, 4 wt % of O, 9 wt % of Au, 84 wt % of Ni).

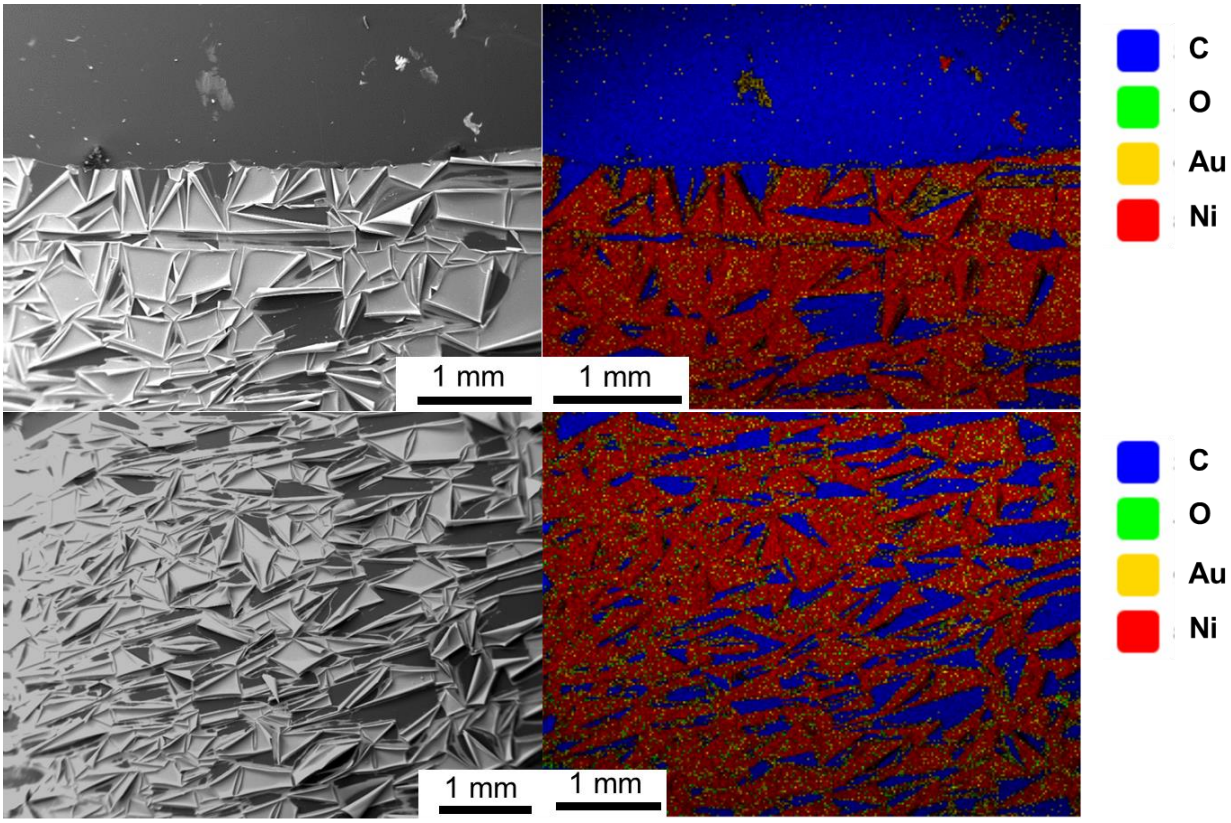

Figure 4.6 Visualization of Ni coating on a LDPE polymer thin sheet. Upper left is a SEM image at the edge of Ni coating; upper right is the corresponding EDX elemental mapping (51 wt % of C, 7 wt % of Au, 42 wt % of Ni); lower left is a SEM image at the main coating body; lower right is the corresponding EDX elemental mapping (28 wt % of C, 3 wt % of O, 8 wt % of Au, 61 wt % of Ni).

The morphologies of Ni coating on the different polymer surfaces were observed by SEM. The Ni depositions on all the designated polymer thin sheets were achieved. As shown in Figures 4.3-4.6, representative images at the coating/polymer edge and at the main coating body are shown, for each designated polymer thin sheet. An EDX elemental mapping investigation was performed and presented next to the corresponded SEM image. Results showed different morphologies of Ni coatings on different polymer substrates. The Ni coating on PP appeared smooth, with minimal defects among all the substrates. The Ni coating on PS exhibited a rough surface, with an overlapped Ni flake-like morphology. The excessive nucleation and growth of Ni coating caused a full coverage on the polymer surface. The Ni coatings on HDPE showed a

similar flake-like morphology, but with less overlap. The coating had a few delaminated areas both at the coating edge and the coating main body. The Ni coating on LDPE showed inferior quality, with a large portion of delamination (interfacial fracture) on the surface. As a result, a fair amount of the LDPE was uncovered with Ni.

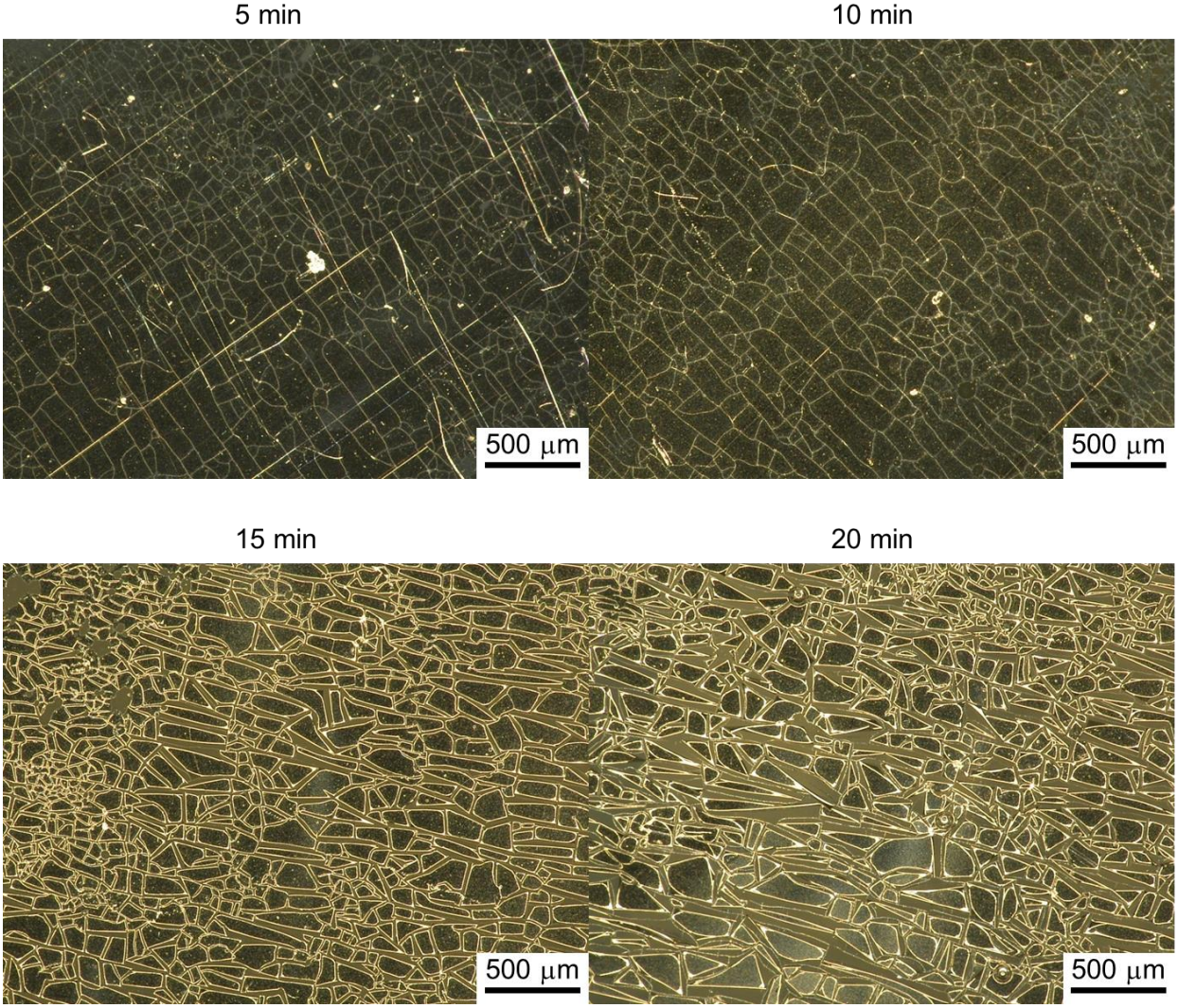

Figure 4.7 The evolution of Ni coating morphologies on the LDPE surfaces.

To further investigate the delamination phenomena, as shown in Figure 4.7, the morphological study of the Ni coating on LDPE as a function of time was conducted. In order to eliminate the effect of drying, the Ni coated LDPE samples were subjected to optical microscopy

imaging immediately after the coating. As suggested by the Figure 4.7, Ni coating formed a connected thin layer up to 10 min of coating. The morphology at 15 min showed that Ni coating was partially disconnected, indicating that the delamination of coating occurred between 10 min and 15 min of coating. The morphology at 20 min exhibited even more delamination. It should be noted that the delamination occurs widely in the coating industry [46-49]. Although many mechanisms have been proposed, generally it is considered that the delamination is due to the internal mechanical/ thermal stress buildup during the coating [49, 50]. Therefore, to prevent delamination, a stress relieve step is needed. One of the efficient ways to relieve stress, as previously reported by our group, is to incorporate nanoparticles [49, 51] at the interface to deflect and break up the internal stresses.

The delamination could be partially due to different mechanisms of Ni formation on the designate polymer surfaces, and the weak adhesion between the coating film and the corresponding substrate. The adhesion between the Ni coating and polymer substrates is not meant to be strong because the adsorption of PAH on to polymer surfaces is not a strong interaction. It was reported that the hydrophobic interaction of PAH was used to transfer multilayer from the stamp when it was initially exploited since the hydrophobic interaction was weaker than the electrostatic forces [52, 53]. Even though, the weak adhesion between coating and the substrate is considered detrimental in many actual practices, people have applied those weakly bonded material structures as intermediate products for composite fabrications [49], and pattern transfer [52] as mentioned earlier. However, if a stronger adhesion is desired, it can be achieved by introducing chemical bonds (e.g. cross-linking), or a careful optimization of the Ni electroless plating bath, polyelectrolyte and the coating procedure.

The coverage of the Ni coating on polymer thin sheets is also of interest. According to the EDX mapping, the PP thin sheets exhibited minimal uncovered area. The PS thin sheet exhibited a superior Ni coating coverage that the polymer was no longer detected (0 % of C). The HDPE thin sheets exhibited a similar coverage of Ni coating to PP. The Ni on the LDPE exhibited a large portion of the uncoated area in the main coating body. By comparing the weight percentage of Ni and C (polymer), the percentage of Ni coverage on those four polymer thin sheets can be ranked in the descending order as follows: PS > PP ≈ HDPE > LDPE.

4.3.2 Visualization and microscopic analysis of polymer pellets and spheres

In this section, all the substrates subjected to the Ni coating follows the same process route as the polymer thin sheets. Figure 4.8 shows the illustrative scheme of the Ni electroless deposition on the neutral hydrophobic polymer pellets and spheres. The mechanism for the formation of the Ni coating is the same, other than the geometry and dimension of the substrate.

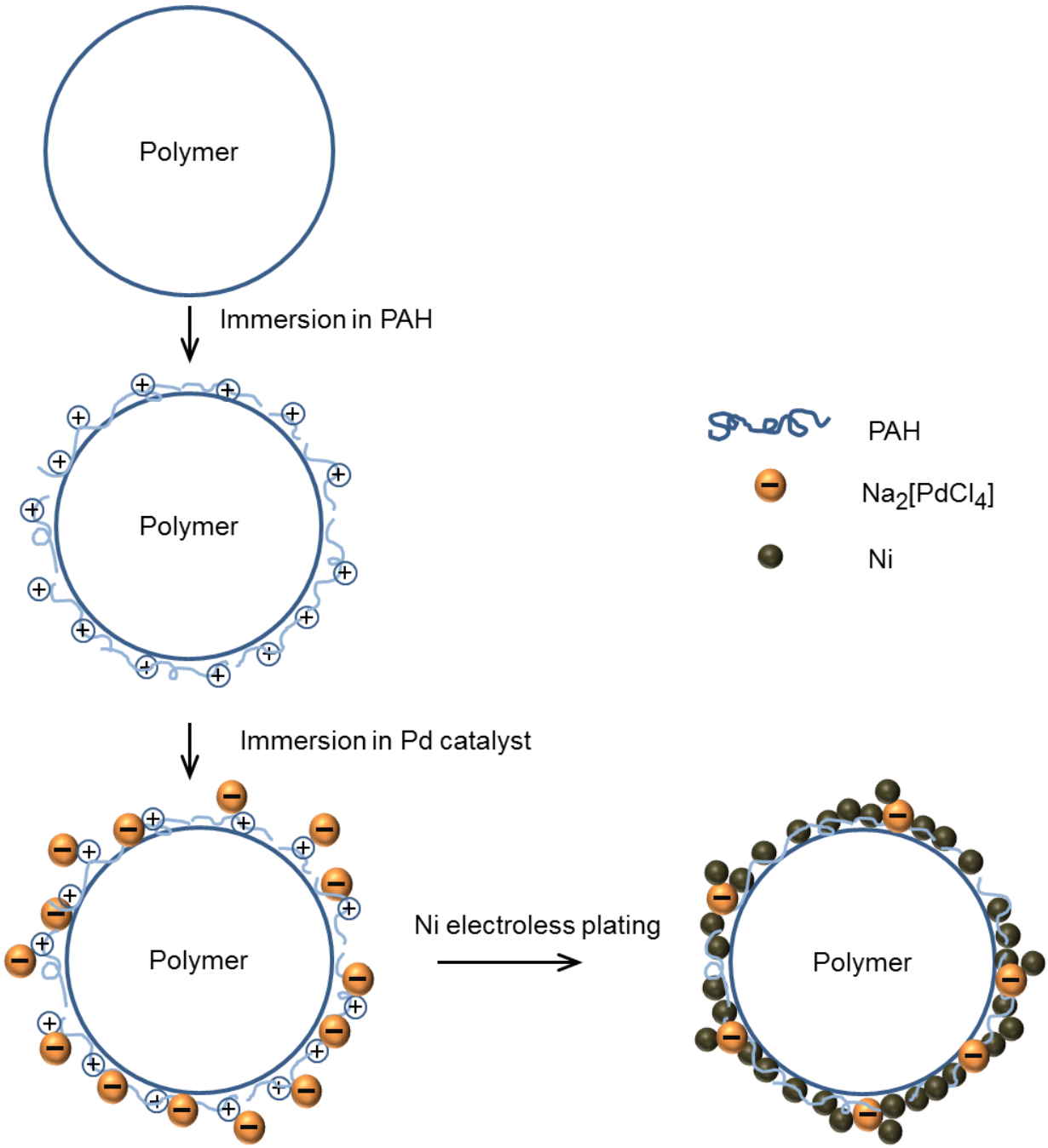

Figure 4.8 Overall scheme of the Ni electroless deposition on the hydrophobic polymer pellet/sphere.

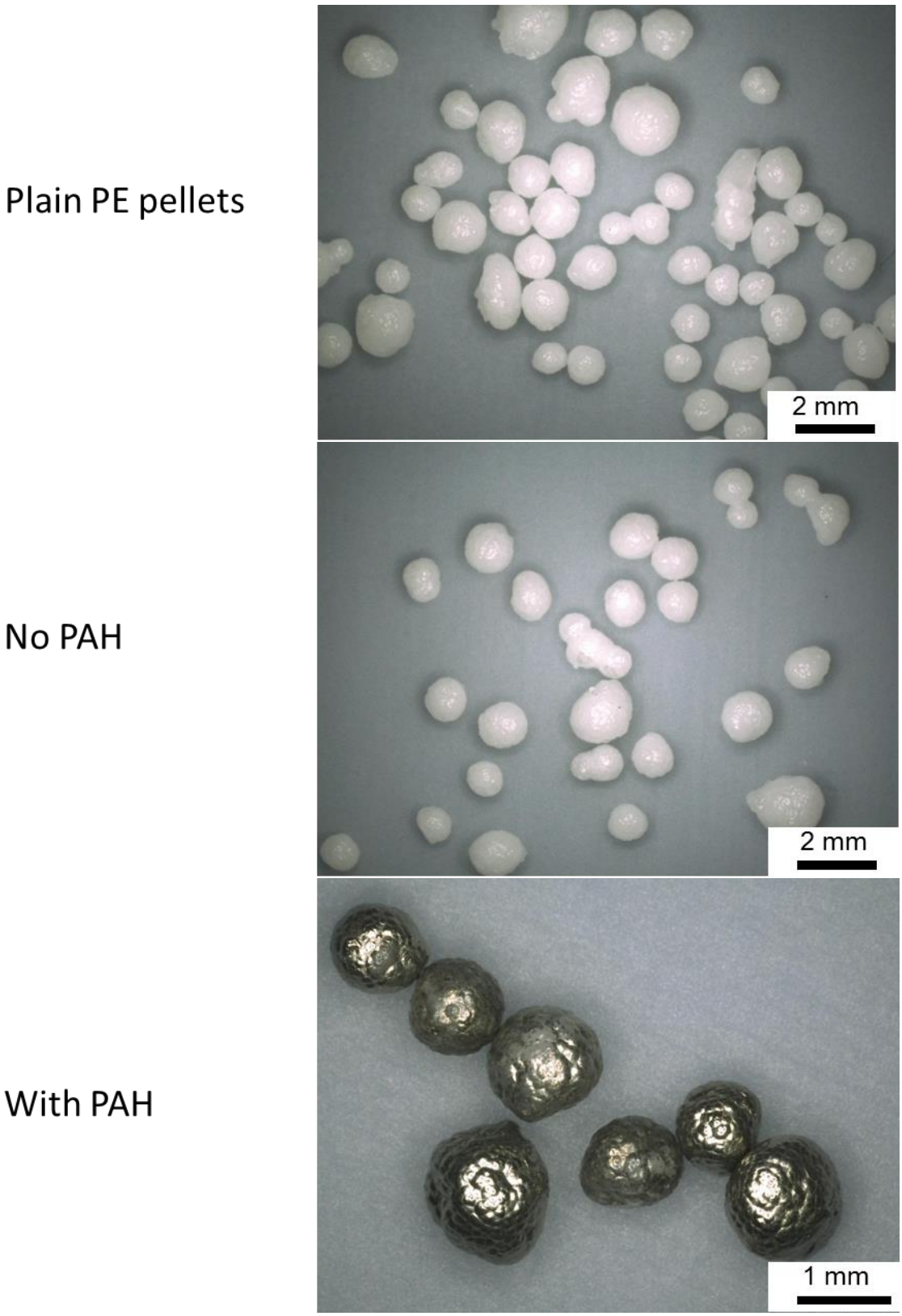

Figure 4.9 Visualization of Ni deposition on PE pellets. Non-PAH modified PE pellets were not able to form Ni coating.

4.3.2.1 Ni deposition on PE pellets

Figure 4.9 exhibits a set of studies of PE pellets before and after the Ni deposition. A control experiment was also performed with the exclusion of step 1 (PAH dipping). Without the inclusion of PAH, PE pellets remained uncoated. With the inclusion of PAH, PE pellets were successfully deposited with Ni, even though the Ni coverage is not perfect on some of the pellets.

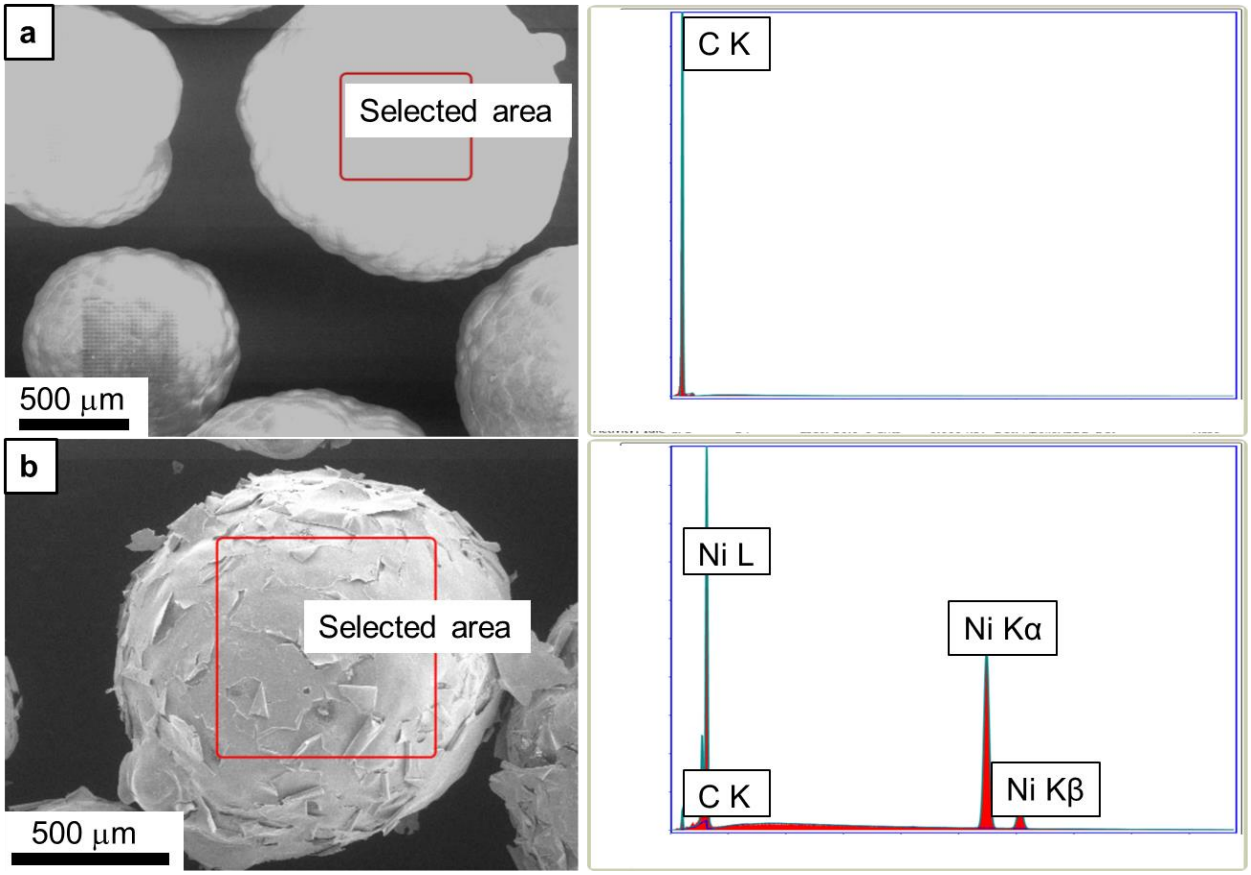

Figure 4.10 SEM images of a) uncoated PE pellets; b) a coated PE pellet. The corresponded diagram next to each image shows the element signal of a selected area designated in the SEM image.

The morphologies of the Ni coated PE pellets were observed by SEM (see Figure 4.10). The coating looks similar to that on the polymer thin sheets. Overlapped flake-like Ni coatings were formed on the PE pellets. A comparison before and after the Ni electroless plating was

made with EDX. With the help of EDX, the area scanning proved formation of Ni on the coated sample (Figure 4.10 (b)); whereas no Ni peak was observed in the uncoated one (Figure 4.10 (a)).

4.3.2.2 Ni deposition on PS microspheres

PS microspheres are commercially provided with specific surface charge functionalities [54], ideally negative (e.g. carboxylate-modified PS), positive (e.g. amine-modified PS) and neutral (e.g. plain PS), but in reality, they can be deviated because of the fabrication methodology. Emulsion polymerization [55, 56] process is usually employed for the fabrication of monodispersed PS, since this method can precisely control the particle size with a narrow polydispersity. This methodology includes: 1) the formation of micelles from surfactant molecules; 2) the addition of monomers (styrene), entering of monomers into micelles; 3) the addition of an initiator to induce polymerization; 4) the polymerization termination by sulfate ions from the initiator which remain at the sphere surface. This mechanism gives rise to the aggregation of anions at the surface, making the surface with charges (negative), even without functional group. Excessive amount of surfactant will largely increase surface charges of the sample. Actually the surface charge of the plain PS purchased from polysciences (Warrington, PA) was tested and gave the value of -20.24 ± 1.09. The variation may exist among different batches, but still, that value is considered mildly negative.

With that in mind, polystyrene microspheres were also Ni electroless plated in this work. The same coating strategy was used. A control study showed no Ni deposition was observed when PAH-step was excluded. Because there is no hydrophobic interaction, also PS surface and the Pd catalyst are both negatively charged, making the Pd catalyst impossible to be attached. However, if the PS has a positive surface charge, the Pd catalyst will be adsorbed by electrostatic

interactions. A similar work has been done by previous researchers [15]. But when the PAH-step was included, the Ni coating was formed (see Figure 4.11). However, the morphology of Ni coated PS microspheres looks different from the coating formed on other samples (polymer thin sheets, PE pellets). Instead of Ni thin films, small size Ni grains were formed on the PS microspheres. It could be ascribed to the fact that the electrostatic and hydrophobic interactions play together, attracting PAH in different conformations and therefore forming Ni deposition in a different way.

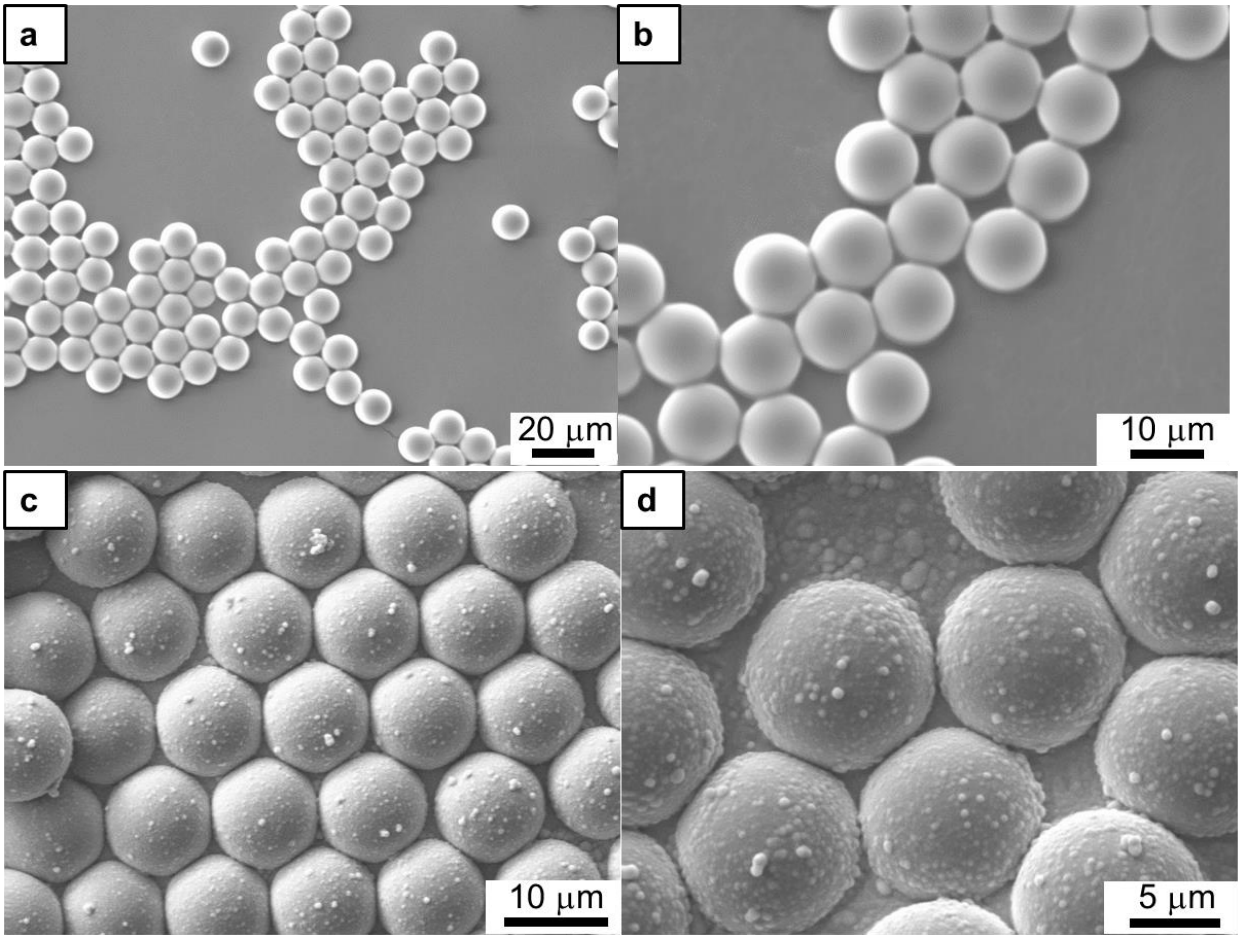

Figure 4.11 SEM images of a) PS microspheres before coating; b) non-PAH modified PS microspheres after Ni deposition; c) and d) PAH modified PS microspheres after Ni deposition.

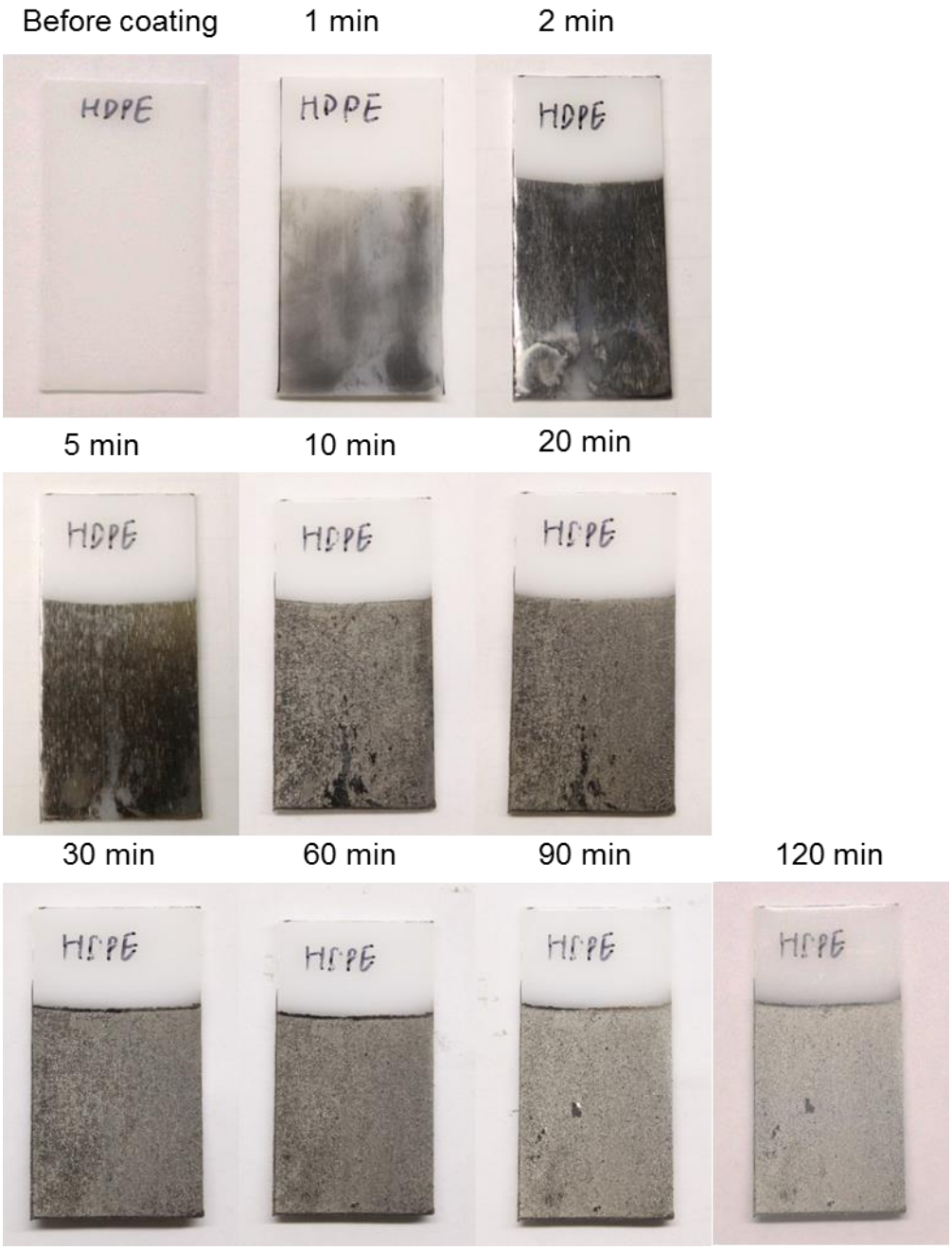

Figure 4.12 A morphological change of HDPE thin sheet, during Ni electroless deposition.

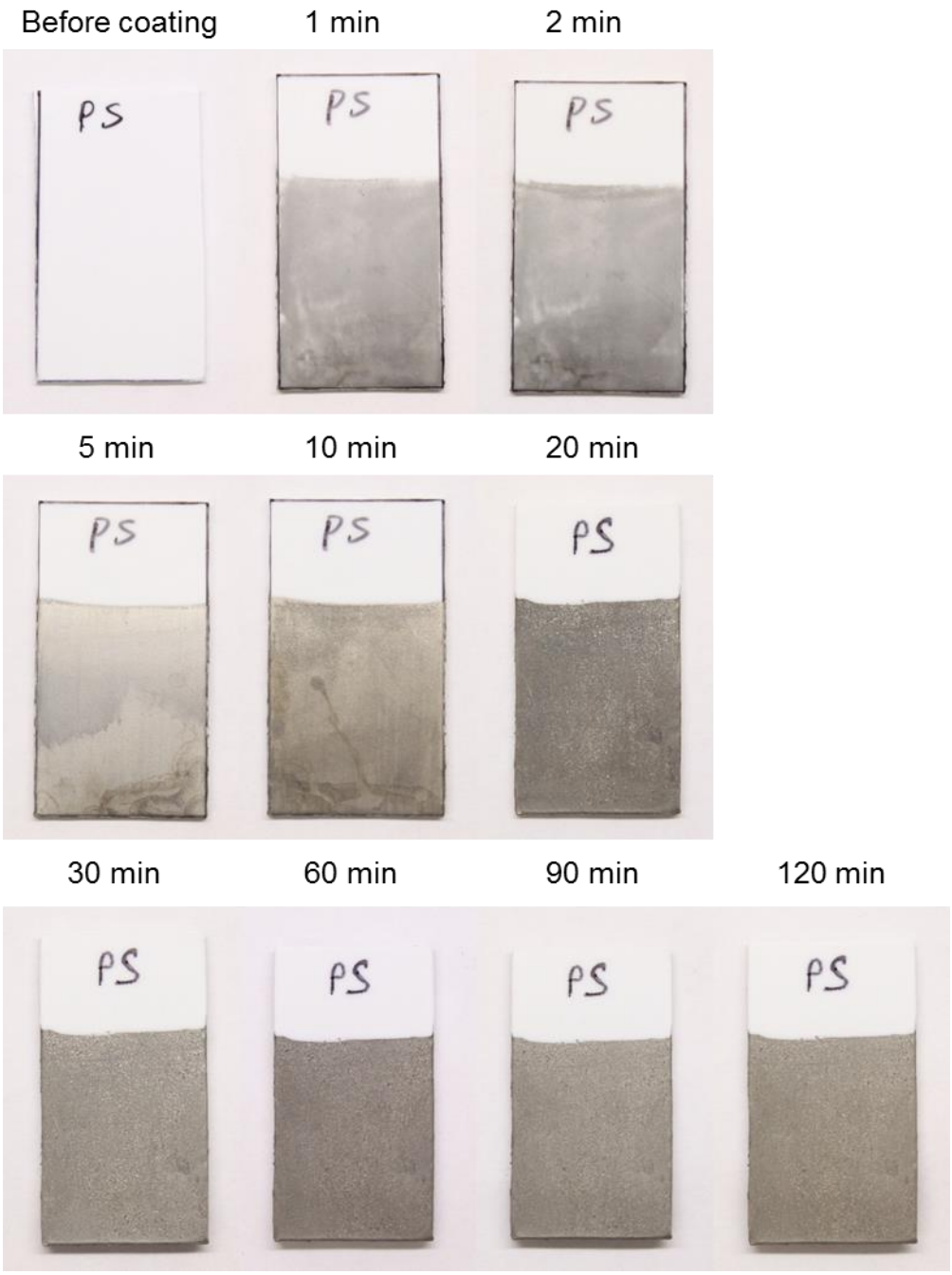

Figure 4.13 A morphological change of PS thin sheet, during the Ni electroless deposition.

4.3.3 Kinetic study of Ni deposition

Figures 4.12 and 4.13 demonstrate gradual morphology changes along with coating time on the HDPE thin sheet and the PS thin sheet, respectively. The depositions of Ni on the Pd catalyst-seeded HDPE and PS thin sheets are almost instantaneous. Both substrates showed the

Ni coating at the 1st min of coating. In the first 10 min of coating, both substrates showed a severe morphological change, due to the Ni coating formation. It was also noted that for both polymers, after 30 min of coating, the morphology of them remain almost unchanged. It is probably due to the fact that the horizontal coverage of Ni reaches plateau in that time frame, and the vertical thickness growth became dominant, which will not result in any change in its outlook.

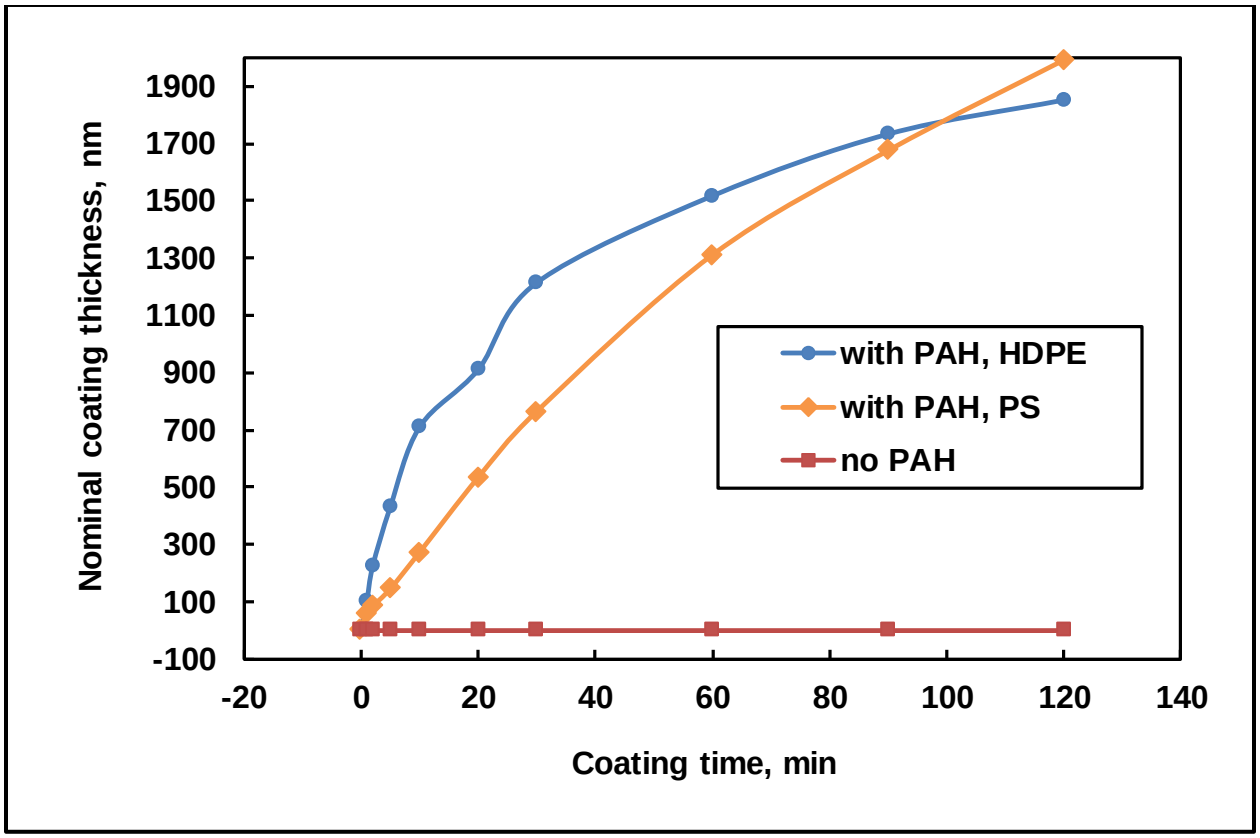

Figure 4.14 Kinetic studies and comparison of Ni electroless deposition on HDPE and PS, respectively. A nominal thickness gain over coating time was plotted.

The thickness gain over time provided more details. The nominal thickness gains of two polymer thin sheets were plotted against coating time as shown in Figure 4.14. The thickness gains for non-PAH modified HDPE and PS remained zero for 2 hours of coating. The nominal thickness gain was calculated by dividing Ni volume gain by the surface area of designated coating area as demonstrated in Equation 4.1.

$$T = \frac{\Delta m}{\rho[2L_d(w+h)+wh]} \quad \text{(Equation 4.1)}$$

where, T denotes the coating thickness, Δm denotes mass gain in each designated time window, ρ denotes the density of the coated material (for Ni it is 8.91 g cm^{-3}), L_d denotes the long dimension of designated coated area, w denotes the width of the polymer sheet, which equals 25.4 mm, h denotes the thickness of the polymer sheet, which equals 1.6 mm. From the curve, over 2 hours of Ni electro-deposition, both substrates gained an approximately 2 μm coating thickness. However, the HDPE substrate showed slower Ni mass gain after 1hour of coating; whereas the PS substrate exhibited a decreasing trend in terms of thickness gain over time after 1 hour, the thickness gain rate was still faster than that of HDPE in that time frame.

4.3.3 Cu electro-deposition on Ni coated polymer

One of the disadvantages of electroless deposition is that, it can only achieve a few microns or even submicron size thickness, even in hours of processing. This limitation can be overcome by an electro-deposition method in which an applied electro-field forces a current flow through an electrochemical cell to cause chemical changes [57]. The electro-deposition can achieve more than a hundred microns coating thickness in hours. As a matter of fact, in practical, in order to electroplate a substrate which is non-conductive, a thin layer of metal induced by electroless plating is usually applied to reinforce the conductivity, allowing the substrate to be electroplated with either homogeneous or heterogeneous materials afterwards [21, 57]. To address the aforementioned issues and to demonstrate the feasibility, Ni coated polymer sheets were electroplated with Cu.

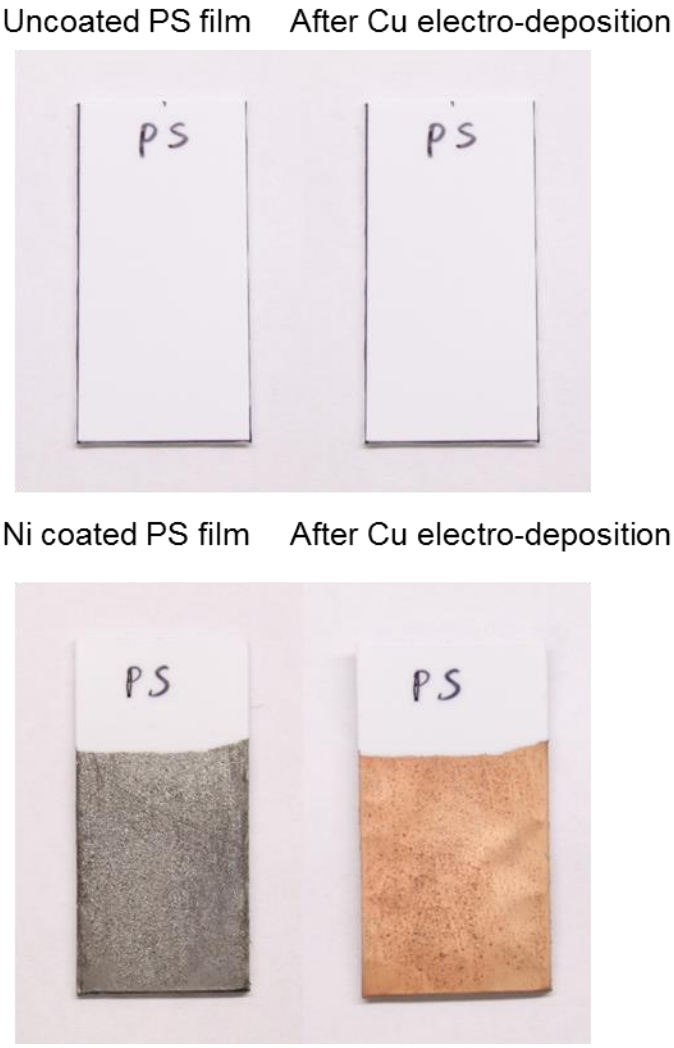

Figure 4.15 Visualization of Cu deposition on Ni coated PS thin sheets, after Cu electro-deposition. Uncoated PS sheets were not able to form Cu coating.

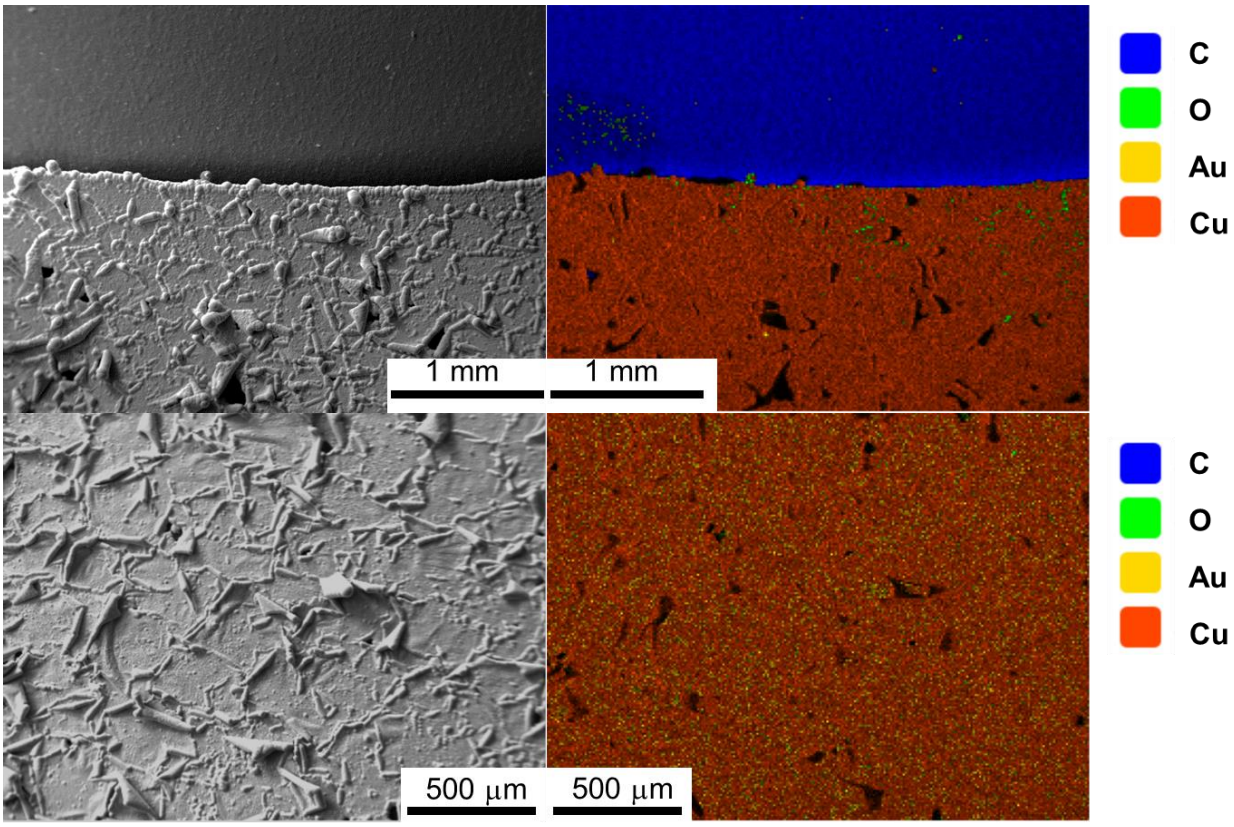

Figure 4.16 Visualization of Cu coating on a Ni coated PS thin sheet, after Cu electro-deposition. Upper left is a SEM image at the edge of Cu coating; upper right is the corresponding EDX elemental mapping (36 wt % of C, 3 wt % of O, 21 wt % of Au, 39 wt % of Ni); lower left is a SEM image at the main coating body; lower right is the corresponding EDX elemental mapping (3 wt % of O, 14 wt % of Au, 82 wt % of Ni).

Again a control experiment was conducted, in which an uncoated PS sheet was electroplated in the same electro-deposition system. As expected, no Cu deposition was achieved, simply because of the non-conductive nature of the PS. On the contrary, a Ni coated PS thin sheet was electroplated in the same system, and Cu deposition was successfully achieved (see Figure 4.15). The Cu deposition was visually reddish-orange. It should be noted that although the whole sheet was immersed in the electrolyte and subjected to electro-deposition, only the Ni coated portion was electrodeposited. Similarly, SEM images and corresponding EDX investigations on the edge of the coating and the main coating body were conducted, as shown in

Figure 4.16. A full coverage of Cu on to the Ni coated PS sheet was observed. Upon certain thickness of Cu deposition, the designated polymer and Ni were not able to be detected.

The following methodology was applied to calculate the nominal coating thickness gain over time. The mass gain fulfills the classic Faraday's law of electrolysis as a function of time, at a constant current [57],

$$\Delta m = \frac{IM}{Fz} \times t \qquad \text{(Equation 4.2)}$$

where, *I* denotes the applied current, *M* denotes the molar mass of deposited metal (for Cu it is 64 g mol^{-1}), *F* denotes Faraday's constant, *z* denotes the valency number of deposited element (for Cu it is 2), *t* denotes time (in second(s)). Equation 4.1 was used to calculate the thickness gain of deposition, except for the denotation of mass gain. Here it represents the mass gain in electro-deposition. If substitute Equation 4.1 with Equation 4.2,

$$T = \frac{IM}{Fz} \times \frac{t}{\rho[2L_d(w+h)+wh]} \qquad \text{(Equation 4.3)}$$

thus, a nominal thickness evaluation of Cu electro-deposition as a function of time was obtained. Based on the calculation, an approximately 15 μm coating thickness was gained in 1 hour.

4.4 Conclusions

In this work, a facile methodology for Ni electroless deposition on hydrophobic polymer surfaces was proposed. The hydrophobic interaction between PAH and a large variety of hydrophobic polymer surfaces helped eliminate the need for harsh and/or toxic surface treatment for the catalyst adsorption/immobilization. Various hydrophobic polymers with different geometries and dimension were tested, and Ni was successfully deposited onto all of these

polymer surfaces. Comparisons showed without the PAH, Ni coating was not able to form on any of these hydrophobic polymer surfaces. A thickness of ~2 μm of Ni deposition was obtained in 2 hours. The coating thickness limitation can be addressed by applying a further electro-deposition, even with a heterogeneous metal. The electro-deposition can expedite the thickness growth and extend the metallization of non-conductive materials to many aspects.

REFERENCES

REFERENCES

1. Tran VH, Massardier V, Guyot A. Interactions in metal-polymer-metal interfaces. Polymer 1993;34(15): 3179-3183.

2. Grundmeier G, Stratmann M. Adhesion and de-adhesion mechanisms at polymer/metal interfaces: Mechanistic understanding based on in situ studies of buried interfaces. Annual Review of Materials Research 2005;35: 571-615.

3. Holubar P, Jilek M, Sima M. Present and possible future applications of superhard nanocomposite coatings. Surface & Coatings Technology 2000;133-134: 145-151.

4. Long DP, Blackburn JM, Watkins JJ. Chemical fluid deposition: a hybrid technique for low-temperature metallization. Advanced Materials 2000;12(12): 913-915.

5. Cheng K, Yang M-H, Chiu WWW, Huang C-Y, Chang J, Ying T-F, et al. Ink-jet printing, self-assembled polyelectrolytes, and electroless plating: low cost fabrication of circuits on a flexible substrate at room temperature. Macromolecular Rapid Communications 2005;26(4): 247-264.

6. Chen Y, Liu P. Surface modification of polyethylene by plasma pretreatment and UV-induced graft polymerization for improvement of antithrombogenicity. Journal of Applied Polymer Science 2004;93(5): 2014-2018.

7. Esrom H, Kogelschatz U. Modification of surfaces with new excimer UV sources. Thin Solid Films 1992;218(1-2): 231-246.

8. Hrapovic S, Liu Y, Enright G, Bensebaa F, Luong JHT. New strategy for preparing thin gold films on modified glass surfaces by electroless deposition. Langmuir 2003;19(9): 3958-3965.

9. Esroma H, Seeböcka R, Charbonnierb M, Romandb M. Surface activation of polyimide with dielectric barrier discharge for electroless metal deposition. Surface & Coatings Technology 2000;125(1-3): 19-24.

10. Garcia A, Berthelot T, Viel P, Mesnage A, Jégou P, Nekelson F, et al. ABS polymer electroless plating through a one-step poly(acrylic acid) covalent grafting. Applied Materials & Interfaces 2010;2(4): 1177-1183.

11. Rossnagel SM. Directional and ionized physical vapor deposition for microelectronics applications. Journal of Vacuum Science & Technology B 1998;16(5): 2585-2608.

12. Fix R, Gordon RG, Hoffman DM. Chemical vapor deposition of vanadium, niobium, and tantalum nitride thin films. Chemistry of Materials 1993;5(5): 614-619.

13. Willmott P. Deposition of complex multielemental thin films. Progress in Surface Science 2004;76(6-8): 163-217.

14. Karasawa T, Miyata Y. Electrical and optical properties of indium tin oxide thin films deposited on unheated substrates by d.c. reactive sputtering. Thin Solid Films 1993;223(1): 135-139.

15. Lee I, Hammond PT, Rubner MF. Selective electroless nickel plating of particle arrays on polyelectrolyte multilayers. Chemistry of Materials 2003;15(24): 4583-4589.

16. Wang TC, Chen B, Rubner MF, Cohen RE. Selective electroless nickel plating on polyelectrolyte multilayer platforms. Langmuir 2001;17(21): 6610-6615.

17. Matsumura Y, Enomoto Y, Sugiyama M, Akamatsu K, Nawafune H. Direct metallization of nickel on polymeric template patterns for fabrication of copper circuits on glass substrates. Journal of Materials Chemistry 2008;18(42): 5078-5082.

18. Rohan JF, O'Riordan G, Boardman J. Selective electroless nickel deposition on copper as a final barrier/bonding layer material for microelectronics applications. Applied Surface Science 2002;185(3-4): 289-297.

19. Tang X, Bi C, Han C, Zhang B. A new palladium-free surface activation process for Ni electroless plating on ABS plastic. Materials Letters 2009;63(11): 840-842.

20. Kimura M, Yamagiwa H, Asakawa D, Noguchi M, Kurashina T, Fukawa T, et al. Site-selective electroless nickel plating on patterned thin films of macromolecular metal complexes. Applied Materials & Interfaces 2010;2(12): 3714-3717.

21. Riedel W. Electroless Nickel Plating. London, UK: ASM International; 1991.

22. Girginera B, Karagoza B, Urgenb M, Bicak N. A method for polyaniline coatings on solid polystyrene surfaces and electroless copper deposition. Surface & Coatings Technology 2008;202(17): 4176-4182.

23. Domenech S, Lima E, Drago V, Lima JD, Borges N, Avila A, et al. Electroless plating of nickel-phosphorous on surface-modified poly(ethylene terephthalate) films. Applied Surface Science 2003;220(1-4): 238-250.

24. Charbonnier M, Alami M, Romand M. Plasma treatment process for palladium chemisorption onto polymers before electroless deposition. Journal of the Electrochemical Society 1996;143(2): 472-480.

25. Calvert JM, Georger JH, Schnur JM, Schoen PE. Deep UV photochemistry and patterning of self-assembled monolayer films. Thin Solid Films 1992;210-211(1): 359-363.

26. Charbonnier M, Romand M. Polymer pretreatments for enhanced adhesion of metals deposited by the electroless process. International Journal of Adhesion and Adhesives 2003;23(4): 277-285.

27. Schrott AG, Braren B, O'Sullivan EJM, Saraf RF, Bailey P, Roldan J. Laser assisted seeding for electroless plating on polyimide surfaces. Journal of the Electrochemical Society 1995;142(3): 944-949.

28. Niino H, Yabe A. Surface modification and metallization of fluorocarbon polymers by excimer laser processing. Applied Physics Letters 1993;63(25): 3527-3529.

29. Tengsuwan S, Ohshima M. Electroless nickel plating on polypropylene via hydrophilic modification and supercritical carbon dioxide Pd-complex infusion. Journal of Supercritical Fluids 2012;69: 117-123.

30. Nakagawa M, Nawa N, Iyoda T. Selective Ni-P electroless plating on photopatterned cationic adsorption films influenced by alkyl chain lengths of polyelectrolyte adsorbates and additive surfactants. Langmuir 2004;20(22): 9844-9851.

31. Faghihnejad A, Zeng H. Hydrophobic interactions between polymer surfaces: using polystyrene as a model system. Soft Matter 2012;8(9): 2746-2759.

32. McQuarrie DA, Simon JD. Physical Chemistry: A Molecular Approach. Sausalito, CA: University Science Books; 1997.

33. Chandler D. Interfaces and the driving force of hydrophobic assembly. Nature 2005;437(7059): 640-647.

34. Delcorte A, Bertrand P, Wischerhoff E, Laschewsky A. Adsorption of polyelectrolyte multilayers on polymer surfaces. Langmuir 1997;13(19): 5125-5136.

35. Park J, Hammond PT. Polyelectrolyte multilayer formation on neutral hydrophobic surfaces. Macromolecules 2005;38(25): 10542-10550.

36. Jiang X, Ortiz C, Hammond PT. Exploring the rules for selective deposition: interactions of model polyamines on acid and oligoethylene oxide surfaces. Langmuir 2002;18(4): 1131-1143.

37. Kim B-S, Park SW, Hammond PT. Hydrogen-bonding layer-by-layer-assembled biodegradable polymeric micelles as drug delivery vehicles from surfaces. ACS Nano 2008;2(2): 386-392.

38. Kim B-S, Lee H-i, Min Y, Poon Z, Hammond PT. Hydrogen-bonded multilayer of pH-responsive polymeric micelles with tannic acid for surface drug delivery. Chemical Communications 2009(28): 4194-4196.

39. Wong SY, Han L, Timachova K, Veselinovic J, Hyder MN, Ortiz C, et al. Drastically lowered protein adsorption on microbicidal hydrophobic/hydrophilic polyelectrolyte multilayers. Biomacromolecules 2012;13(3): 719-726.

40. Mahammad S, Abdala A, Roberts GW, Khan SA. Manipulation of hydrophobic interactions in associative polymers using cyclodextrin and enzyme. Soft Matter 2010;6(17): 4237-4245.

41. Choi J. Fundamental studies of pH-sensitivity in polyeletrolyte multilayers. Boston, MA: Massachusetts Institute of Technology; 2004.

42. Fang M, Kim CH, Saupe GB, Kim H-N, Waraksa CC, Miwa T, et al. Layer-by-layer growth and condensation reactions of niobate and titanoniobate thin films. Chemistry of Materials 1999;11(6): 1526-1532.

43. Poncet C, Tiberg F, Audebert R. Ellipsometric study of the adsorption of hydrophobically modified polyacrylates at hydrophobic surfaces. Langmuir 1998;14(7): 1697-1704.

44. Lee I, Ahn JS, Hendricks TR, Rubner MF, Hammond PT. Patterned and controlled polyelectrolyte fractal growth and aggregations. Langmuir 2004;20(6): 2478-2483.

45. Srivastava D, Hendricks TR, Lee I. Step-edge like template fabrication of polyelectrolyte supported nickel nanowires. Nanotechnology 2007;18(24): article number 245305.

46. Bao G, Cai H. Delamination cracking in functionally graded coating/metal substrate systems. Acta Materialia 1997;45(3): 1055-1066.

47. Wiklund U, Gunnars J, Hogmark S. Influence of residual stresses on fracture and delamination of thin hard coatings. Wear 1999;232(2): 262-269.

48. Chai H, Fox J. On delamination growth from channel cracks in thin-film coatings. International Journal of Solids and Structures 2012;49(22): 3142-3147.

49. Ahn JS, Hendricks TR, Lee I. Control of specular and diffuse reflection of light using particle self-assembly at the polymer and metal interface. Advanced Functional Materials 2007;17(17): 3619-3625.

50. Hendricks TR, Wang W, Lee I. Buckling in nanomechanical films. Soft Matter 2010;6(16): 3701-3706.

51. Hendricks TR, Lee I. Wrinkle-free nanomechanical film: control and prevention of polymer film buckling. Nano Letters 2006;7(2): 372-379.

52. Park J, Hammond PT. Multilayer transfer printing for polyelectrolyte multilayer patterning: direct transfer of layer-by-layer assembled micropatterned thin films. Advanced Materials 2004;16(6): 520-525.

53. Berg MC, Choi J, Hammond PT, Rubner MF. Tailored micropatterns through weak polyelectrolyte stamping. Langmuir 2003;19(6): 2231-2237.

54. Eckenrode HM, Jen S-H, Han J, Yeh A-G, Dai H-L. Adsorption of a cationic dye molecule on polystyrene microspheres in colloids: effect of surface charge and composition probed by second harmonic generation. The Journal of Physical Chemistry B 2005;109(10): 4646-4653.

55. Bangs Laboratories I. Polymer Microspheres. Fishers, IN: Bangs Laboratories, Inc.; 2010.

56. Xia Y, Gates B, Yin Y, Lu Y. Monodispersed colloidal spheres: old materials with new applications. Advanced Materials 2000;12(10): 693-713.

57. Rieger PH. Electrochemistry. 2nd edition ed. New York, NY: Springer; 1994.

Chapter 5 Conclusions and future work

5.1 Conclusions

In summary, the nanotechnology based strategies were developed and applied in three fields: biomass pretreatment in biofuel production, functional material fabrication and surface modification.

First, a novel and fast nanoshear hybrid alkaline (NSHA) pretreatment method for lignocellulosic biomass was developed. Corn stover (CS) was pretreated as an illustrative example in a modified Taylor-Couette reactor with sodium hydroxide at room temperature, with a two-minute retention time and a 12500 s^{-1} shear rate. The NSHA pretreatment substantially enhanced the digestibility of CS. The saccharification rate and overall conversion of cellulose and hemicellulose were significantly improved over the untreated CS sample. A complete enzymatic conversion of the NSHA pretreated sample was achieved in one day. Compared with untreated corn stover, an approximately 4-fold increase in enzymatic cellulose conversion and a 5-fold increase in hemicellulose conversion were achieved. Also, the NSHA pretreatment facilitated significant removals of lignin and hemicellulose, leaving an up to 82 % of cellulose content in the remaining solid. In addition, micro-scale studies revealed inherent microstructural changes of the remaining solid in the pretreated biomass. The NSHA pretreatment was found to severely disrupt the biomass cell walls, and also caused fibrillations of cellulose fibers. The exposure of polysaccharide aggregates were also observed, and believed to be beneficial for improved accessibility of polysaccharides to enzymes.

Second, to overcome the compromised energy absorption capacity induced by the inherent characteristics of stress-strain property relationship of open-cell aluminum (Al) foams,

whereby upon homogeneous strut thickening, an increase in the plateau stress without a reduction in densification strain cannot be achieved, a nano-deposition strategy was developed. A featured non-cyanide nano-crystalline copper electro-deposition system was setup for the coating of open-cell Al foam, with which nano-crystalline copper (Cu) was uniformly deposited onto the Al foam, and novel 3-D composite foam structured materials were fabricated. The presented investigation aimed to demonstrate the hypothesis that a stiff nano-structured metal coating on an open-cell foam would lead to enhanced energy absorption under compressive load by increasing the elastic and plastic stress capacity of the composite foam material with minimum impact on the strut thickness and porosity, thus avoiding a significant reduction on the foam densification strain. The x-ray diffraction tests confirmed the crystallinity of the Cu deposition and the crystallite size was calculated to be 38 nm. Nano-Cu coated Al foams showed a quasi-static compressive response with an increased plateau stress, without compromising the densification strain. The advantage of a composite foam system was investigated by comparing the compressive performance of coated and uncoated foam samples with the same overall strut thickness, which showed that the Cu nano-crystalline coated Al foam possessed an elongated plastic region and, therefore, exhibited better energy absorbing capability.

Finally, a facile “dip & rinse” method for nickel (Ni) electroless deposition on hydrophobic polymer surfaces was developed. By making use of hydrophobic interactions between Poly(allylamine hydrochloride) (PAH) and polymer substrates, the proposed methodology eliminated the need for harsh and/or toxic surface treatment for the catalyst adsorption/immobilization. Various hydrophobic polymer surfaces with different geometries and dimensions were tested, and Ni was successfully deposited onto all of the polymer surfaces. Comparisons showed that, without the PAH, Ni coating was not able to be formed on any of

these polymer surfaces. Among these polymer thin sheets, with the same experiment condition and procedure, coverage of Ni coating can be ranked in the following order: PS > PP ≈ HDPE > LDPE. The study shows that Ni deposition achieved a thickness of ~2 μm in 2 hours. The coating thickness limitation can be addressed by applying a subsequent electro-deposition, even with a heterogeneous metal. The electro-deposition can expedite the thickness growth and extend the metallization of non-conductive materials to many aspects.

5.2 Outlook & future work

The NSHA pretreatment method for lignocellulosic biomass can be extended to at least two directions. First, the NSHA pretreatment method will be more attractive and competitive when a cost control is executed since an inexpensive pretreatment step is highly desired for an economic biofuel production from biomass. As mentioned in Chapter 2, the pretreatment accounts for the second largest portion in the entire cost of bioethanol production. A favorable pretreatment should be cost-efficient itself, and also benign to the downstream processes. For example, dilute acid pretreatment normally leads to the formation of degradation products (e.g., furfural), which are toxic to the next step - fermentation. Thus after the pretreatment, the biomass is subjected to a conditioning and separation step, which raises the cost both in equipment and operation. The cost control of the NSHA pretreatment can be done by "synergistically" optimizing the retention time, alkaline concentration, biomass loading, and shear rate. All these parameters are cost-sensitive. A quick solution will be elongating the retention time by a small margin while keeping other conditions the same since the small extension will not bring a severe safety concern. However, that small extension is a high shear process at an elevated temperature (100 °C) with an elevated alkaline concentration (water evaporation), which will make

considerable differences. At the same time, it would be interesting to further investigate the effect of NSHA pretreatment on many other biomass species. Comparison can be made to see if the NSHA pretreatment would be advantageous over other pretreat methods on certain types of biomass.

Second, from a research standpoint, many other chemicals can be tested and/or combined, other than those which involve safety issues. As previously discussed in Chapter 2, volatile chemical compounds and calcium hydroxide are not suggested to be incorporated with the high shear system. Other chemicals may substitute or add to sodium hydroxide for higher efficiencies. Promising candidates include sodium peroxide (Na_2O_2), hydrogen peroxide (H_2O_2), and ionic liquids. Water and most acids are less promising, since without the help of high shear, they are usually combined with high temperature (no less than 160 $^{\circ}$C) for an effective breakdown of biomass.

The work of nano-crystalline copper deposition on to open-cell Al foams for a better energy absorption capacity can be extended in many perspectives. First, other mechanical tests, including tension test, dynamic Hopkinson bar test of coated Al foams can be done to investigate other mechanical insights of the nano-crystalline copper deposition. That part of work is currently under investigation by our collaborators. Second, a further study on the steep stress reduction upon initiation of the plastic region can be done, and possible improvements can be made to reduce or even eliminate the stress drop. The stress drop is mainly due to the inhomogeneity between Cu and Al, giving rise to the imperfect adhesion at the interface. Different solutions (e.g., introduce chemical bond) to improve the adhesion may lead to different overall mechanical responses of coated Al foams. Finally, different materials with higher

stiffness can be coated on to the Al foams for enhanced mechanical properties. The candidates include iron (Fe), Ni, metal composites, graphene, graphite and so on.

The work of Ni electroless deposition on hydrophobic polymer surfaces is at the preliminary stage and can be extended. The potential application can be diverse. Studies can be done to enhance the interfacial bonding between metal (Ni) and various polymers, for a composite core-shell structure with higher stability. When combined Ni, because it has better mechanical strength, electrical and thermal conductivity than polymer, a better interfacial bonding always helps enhance the desired properties. On the other hand, the deposition strategy can be applied in the composite fabrication methodology when the interfacial bonding between metal and polymer is weak.